FLUID EVOLUTION AND MINERALISING POTENTIAL IN THE OUTER MARGIN OF THE SOUTHERN GARIEP BELT

BY

WARWICK STUART BOARD

Dissertation submitted in fulfilment of the requirements for the degree of Master of Science (Geology) at the University of Cape Town, South Africa.

Department of Geological Sciences
August 1998

ABSTRACT

Fluid inclusion analyses of quartz veins of various generations from the outer margin of the southern Gariep Belt reveal the presence of two chemically distinct fluid populations: the pre-orogenic, rift-related Rosh Pinah ore-forming fluid and the orogenic fluids. The ore-forming fluid is more saline and chemically more complex than the orogenic fluids, probably representing hot, chemically evolved hypersaline brines induced by rift-related magmatism. Four generations (D_1/D_2, D_3, D_4 and D_5) of orogenic veins are recognised on the basis of their structural relationships. The orogenic fluids are chemically similar, dominantly aqueous and generally of moderate to low salinities (<10 wt% $NaCl_{eq}$), with the few higher salinity estimates (10-16 wt% $NaCl_{eq}$) being attributed to the interaction of some of the orogenic fluids with evaporitic horizons. A trend of decreasing temperature with a decrease in age ($D_4>D_1/D_2>D_3>D_5$) is developed within the orogenic fluids, with the exception of those fluids related to the emplacement of the Kuboos Pluton, which yielded the highest temperatures. The D_1/D_2 fluids from the northern and Vanrhynsdorp areas were hotter than the fluids from the central area, whereas the D_3 and D_5 fluids exhibit no apparent temperature variation as a function of area. D_4 fluids show a decrease in temperature further away from the pluton. Estimates of the maximum metamorphic pressure recorded in the outer margin of the belt have been further constrained, using microthermometry results in conjunction with mineral assemblages, to 2.9-3.6 kbar, 2.9-3.1 kbar and 1.8-3.1 kbar for the northern, central and Vanrhynsdorp areas, respectively. Field observations and fluid inclusion analyses suggest channeled fluid flow on a regional rather than on an intra-formational scale, even though a rock-buffered system is suggested by oxygen isotope results. A different, largely rock-dominated fluid system was developed within the relatively impermeable carbonate units compared with the fluid system developed within the rest of the outer margin of the belt. The D_1/D_2 fluids probably represent circulating formation and metamorphic waters that were advectively forced out of the orogen and into the foreland, whereas channeled meteoric fluid flow most likely dominated during the transtensive phase of the orogeny. The D_4 fluids probably contain a magmatic component, in addition to the meteoric component. Comparisons between the ore-forming fluid and the orogenic fluids indicate that the latter have neither the required

salinities, nor the required chemistry necessary in order to transport sufficient metals to produce a massive sulphide deposit the size of Rosh Pinah. The chemistry of the orogenic fluids are, however, similar to those associated with gold remobilisation and as such the potential for gold mineralisation related to these orogenic fluids should not be ruled out. Base metal sulphide exploration within the outer margin of the belt should be confined to rocks of the Hilda Subgroup. The recognition of highly saline, chemically complex non-orogenic quartz vein-hosted fluid inclusions is considered critical from the point of view of base metal sulphide exploration.

LIST OF FIGURES

Figure 5.5 Summary bivariate plots of the triple-point depression (T_mCO_2) and the CO_2 homogenisation temperatures for Type II and Type III inclusions from post -D_1/D_2 quartz veins: (a) northern area, (b) central area, (c) southern area, (d) Vanrhynsdorp area.

Figure 5.6 Summary bivariate plots of the triple-point depression (T_mCO_2) and the CO_2 homogenisation temperatures for Type II and Type III inclusions from post -D_1/D_2 quartz veins: (a) D_3, (b) D_4, (c) D_5, and pre-orogenic quartz: (d) silicic footwall breccia, Rosh Pinah mine.

Figure 5.7 Ranges in $\delta^{18}O$ value (relative to V-SMOW) obtained from vein quartz and vein calcite for: (a) the various vein generations, (b) D_1/D_2 veins from different areas, (c) post-D_1/D_2 veins from different areas, (d) different host-rocks, in stratigraphic sequence. Note that R = Rosh Pinah mine, N = northern area, C = central area, S = southern area, B = basement, Sl = Lekkersing Fm, Sv = Vredefontein Fm, Kg = Kaigas Fm, Rp = Rosh Pinah Fm, Ph = Pickelhaube Fm, Nm = Numees Fm, Ho = Holgat Fm.

Figure 5.8 Bivariate plot of $\delta^{18}O_{vein}$ against $\delta^{18}O_{host\text{-}rock}$ for orogenic quartz veins, regardless of generation and geographical locality, hosted by different stratigraphic units.

Figure 5.9 Plot of $\delta^{18}O_{vein\ quartz}$ vs δD_{fluid}. The fields of metamorphic fluids and magmatic fluids, together with the global meteoric water line ($\delta D = 8\delta^{18}O+10$, after Craig, 1961) are shown for reference purposes. It should be noted that whilst vein quartz $\delta^{18}O$ values have been plotted, the ranges in $\delta^{18}O$ for the aforementioned fields and the meteoric water line correspond to ranges in $\delta^{18}O$ of the fluid.

Figure 5.10 Ternary diagrams of the most abundant cations (molar values) present within fluid inclusion leachates for the various samples analysed: (a, b) Na^+ -NH_4^+-K^+, (c, d) Na^+-Mg^{2+}-Ca^{2+}. Individual data points represent the average of the various sub-samples of each sample. Different vein generations, regardless of host-rock, are indicated in (a) and (c), whereas (b) and (d) show the different host-rocks for the various samples.

Figure 5.11 Ternary diagrams of the most abundant anions (molar values) present within fluid inclusion leachates for the various samples analysed: (a, b) Cl^--Br^- -SO_4^{2-}, (c, d) Cl^--CO_3^{2-}-SO_4^{2-}. Individual data points represent the average of the various sub-samples of each sample. The variation of the important anions as a function of different vein generations (regardless of host-rock), and as a function of host-rock, are indicated in (a) and (c), and (b) and (d), respectively. Note that the CO_3^{2-} component has been estimated from charge balance calculations (see text for discussion).

LIST OF TABLES

CONTENTS

1. INTRODUCTION

The theories of plate tectonics and supercontinent cycles have played important roles in the understanding of the Proterozoic crustal evolution of the Precambrian shield of southern Africa (Hartnady *et al.*, 1985). The manifestation of the operation of such processes is evident in the "mosaic" of major tectonic provinces on the western edge of the Kaapvaal Province (Fig. 1.1).

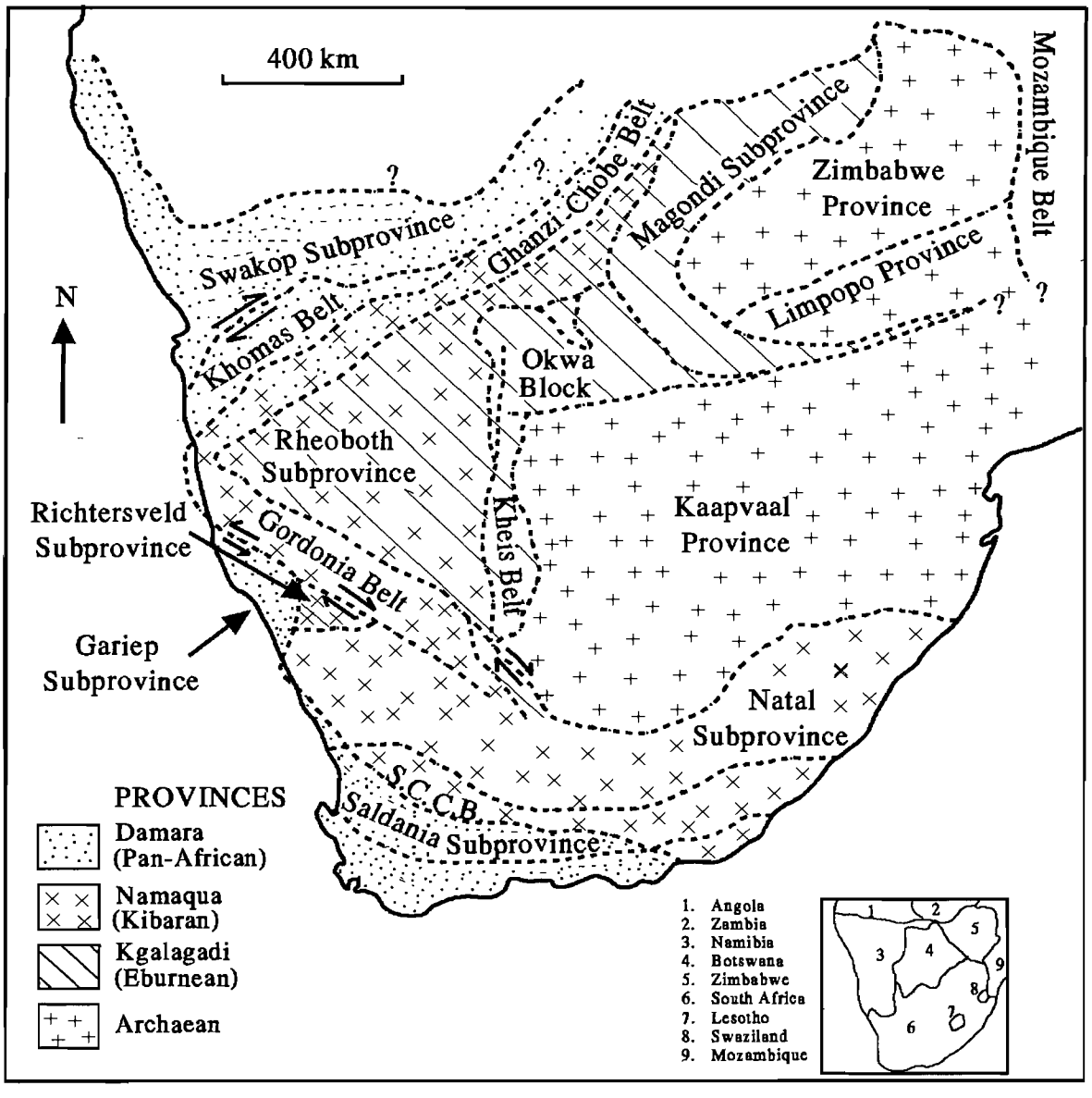

Figure 1.1 Major tectonic provinces and subprovinces of southern Africa (after Hartnady *et al.*, 1985). S.C.C.B. = Southern Cape Conductive Belt.

1.1 Proterozoic tectonic framework of southern Africa

Three main chelogenic cycles are considered to have given rise to the Proterozoic Provinces of southern Africa (Hartnady *et al.*, 1985) (Fig. 1.1). The Eburnean (2.0-1.7 Ga), which led to crustal accretion and growth on the western edges of the Kaapvaal and Zimbabwe Provinces, is recorded in the Kheis, Okwe and Magondi Subprovinces of the Kgalagadi Province (Hartnady *et al.*, 1985; Thomas *et al.*, 1993). Geochronological evidence exists (e.g. Barton, 1983) which suggests that the Richtersveld Subprovince was formed during the Eburnean cycle (Hartnady *et al.*, 1985; Thomas *et al.*, 1993). This was followed by the Kibaran (1.2-1.0 Ga) cycle during which the Namaqua Province was formed, most likely by multiple crustal amalgamation-accretion events (Hartnady *et al.*, 1985) as manifested in the mosaic of diverse terranes in this province.

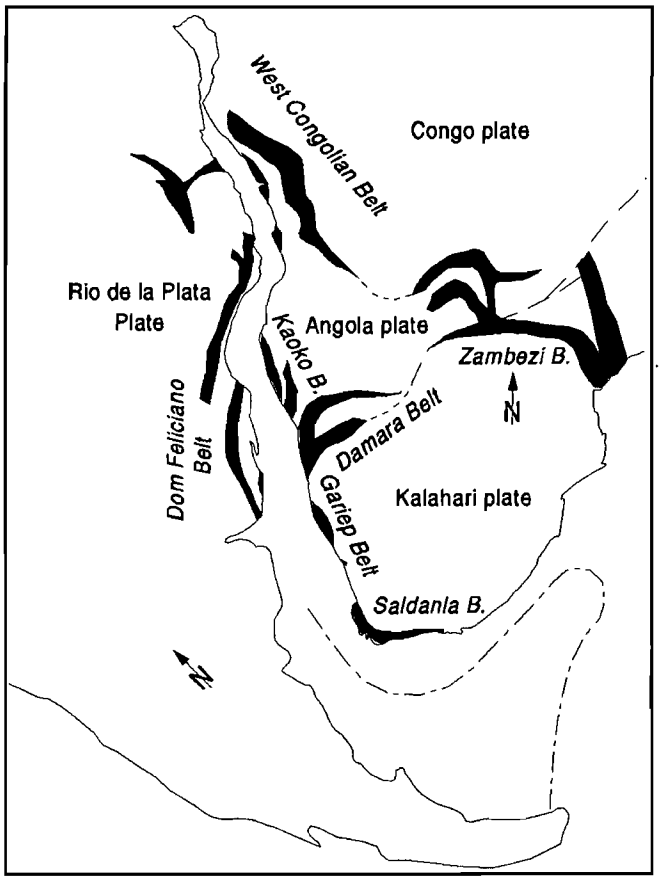

Figure 1.2 The configuration of Pan-African pre-orogenic rift sequences in southern Africa and South America (modified after Porada, 1989).

Numerous orogenic belts surround the Kalahari Plate (Figure 1.2), namely the Zambezi Belt in the north, the Damara Belt in the northwest, the Saldania Belt in the south and the Gariep Belt in the west (Fig. 1.2). These orogenic belts were formed as a consequence of the break-up of the supercontinent (Rodinia) formed by the Kibaran event, and the subsequent amalgamation of the late Proterozoic supercontinent, Gondwana (Frimmel, 1995; Frimmel *et al.*, 1996a; Prave, 1996) during the late Proterozoic-early Palaeozoic Pan-African cycle (~750-500 Ma).

1.2 The Pan-African (~750-500 Ma) in southwestern Africa

The Pan-African tectonic framework in southwestern Africa, including the Kaoko, Damara and Gariep Belts (Fig. 1.2), forms part of a larger Pan-African belt system in western Gondwana (e.g. Porada, 1989). The Damara Orogen (*sensu lato*) refers to a diverging structure consisting of two branches: (i) an intracontinental branch, the Damara Belt (*sensu stricto*) and (ii) a coastal branch, the Kaoko Belt (Miller, 1983; Porada, 1989). Stanistreet *et al.* (1991) extended the term 'coastal branch' to include both the Kaoko Belt (northern coastal branch) and the Gariep Belt (southern coastal branch). Models pertaining to the evolution of the Damara Orogen have varied from an orogen-aulacogen model with a triple junction of continental rifts formed above a mantle plume to the west of the present Namibian coast (Martin and Porada, 1977), to a Wilson-cycle model with sea-floor spreading, subduction and subsequent continental collision (e.g. Miller, 1983). Porada (1983, 1989) suggested that the intracontinental branch (along which the Khomas Sea was opened) originated from a rift structure propagating northwards from the Gariep Belt and then northeastwards into the continent. This rift structure, according to Porada (1989), may be thought of as being an offshoot of a major rift structure, extending northwards towards the West Congolian Belt (see Fig. 1.2), along which a Pan-African South Atlantic Ocean (hereafter termed the Adamastor Ocean after Hartnady *et al.*, 1985) was opened.

The post-rifting collision stage recorded in these belts is a result of the interactions between the Angola (after Frimmel and Frank, 1998) and Kalahari plates of Africa and the Rio de la Plata plate of South America during the Pan-African assembly of Gondwana (e.g.

Porada, 1989). Controversy as to the correct temporal sequence of tectonic events is manifest in the literature. Stanistreet *et al.* (1991) suggested the closure of the intracontinental branch (Damara Belt) prior to closure of the Adamastor Ocean. Prave (1996) indicated that Angola plate-Rio de la Plata plate suturing predated Angola plate-Kalahari plate suturing, supporting the interpretation of Coward (1983). Stratigraphic correlations (Germs, 1995) between the various platform successions of the Damara, Gariep and Vanrhynsdorp Belts on the basis of microfossil palaeontology and carbon isotope data suggest that the deformation in the Kaoko Belt is older than that of the Damara, Gariep and Vanrhynsdorp Belts. Frimmel and Frank (1998) provide evidence for the closure of the Damara Belt prior to that of the Gariep Belt. They propose that the closure of the southward widening Adamastor Ocean occurred as a result of oblique collision between the Rio de la Plata plate and Angola and Kalahari plates. This caused the progressive closure of the various basins from north to south, first producing the Kaoko Belt, then the Damara Belt and finally the Gariep Belt.

1.3 Fluid evolution and mineralising potential in the Gariep Belt

The tectonism related to the formation of the Gariep Belt, together with the coeval metamorphism of the sedimentary rocks to upper greenschist conditions (see Chapter 2), must have induced the expulsion of large volumes of aqueous orogenic fluid from the central parts of the orogen into the foreland (Frimmel, 1995). Given the presence of a number of rift-related base metal sulphide deposits within the outer margin of the Gariep Belt (see Chapter 2), some of the ore in these deposits may have been re-distributed by the orogenic fluids, accumulating in suitable traps further east in the foreland (Frimmel, 1995). This project was initiated, in the light of the previous discussion, in order to describe the evolution and assess the mineralising potential of the orogenic fluids by:

i) Chemically categorising the orogenic fluids related to the various deformation events (see Chapter 2) and, if possible, distinguishing between them;
ii) Comparing/contrasting the chemistry of orogenic fluids of the same generation within the same host-rock over different areas;

iii) Comparing/contrasting the chemistry of orogenic fluids of the same generation but hosted within different rock types;

iv) Comparing/contrasting the chemistry of orogenic fluids in mineralised areas with those in unmineralised areas;

v) Comparing/contrasting the chemistry of the fluids related to the primary ore with the orogenic fluids associated with the secondary remobilised ore at the Rosh Pinah mine.

2. THE PAN-AFRICAN GARIEP BELT

The late Proterozoic Gariep Belt forms an arcuate exposure along the west coast of southern Africa, extending from Lüderitz in Namibia to south of Port Nolloth in South Africa (Fig. 2.1, Appendix 1). The Gariep Belt strikes out to sea south of Port Nolloth and exists as a few minor exposures along the west coast as far south as the mouth of the Olifants River (Gresse, 1994)(Fig. 2.1). It probably links up with the Saldania belt further to the south (e.g. Porada, 1989; Gresse, 1994; Frimmel *et al.*, 1996a).

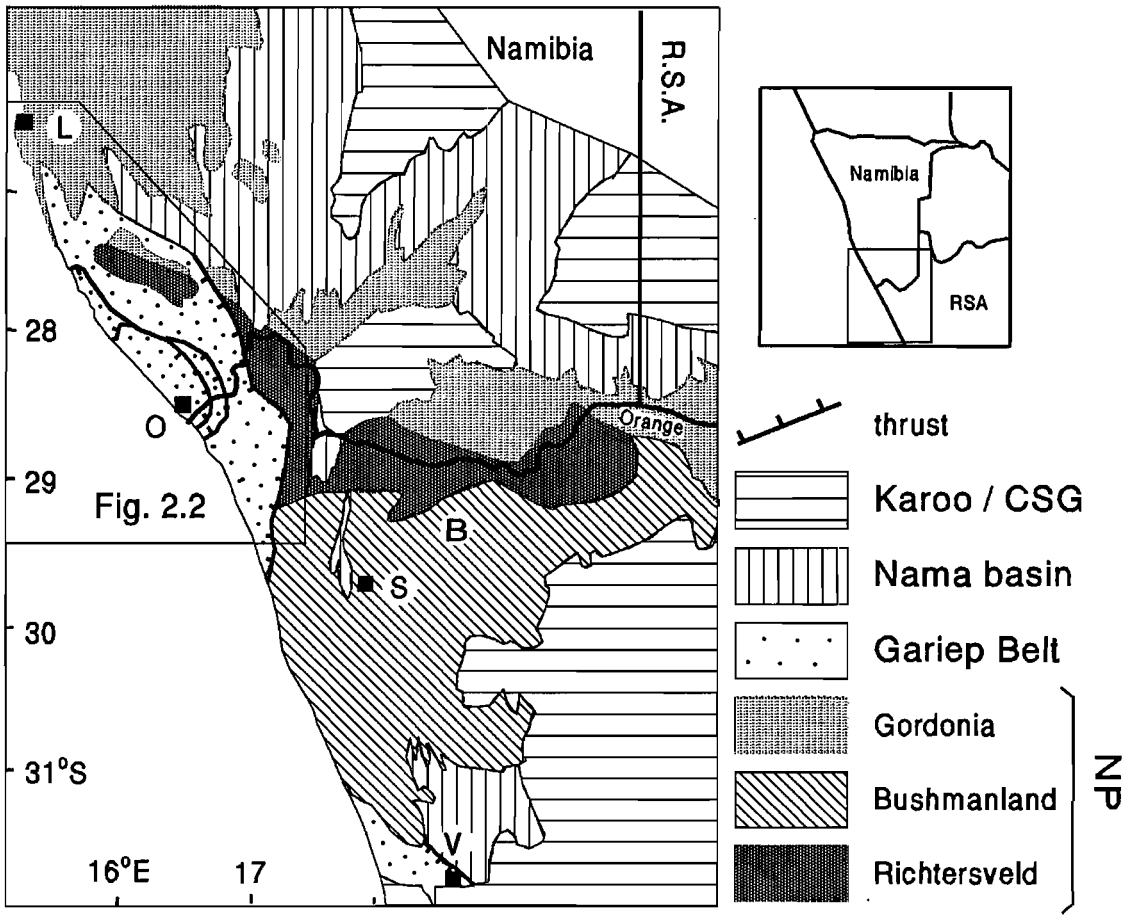

Figure 2.1 Simplified geological map of southern Namibia and northwestern South Africa showing the position of the Gariep Belt in relation to the three subprovinces of the Namaqua Province (NP). The syn- to post-orogenic molasse deposits of the Nama Group, overlain by the Palaeozoic Cape Supergroup (CSG) in the south and by the Karoo Supergroup in the north and east, are also shown. L = Lüderitz, O = Oranjemund, S = Springbok, B = Broken Hill deposit at Aggeneys, V = Vanrhynsdorp (modified after Frimmel and Frank, 1998).

2.1 Pre-Gariepian basement rocks

The Gariep Belt is bounded to the east by rocks of the Kibaran-aged Namaqua Province (see Fig. 2.1). The Namaqua Province is subdivided into the Richtersveld, Bushmanland and Gordonia Subprovinces (Hartnady *et al.*, 1985), and it can be seen from Fig. 2.1 that the northeastern sections of the Gariep Belt are underlain by high-grade rocks of the Gordonia Subprovince. The low-grade, supracrustal rocks of the Richtersveld Subprovince underlie the eastern portions of the belt, and the southern portions are thrust over the high-grade Bushmanland Subprovince. The rocks of the Namaqua Province were subjected to low-pressure granulite-facies metamorphism during the Namaqua thermal event (c. 1030 Ma in the Bushmanland Subprovince)(Waters *et al.*, 1996). Regional trends of structures within the Richtersveld and Bushmanland Subprovinces are typically east-west, whereas they are northwest-southeast in the Gordonia Subprovince (Hartnady *et al.*, 1985). An increasingly intense Pan-African overprint (thermal as well as structural) is exhibited by the basement rocks closer to the orogenic front of the Gariep Belt and the north-south trending structures in the southeastern Bushmanland Subprovince have been shown (Frimmel and Frank, 1998) to be of Pan-African rather than Kibaran age. Frimmel and Frank (1998) have proposed the transport of relatively hot orogenic fluids (expelled from the Gariep Belt during Pan-African tectonism and metamorphism) over at least 160 km to the east.

2.2 Tectonostratigraphic and lithostratigraphic subdivision

The Gariep Belt is subdivided into an eastern para-autochthonous passive continental margin zone, the Port Nolloth Zone, and the allochthonous, predominantly mafic Marmora Terrane in the west (Frimmel and Hartnady, 1992) (see Fig. 2.2). The Marmora Terrane was thrust in a southeasterly direction over the Port Nolloth Zone (Davies and Coward, 1982; Hartnady *et al.*, 1990; Frimmel and Hartnady, 1992; Von Veh, 1993).

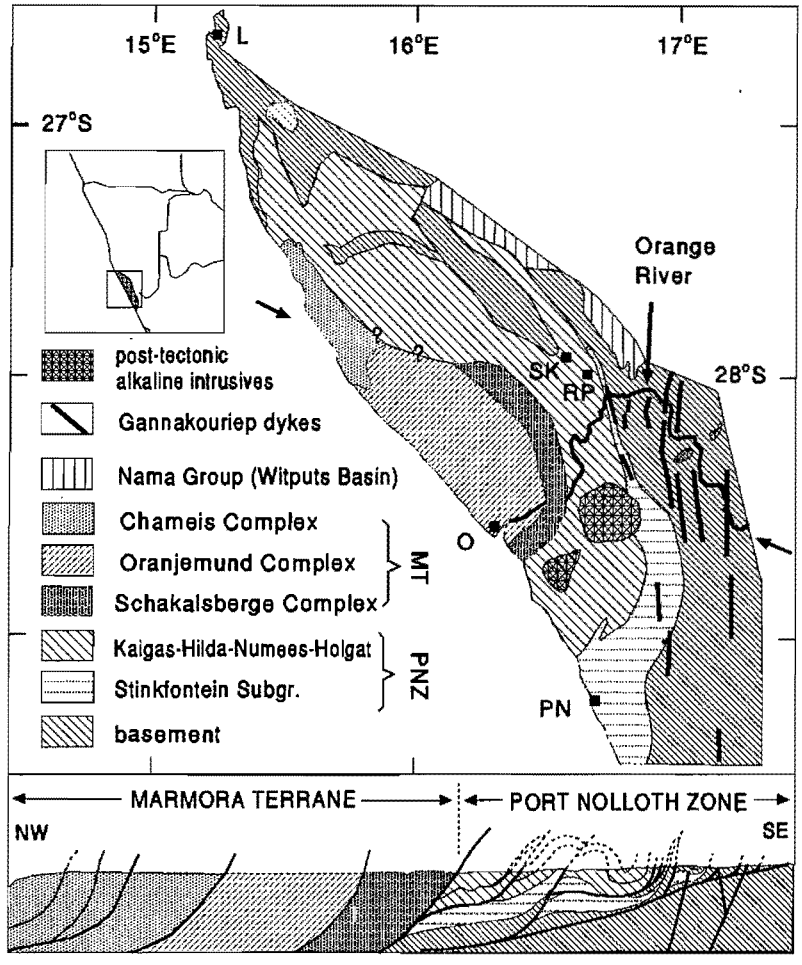

Figure 2.2 Simplified geological map of the Gariep Belt (after Frimmel and Frank, 1998) showing the distribution of the tectonostratigraphic units, with a NW-SE cross-section (arrows on map indicate line of section). L = Lüderitz, O = Oranjemund, PN = Port Nolloth, RP = Rosh Pinah mine, SK = Skorpion deposit, MT = Marmora Terrane, PNZ = Port Nolloth Zone.

2.2.1 The Port Nolloth Zone

The Port Nolloth Zone (PNZ) follows the arcuate trend of the eastern margin of the Gariep Belt southwards from an area between Bogenfels and Lüderitz in Namibia, via Rosh Pinah to a point south of Port Nolloth in South Africa where it strikes out to sea (Fig. 2.2). It reappears to the west of Vanrhynsdorp, where the Gariep Belt forms a re-entrant on the current South African coastline (Fig. 2.1). The lithostratigraphic subdivision of the PNZ is shown in Fig. 2.3. A Port Nolloth Group, comprising of all of the rocks of the Port Nolloth Zone, is now distinguished within the Gariep Supergroup (e.g. Frimmel and Frank, 1998).

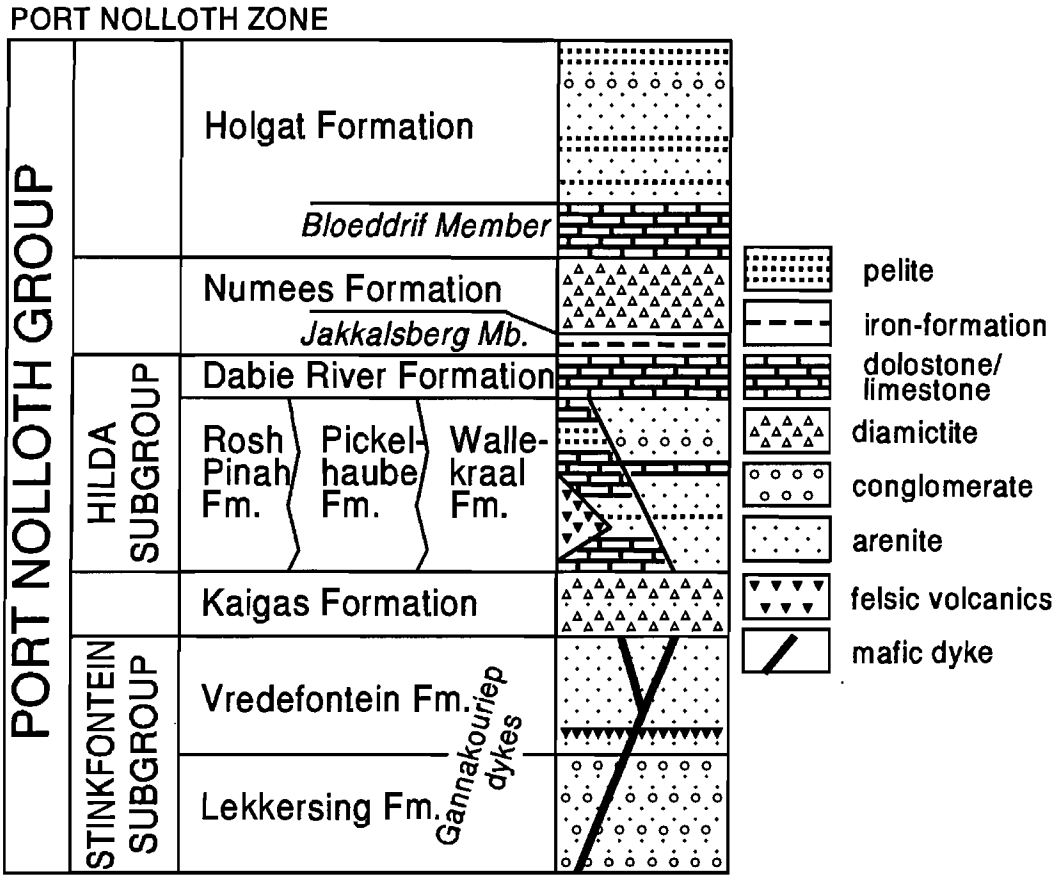

Figure 2.3 Lithostratigraphic subdivision of the Port Nolloth Zone (after Frimmel and Frank, 1998).

The predominantly sedimentary Stinkfontein Subgroup is comprised of fluvial conglomerate and quartz arenite of the Lekkersing Formation and feldspathic quartzites with minor intermediate to felsic volcanic rocks of the Vredefontein Formation (Von Veh, 1993; Frimmel and Board, unpubl. observations). The Gumchavib Formation (marginal marine calcareous feldspathic quartzites interbedded with dolomite and phyllite) of Von Veh (1993) is now regarded as a lateral facies variation in the Hilda Subgroup, being a time equivalent of the Pickelhaube and Wallekraal Formations (Frimmel and Fölling, unpubl. data).

A predominantly diamictic unit (interbedded with gritty quartzite, greywacke and laminated shale), the Kaigas Formation, overlies (unconformably in places) the Stinkfontein Subgroup (Von Veh, 1990, 1993). This, in turn, is overlain by a predominantly calcareous sequence, the Hilda Subgroup, which, according to Von Veh (1993), consists of metapelites, quartzites and meta-conglomerates of the Wallekraal Formation sandwiched between the platform carbonates of the basal Pickelhaube and upper Dabie River

Formations. Recent detailed stratigraphical investigations (Frimmel and Fölling, unpubl. data) have placed the Wallekraal Formation as a time-equivalent lateral facies variation of the Pickelhaube Formation, with the Dabie River Formation capping the sequence.

The predominantly volcanic Rosh Pinah Formation is only present north of the Orange River and is restricted to an area extending for approximately 35km from Rosh Pinah northwestwards (Frimmel *et al.*, 1996b)(see Fig. 2.4). This sequence of massive felsic lava flows and pyroclastic units grades laterally into the Hilda Subgroup strata and is considered to be a time equivalent to the lower Hilda Subgroup (Frimmel *et al.*, 1996a, 1996b). The Rosh Pinah Formation can be subdivided into a proximal volcanic facies and a distal volcaniclastic facies (Frimmel *et al.*, 1996b)(Fig. 2.4), with the former comprising massive rhyolitic lava flows, felsic agglomerates, ignimbrites, crystal tuffs and tuffites, intercalated sulfidic black shales, cherts and dolomitic limestones. A predominantly sedimentary package of arkoses, calc-arenites, argillite intercalated with minor carbonates, tuffitic shale, conglomerates, ferruginous shale and chert, with minor felsic volcanic and pyroclastic rocks characterises the distal facies (Frimmel *et al.*, 1996b). The presence of mafic rocks underlying the felsic sequence has been revealed in a drill core (Frimmel *et al.*, 1996a, 1996b).

The Hilda Subgroup is overlain by the massive glaciogenic diamictites with thin near basal intercalations of banded ironstone (Jackalsberg Member) of the Numees Formation (Von Veh, 1990, 1993). The stratigraphic top of the PNZ consists of the shallow to deepwater clastic Holgat Formation marbles (which cap the Numees Formation), meta-arkoses, meta-greywackes and metapelites (Von Veh, 1993). A mafic dyke swarm (the Gannakouriep swarm) intruded the pre-Gariepian basement rocks and the basal units of the PNZ (viz. the Stinkfontein Subgroup, see Figs 2.2 and 2.3)(Reid *et al.*, 1991; Frimmel *et al.*, 1996b).

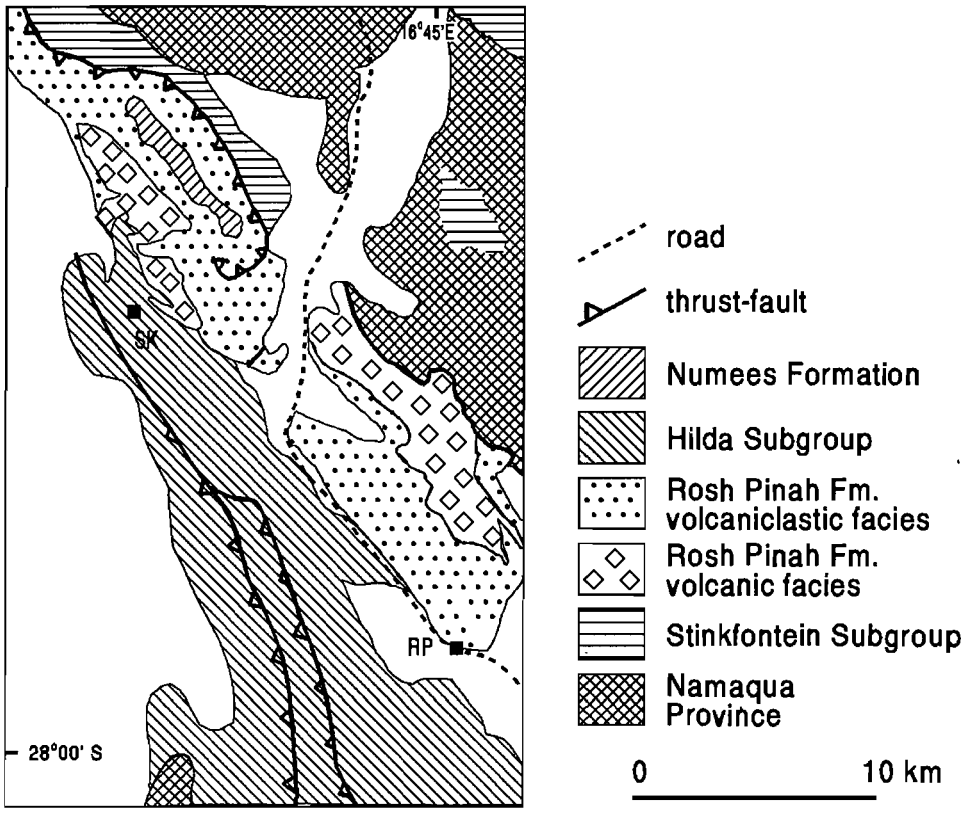

Figure 2.4 Simplified geological map of the area northwest of the Rosh Pinah Mine showing the distribution of the Rosh Pinah Formation (modified after Frimmel *et al.*, 1996b). RP = Rosh Pinah mine, SK = Skorpion deposit.

2.2.2 The Marmora Terrane

The Marmora Terrane (MT), juxtaposed against the PNZ along the Schakalsberge Thrust, forms a horn-shaped area extending southwestwards from just north of Bogenfels in Namibia (the tip of the horn) to Alexander Bay in the Republic of South Africa (see Figure 2.2). The MT consists of three tectonostratigraphic units: the Schakalsberge Complex, the Oranjemund Complex and the Chameis Complex (Hartnady *et al.*, 1990; Frimmel and Hartnady, 1992; Frimmel *et al.*, 1996a).

The Schakalsberge Complex forms the easternmost extension of the MT, and is separated from the westernmost PNZ by the Schakalsberge Thrust. The Schakalsberge Complex consists of the predominantly mafic Grootderm Formation, capped by dolomites

of the Gais Member (Appendix 1). The Grootderm Formation consists of aphyric, porphyric and amygdaloidal metabasalts with pillow structures, agglomerates and tuff horizons and abundant hyaloclastites (Frimmel *et al.*, 1996a). Metagabbros and serpentinised picrites occur near the bottom of this formation. The Grootderm Formation is intruded by the Rooilepel Bostonite Suite (Hartnady *et al.*, 1990; Frimmel and Hartnady, 1992).

The Oranjemund Complex (Fig. 2.2) consists mainly of an interlaminated succession of metagreywackes, phyllites and quartzites (Hartnady *et al.*, 1990; Frimmel and Hartnady, 1992; Frimmel *et al.*, 1996a) varying from very low to low grade, relatively undeformed cyclothemic turbidites to intensely deformed mica schists. The localised intercalations of chlorite schists may either be metamorphosed tuffs or the erosional products of the Grootderm lavas (Frimmel *et al.*, 1996a).

The Chameis Complex, the northwestern-most outcrop of the MT (Fig. 2.2), consists of a sequence of serpentinites, metamorphosed gabbros, basalts, basaltic breccias, hyaloclastites and tuffs overlain by ferruginous pelites, alternating dolomite and quartzite bands and various phyllites (Frimmel *et al.*, 1996a). Evidence for these rocks representing ancient oceanic crust (from field observations and associated rock types) was presented by Frimmel *et al.* (1996a). Tectonic repetition of the aforementioned sequence combined with the presence of exotic mafic and ultramafic blocks from different oceanic enviroments occurring in close proximity within a highly tectonised metasedimentary envelope, has been noted by several authors (e.g. Hartnady *et al.*, 1990; Frimmel and Hartnady, 1992; Frimmel *et al.*, 1996a). This supports the interpretation of the Chameis Complex (Hartnady *et al.*, 1990) as a tectonic mélange zone.

2.3 Mineralisation in the Gariep Belt

"By virtue of its inaccessibility, the Richtersveld has always been said by the romantically minded to contain large mineral deposits of exceptional richness. Although

past prospecting has admittedly been desultory and deposits of a wide range of minerals do occur, large-scale mineralisation is practically unknown" (De Villiers and Söhnge, 1959).

Numerous prospects (e.g. Kodas and Numees copper prospects, Billingham's gold prospect etc.) within the Gariep Belt bear testimony to the "romantic" lure of the Richtersveld and the vain hope of finding the "mountains of copper" and other rich mineral deposits rumoured to exist in such "godforsaken country". Although occurrences of asbestos, barite, native copper (as well as oxides and sulphides), gold, fluorspar, graphite, gypsum, scheelite, iron oxides, galena (containing minor silver in places), molybdenite, phosphate and cassiterite have been described from these old prospects (see De Villiers and Söhnge, 1959), they are generally highly localised and are of no economic interest. Some of the mineralisation described (e.g. barite, copper oxides and sulphides, gold, galena) from these old prospects is found in shear zone-, fault- and fracture-hosted quartz veins, indicating a deformation-induced genesis. Inferred source regions for the mineralisation include: remobilisation and concentration of the important minerals from proximal basic dykes (De Villiers and Söhnge, 1959) and/or possibly from the host rock itself. The general lack of vertical persistence (De Villiers and Söhnge, 1959) in these deposits highlights their localised nature. Elsewhere the mineralisation (e.g. the various copper minerals, galena, fluorspar and molybdenite hosted by quartz veins and other rocks from the aureole of the Kuboos pluton, scheelite and cassiterite in pegmatites and granites, respectively) is most probably genetically related to igneous activity (De Villiers and Söhnge, 1959). The mineralisation related the igneous activity is not of economic interest (De Villiers and Söhnge, 1959).

As a result of the lack of "large-scale" mineralisation, the alluvial diamond deposits related to the Orange River and its floodplain constituted the main source of mineral wealth and production in the Richtersveld (De Villiers and Söhnge, 1959) until 1969 when the mineral deposit discovered at Rosh Pinah (1963) became a mine (Fig. 2.2)(Van Vuuren, 1986). The find resulted in renewed interest in the area, especially in the unexplored ground within Diamond Area No. 1 in southern Namibia for which Consolidated Diamond Mines

(Pty) Ltd (CDM) had sole prospecting rights. An agreement between CDM and Anglo American Prospecting Services Namibia (Pty) Ltd in 1975 allowed the latter to explore for base metals within this area (Erongo Exploration and Mining Company Ltd and Reunion Mining PLC, 1996). As a result of this, a belt of major Zn-Pb-Cu-Ag mineralisation was discovered in the Rosh Pinah Formation to the northwest of Rosh Pinah itself: the Skorpion Prospect (Erongo Exploration and Mining Company Ltd and Reunion Mining PLC, 1996). In the light of the previous discussion, the rest of this section will focus on the Skorpion Prospect and the Rosh Pinah Deposit as they are the only (known) representatives of appreciable base metal sulphide mineralisation within the Gariep Belt.

The Skorpion and Rosh Pinah Zn-Pb-Cu-Ag (+Ba) deposits are situated (~60 km and ~30 km, respectively) northwest of the Dreigratberg in southwestern Namibia (Fig. 2.2). They are hosted in sulphidic black shale, chert and carbonate lenses within a narrow stratigraphic zone closely associated with thin felsites and ignimbrites near the top of the Rosh Pinah Formation (see section 2.2.2). These deposits are considered as being related to the same mineralising event(s) (Van Vuuren, 1986; Erongo Exploration and Mining Company Ltd and Reunion Mining PLC, 1996).

The geological setting of a rift graben, evidenced by the sedimentological features (e.g. Van Vuuren, 1986; Siegfried and Moore, 1990, section 2.2.2) of, and recent geochemical investigations (Frimmel *et al.*, 1996a, 1996b) on the Rosh Pinah Formation, provides a favourable environment for volcanogenic to distal volcano-sedimentary-hosted stratiform massive base metal sulphide deposits (Guilbert and Park, 1986). The Skorpion base metal deposits are classified as volcanogenic massive sulphide deposits (Erongo Exploration and Mining Company Ltd and Reunion Mining PLC, 1996) and several authors (Van Vuuren, 1986; Siegfried and Moore, 1990) agree on a distal volcano-sedimentary exhalative origin for the Rosh Pinah massive sulphide deposit. The fine grain size of the primary sulphide minerals, some showing framboidal as well as colloform textures, the presence of soft sediment deformation structures and graded bedding within the massive sulphides, concordance of the ore horizons with stratigraphy, lateral and vertical metal zonation, and

rip-up clasts of the ore-zone rock types in the overlying strata provide evidence for a syn-sedimentary exhalative origin for the Rosh Pinah deposit (Siegfried and Moore, 1990; Frimmel *et al.*, 1996b). Mineralisation in both the Skorpion and Rosh Pinah deposits was accompanied by brecciation and silicification (Van Vuuren, 1986; Siegfried and Moore, 1990; Erongo Exploration and Mining Company Ltd and Reunion Mining PLC, 1996; Frimmel *et al.*, 1996b), as evidenced by intense stockwork brecciation in the footwall quartzite and by dark sulphidic chert in the ore horizon.

The Skorpion and Rosh Pinah deposits have both been modified by the regional deformation (section 2.4) related to Pan-African tectonism, and, as a result, are structurally complex (Van Vuuren, 1986; Siegfried and Moore, 1990; Hälbich and Alchin, 1995; Erongo Exploration and Mining Company Ltd and Reunion Mining PLC, 1996; Frimmel *et al.*, 1996b). Localised recrystallisation and remobilisation of the sulphides (in the Rosh Pinah deposit) is evident in fold hinges and thrusts, accompanied by CO_2 metasomatism (Frimmel *et al.*, 1996b), and the upper parts of some of the ore bodies show evidence for later supergene alteration. The massive sulphides of the Skorpion deposits have been affected by deep oxidation and, together with the excessive drilling difficulties, the lack of unoxidised sulphide ore at reasonable depths led to the termination of work on these deposits in 1982 (Erongo Exploration and Mining Company Ltd and Reunion Mining PLC, 1996). The Rosh Pinah deposit is currently the only mineral deposit (apart from the numerous alluvial diamond diggings and mines along the Orange River and the West Coast) being mined.

2.4 Evolution of the Gariep Belt

According to Porada (1989), the majority of the Pan-African belts surrounding and traversing the African continent and partly extending into South America, Antarctica and Australia must have evolved from continental rift structures that were subsequently closed during the amalgamation of Gondwana. The application of a modern Wilson-cycle to the evolution of these belts in southern Africa had been inhibited by only equivocal evidence of

oceanic crust and the lack of blueschist and/or eclogite facies metamorphism (Frimmel and Hartnady, 1992). Recently, however, detailed studies of the mafic and ultramafic magmatic units of the MT (Frimmel and Hartnady, 1992; Frimmel *et al.*, 1996a) have provided unequivocal evidence for the existence of oceanic crust within the Gariep Belt. The passive continental margin PNZ sediments were deposited, together with the formation of the oceanic crust of the MT, during the rifting and seafloor spreading stages of the evolution of the Gariep Belt (Von Veh, 1993; Frimmel and Frank, 1998). The deformation and metamorphism of the Gariepian rocks occurred during the subsequent collision stage in which the MT was thrust over the PNZ in a SE direction along the Schakalsberge Thrust (Von Veh, 1993; Frimmel, 1995).

The deposition of the Stinkfontein sediments as broad coalescing alluvial fans within a continental environment at the foot of an uplifted region to the east (Von Veh, 1993) marks the onset of the extensional stage in the southern Gariep Belt. The basal (proximal) Lekkersing Formation contains sedimentary features typical of the upper flow regime, gradually decreasing to moderate flow conditions during the deposition of the more distal Vredefontein Formation and palaeocurrent directions derived from trough cross-bedding confirm a source region in the east. The occurrence of minor volcanic rocks within the Vredefontein Formation indicates intermittent nearby, volcanic activity covering the fan deposits (Von Veh, 1993). The northward pinching-out of the Stinkfontein Subgroup (Fig. 2.2; Appendix 1) is considered to be a primary sedimentary feature related to the westward swing of the depositional basin with progressive rifting, and an increase in distance from the main depositional centre (Von Veh, 1993).

Thrust slices of basement granite (Lekkersing granite, 781^{+34}_{-31} Ma, recalculated U-Pb zircon age)(Allsopp *et al.*, 1979) exist within the quartzites of the Stinkfontein Subgroup, providing a maximum age for the onset of Stinkfontein sedimentation (Frimmel and Frank, 1998). Progressive extension led to the production of localised grabens and half-grabens on the western flank of the aforementioned fault scarp by step faulting (Von Veh, 1993; Hälbich and Alchin, 1995) which were filled in by the talus, landslide and debris flow

deposits of the Kaigas Formation. The presence of clasts penetrating and deforming the underlying laminations, bimodal clast distributions and outsized erratic blocks in shaley beds provide evidence for a glacial debris contribution (Von Veh, 1993).

The dating of single zircons (Pb-Pb evaporation technique) from the low-grade metamorphosed rhyolites of the Rosh Pinah Formation by Frimmel *et al.* (1996b) has provided a minimum age constraint for the onset of continental break-up in southern Namibia at 741±6 Ma. Consequently the earliest onset of crustal extension in the Gariep Belt can be bracketed between ~781 Ma and ~741 Ma. This Pb-Pb age (741±6 Ma) is statistically indistinguishable from that obtained for rhyolite lavas (748±3 Ma, U-Pb single zircon age)(Hoffman *et al.*, 1994) of the upper Naauwpoort Formation of the syn-rift Nosib Group in the northern Damara Belt (*sensu stricto*), suggesting the coeval births of the Adamastor and Khomas oceans (Frimmel *et al.*, 1996b). Recent geochemical studies combined with sedimentological and structural data (Frimmel *et al.*, 1996a, 1996b) on the felsic and mafic rocks of the Rosh Pinah Formation indicate that the earliest magmatic activity related to the rifting was bimodal volcanism with continental within-plate affinity along a failed rift graben. Frimmel *et al.* (1996a, 1996b) showed that the Rosh Pinah Formation was derived from a different mantle source than all the other mafic magmatic units within the belt, supporting the idea of a failed rift.

The intrusion of the Gannakouriep dyke swarm, parallel to the rift structures, at ~717 Ma may herald a more advanced stage of rifting (Frimmel *et al.*, 1996a, 1996b). The fact that these dykes are younger than the Rosh Pinah Formation, but do not appear to intrude it, may indicate that the age determined by Reid *et al.* (1991) is too young and in need of revision (Frimmel and Fölling, 1998). Geochemical evidence presented in Frimmel *et al.* (1996a, 1996b) shows that the mafic rocks of the Rosh Pinah Formation were derived from a different magmatic source than the Gannakouriep mafic dyke swarm, even though both exhibit continental within-plate geochemical affinities.

The shallow water carbonate-clastic Hilda Subgroup was deposited during the sea-floor spreading stage of the Adamastor Ocean, between ~740 Ma and ~630-600 Ma (Von Veh, 1993; Hälbich and Alchin, 1995; Frimmel and Frank, 1998). The massive platform carbonates of the Pickelhaube Formation and the Wallekraal Formation submarine fan siliciclastic rocks exist as contemporaneous lateral facies variations (Frimmel and Fölling, 1998), the basal parts of which were being deposited contemporaneously with the bimodal volcanism described above (Frimmel *et al.*, 1996a, 1996b). The shallow water (e.g. barrier bar/shelf lagoon) platform carbonates of the Dabie River Formation cap the Hilda Subgroup (Von Veh, 1993).

A recent geochemical study (combined with sedimentological and other field observations) on the magmatic rocks of the Gariep Belt (Frimmel *et al.*, 1996a) has revealed a within-plate setting for all of the magmatic units. Frimmel *et al.* (1996a) showed distinct differences in various geochemical signatures, despite the general tholeiitic nature of the mafic rocks from all units, suggesting different positions of the magmatic activities with respect to their tectonic setting. The widespread presence of basalts with compositions similar to oceanic seamounts (or aseismic ridges) within the Schakalsberge and the Chameis Complexes may be interpreted as evidence for plate movement over a hotspot (Frimmel *et al.*, 1996a). These authors suggest that the Gannakouriep dyke swarm, the Grootderm Formation basalts and the Chameis Complex alkali basalts are all possibly related to the same hotspot. Considering the tectonic setting of the Gannakouriep dykes, and the basalts of the Schakalsberge and Chameis Complexes, these magmatic units can be thought of as representing an array of within-plate magmatic activity stretching from a continental environment in the southeast to an oceanic environment in the northwest (Frimmel *et al.*, 1996a).

The newly-formed oceanic crust of the Adamastor ocean drifted and subsequently cooled through c. 500°C sometime between 630 Ma and 600 Ma ($^{40}Ar/^{39}Ar$ ages, Frimmel and Frank, 1998). The oceanic crust was then subjected to low-P hydrothermal metamorphism, which is recorded in the metagabbros of the Chameis Complex (Frimmel

and Frank, 1998). This metamorphism (M_1), being the earliest recognisable metamorphic event within the Gariep Belt, is manifest in the pre-tectonic (see later) replacement of magmatic clinopyroxene by edenitic amphiboles or hornblende (Frimmel and Hartnady, 1992). At some stage during the evolution of the Adamastor Ocean, the deep sea turbiditic Oranjemund Complex was formed by siliciclastic sedimentation and partial reworking of the adjacent volcanic piles (e.g. slumping, turbidity currents) in a continental slope setting (Hartnady *et al.*, 1990; Frimmel *et al.*, 1996a, Frimmel and Frank, 1998).

Deposition of the glaciogenic Numees Formation occurred after the deposition of the platform carbonates and the rift/drift transition (Von Veh, 1993; Frimmel and Frank, 1998). The extensive lateral distribution of the Numees Formation, its textural homogeneity and unbedded nature, and the presence of outsized extrabasinal dropstones indicates deposition adjacent to a glaciated continental margin by processes of settling from suspension and ice rafting (Von Veh, 1993). Up-welling of anoxic, Fe-rich bottom waters onto a shallow continental shelf and the subsequent contact with cold, oxygenated surface waters led to the precipitation of the Jakkalsberg Member iron-formation (Kaufman *et al.*, 1991; Frimmel and Von Veh, 1998a). The deposition of the Numees Formation diamictite has been correlated with the Vendian global glacial epoch (625-580 Ma; Meert and Van der Voo, 1994)(Frimmel *et al.*, 1996b).

The metagabbros of the Chameis Complex were, subsequent to M_1, subjected to a second metamorphic event, evidenced by more barroisitic rim compositions of earlier hornblende (Frimmel and Hartnady, 1992). This relatively high-pressure ($P \leq 6$ kbar, T: 500-550°C) metamorphic event (M_2) is interpreted as being a response to a process of shallow subduction that affected only the mafic and ultramafic rocks of the MT (Frimmel and Hartnady, 1992; Frimmel, 1995). Neither M_1 nor M_2 are recorded in the rocks of the PNZ (Frimmel, 1995). The lack of eclogite or blueschist facies rocks, and the absence of a magmatic arc in the Gariep Belt, precludes subduction beneath the Kalahari Plate (Frimmel *et al.*, 1996a; Frimmel and Frank, 1998). The principal subduction direction was probably towards the northwest, underneath the Rio de la Plata Plate (Frimmel *et al.*, 1996a; Frimmel

and Frank, 1998) where the corresponding magmatic arc might be found in the Dom Feliciano Belt of Southern Brazil and Uruguay (e.g. Fernandes *et al.*, 1992; Fernandes and Koester, 1998). This event lead to the tectonic assembly of the Marmora Terrane in the shallow leading part of an accretionary wedge, east of the Dom Feliciano Belt (Frimmel *et al.*, 1996a)(see Fig. 2.5). Recent $^{40}Ar/^{39}Ar$ ages (Frimmel and Frank, 1998) recorded by hornblende in the Chameis Complex indicate that this event must have taken place prior to 575 Ma, consequently placing a lower age limit on the timing of the inversion from extension to compression.

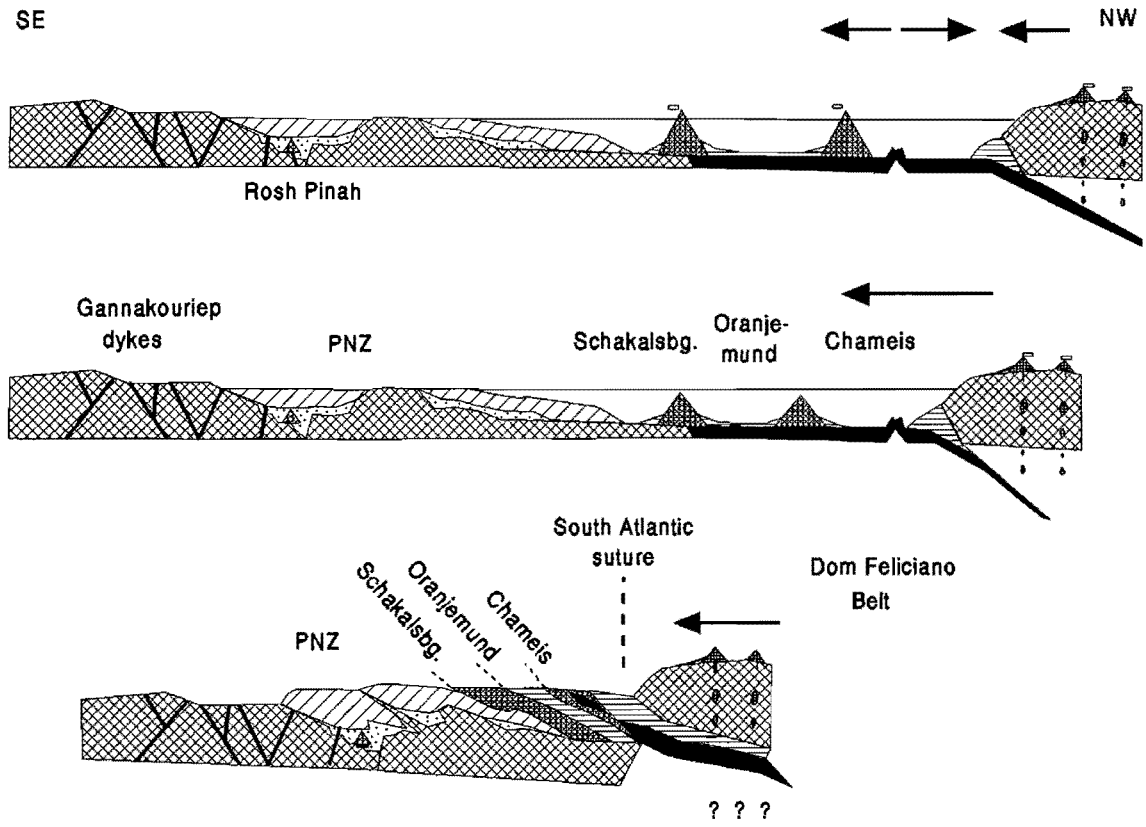

Figure 2.5 Post-extension evolution of the Gariep Belt (after Frimmel *et al.*, 1996a). *Top*: spreading and subduction beneath South America (after ~741 Ma), hotspot-related volcanism and deposition of the Gariep Supergroup along a passive continental margin; *middle*: formation of an accretionary wedge (~575 Ma); *bottom*: closure of the ocean by continent-continent collision (~545 Ma).

The deposition of the deepwater clastic Holgat Formation sediments followed the deposition of the Numees Formation (Von Veh, 1993), and they are probably coincident with the inversion from extension to compression (Frimmel and Frank, 1998). A combined

slope/outer continental shelf depositional environment is envisaged as both turbiditic and quiet, anoxic, relatively deepwater sediments occur (Frimmel and Von Veh, 1998b).

Continued compression led to continent-continent collision during which the accretionary wedge of the MT was thrust over the PNZ along the Schakalsberge thrust (Von Veh, 1993; Frimmel *et al.*, 1996a)(Fig. 2.5). The collision led to crustal thickening due to the stacking of imbricate thrust slices, the individual faults of this imbricate fan often being re-activated, rift-related growth faults (Von Veh, 1993; Hälbich and Alchin, 1995; Frimmel *et al.*, 1996b). The deformation was accompanied by regional low-grade metamorphism (Von Veh, 1993; Frimmel, 1995).

Von Veh (1993) recognised a five-fold sequence of deformation events (D_1 to D_5) related to two main collisional phases: an initial transpressive phase (D_1 and D_2) and a later left-lateral transtensive phase (D_3 to D_5). These phases, and the events they comprise of, represent a continuum of deformation related to the continual SE-ward migration of the accretionary wedge during the progressive closure of the Adamastor Ocean (Von Veh, 1993; Frimmel and Frank, 1998; this study) rather than a series of isolated events.

The first and most penetrative deformation (D_1) is characterised by NNW-SSE trending features including thrust faults steepening towards the northeast, asymmetric open to isoclinal F_1 folds with eastward vergeance and a penetrative S_1 schistosity steepening towards the east (i.e. towards the crystalline basement)(Von Veh, 1993). A strong NNW-plunging stretching lineation (L_1) indicates a general transport direction to the SE or SSE (Von Veh, 1993; Frimmel, 1995). Continual SE-ward migration of the accretionary wedge was accompanied by sinistral wrenching (D_2 - coaxial to D_1) which led to the further steepening of the D_1 structures and resulted in the formation of non-cylindrical, close, westward-verging F_2 back-folds and back-thrusts along the eastern margin of the PNZ (Von Veh, 1993). A shallow to moderate ENE-dipping S_2 crenulation cleavage is associated with F_2 (Von Veh, 1993). The structural control of the change in orientation of the Neoproterozoic continental margin from northwest-southeast to northeast-southwest (see

Fig. 2.2) is evident in the southward decrease in the wrench/thrust shear ratio. Sinistral wrench tectonics dominate in the northern (lateral edge) parts, whilst thrust shear dominates in the southern (frontal) parts of the PNZ (Von Veh, 1993; Gresse, 1994; Frimmel, 1995).

The peak regional metamorphic conditions were reached between the D_1 and D_2 events (Von Veh, 1993; Frimmel, 1995), are generally low grade (greenschist facies) and show no differences as a function of stratigraphic position, although Frimmel (1995) showed that different areas were affected to differing degrees. The differences between the generally lower grade regional metamorphism (M_3) experienced by the tectonically higher MT (lower greenschist facies), and the relatively higher grade experienced by the PNZ has been ascribed to crustal thickening due to thrusting (Frimmel, 1995; Frimmel and Frank, 1998). The peak regional metamorphism in the PNZ (M_{reg}) has been dated at 542±4 Ma ($^{40}Ar/^{39}Ar$ plateau age) by Onstott *et al.* (1986). This age was subsequently re-interpreted as 546±10 Ma by Reid *et al.* (1991). Frimmel and Frank (1998) showed that regional metamorphism reached its peak within the MT between 547 Ma and 543 Ma ($^{40}Ar/^{39}Ar$ age). This indicates that the peak regional metamorphism, corresponding to the transpressive deformation and the emplacement of the MT above the PNZ, in the internal and external zones of the Gariep Belt was reached coevally (~545 Ma)(Frimmel and Frank, 1998).

The onset of the late left-lateral transtensive phase (post peak metamorphism) led to the D_3 event characterised by the production of minor NNW-SSE trending normal faults, rare open small-scale NNW-SSE striking gravity folds (F_3) and an associated, rare, incipient westward inclined axial planar cleavage (S_3)(Von Veh, 1993). The emplacement of the post-orogenic alkaline granitic/syenitic plutons of the southwest-northeast trending Kuboos-Bremen line (including, from southwest to northeast, the Swartbank (not exposed), the Kuboos and the Tatasberg plutons)(Fig. 2.2) led to the D_4 event (Von Veh, 1993; Frimmel, 1995). The structural features related to the emplacement of the plutons within the Gariep Belt are best described from the aureole of the Kuboos pluton as the Swartbank pluton is not exposed, and the Tatasberg pluton intrudes basement rocks to the northeast. The D_4 event in the Gariep Belt is characterised by F_4 kink folds, conjugate folds, box-folds

and a strong S_4 schistosity, and is restricted to the aureole of the pluton (Von Veh, 1993; Frimmel, 1995). Reverse faults that mimic the Kuboos pluton contact and a southward plunging L_4 mineral lineation along the pluton contact are also related to the D_4 event (Von Veh, 1993).

The emplacement of the plutons led to low pressure, high temperature ($P \approx 2$ kbar, T possibly as high as 700°C, Frimmel, 1995) contact metamorphism (M_{con}). The contact aureole (of the Kuboos pluton) in the country carbonate rocks is evidenced by the development of diopside-, wollastonite-, anorthite- and grossular-bearing calc-silicate rocks and strongly depleted country rock $\delta^{18}O$ and $\delta^{13}C$ values induced by isotope exchange with magmatic waters (Frimmel, 1995). This aureole is restricted to a narrow (<100m wide) zone around a pluton with a diameter of ~30 km, indicating that convective heat transfer was limited (Frimmel, 1995). Where the country rock consisted of strongly foliated siliciclastic rocks, the aureole may be up to 3 km in width, indicating that convective heat transfer was more effective (Frimmel, 1995). The highest geotherm during the Gariepian orogeny (at least 45°C/km in the central PNZ) is coincident with the region where these post-orogenic intrusions were emplaced (Frimmel, 1995). Allsopp *et al.* (1979) obtained a Rb-Sr age of 530±12 Ma (based on an errorchron) and an U-Pb age of 520±12 Ma for the various alkaline plutons. Recalculation of the U-Pb ages (Frimmel and Frank, 1998) for the Kuboos pluton and the Bremen Complex yielded 524^{+186}_{-77} Ma (this age suffers from discordancy and is subject to a large error) and 521^{+24}_{-20} Ma, respectively.

The final stages of the transtensive phase led to the development of ESE-WNW striking normal faults, dykes, veins, fractures and joints (D_5) with local S_5 fracture cleavage development parallel to faults (Von Veh, 1993). A sub-vertical slickensiding L_5 lineation is associated with the D_5 phase of deformation (Von Veh, 1993).

A late phase of northeasterly and easterly directed compression, evidenced by northeast- to east-vergent folds and thrusts preserved only in the westernmost part of the Gariep Belt and in the Vanrhynsdorp inlier, has been indicated by Gresse (1994). This compressive

phase may have been the result of final collision and suturing in the Gariep Belt, possibly corresponding to the late Pan-African event (496±2 Ma, $^{40}Ar/^{39}Ar$ age, Gresse *et al.*, 1988) which also affected the Nama foreland deposits (Gresse, 1994).

Structural loading of the Kalahari Plate (related to convergent tectonics), with associated flexural fore-bulging and sea-level changes, led to the formation of a peripheral foreland basin in which the Neoproterozoic/Palaeozoic Nama Group was deposited (Germs and Gresse, 1991; Gresse and Germs, 1993)(Fig. 2.6). Palaeocurrent studies show a change in the source region from the lower to middle portions of the Nama Group (Germs and Gresse, 1991; Gresse and Germs, 1993). The lower Nama Group clastic sediments were derived from the Kalahari Plate to the east and northeast of the foreland basin, whereas the upper-middle and upper Nama Group molasse sediments were derived from the Gariep Belt in the west. Further to the north, the continual switching of source and current direction from the north and the north-north-west emphasises the interaction between the western (Gariep) and northern (Damaran) orogens during foreland deposition in that region (Gresse and Germs, 1993). The age of the base of the Nama Group is possibly 560-570 Ma (Gresse and Germs, 1993) and recent $^{207}Pb/^{206}Pb$ single zircon ages (Grotzinger *et al.*, 1995) indicate that sediment supply from the Gariep Belt had commenced shortly after the peak of metamorphism, that is, not later than ~540 Ma.

3. GARIEPIAN FLUIDS: FIELD EVIDENCE

In order to characterise the fluid evolution within the outer margin of the Gariep Belt, it is clear that a suitable sampling material containing relics of the various orogenic fluids and the pre-orogenic Rosh Pinah ore fluid is needed. Evidence for fluids and fluid flow is provided by veins (Fyfe *et al.*, 1979) which commonly consist of quartz and/or carbonate (Fyfe *et al.*, 1979; Yardley, 1989), hence samples of quartz and carbonate veins were collected for this study. This chapter aims to provide the geological framework, as evidenced by field relationships on both a localised (e.g. each sample locality) and a regional scale, within which interpretations of the analytically determined data can be constrained.

3.1 Quartz veins

Samples of various generations of orogenic quartz veins were collected from the outer margin of the Gariep Belt, from the farm Spitskop 111 in the north to near Lekkersing in the south (Fig. 3.1), the Vanrhynsdorp inlier (Appendix 2), and from the Southern Orefield No. 1 (370m level) of the Rosh Pinah mine (Fig. 3.2a). Sample material most likely to contain relics of the primary Rosh Pinah ore fluid (see 3.1.2) were collected from relatively less deformed areas of the mine (Figs 3.2b and 3.2c).

3.1.1 Relative abundance

Quartz veins are the most abundant type of vein present within the Gariep Belt and their relative abundance appears to be primarily controlled by the nature of the host rock: the siliciclastic rocks commonly host quartz veins, whereas such veins are scarce to generally absent in the carbonate rocks. This feature is clearly evident in the Bloeddrif Fault (Fig. 3.1) where the abundance of quartz veins hosted within the hanging-wall Wallekraal Formation siliciclastics contrasts with the lack of veins in the footwall carbonates of the

FIGURE 3.1 Geological map of the southern Gariep Belt, showing sample localities (see Appendix 1 for an enlarged version of the map).

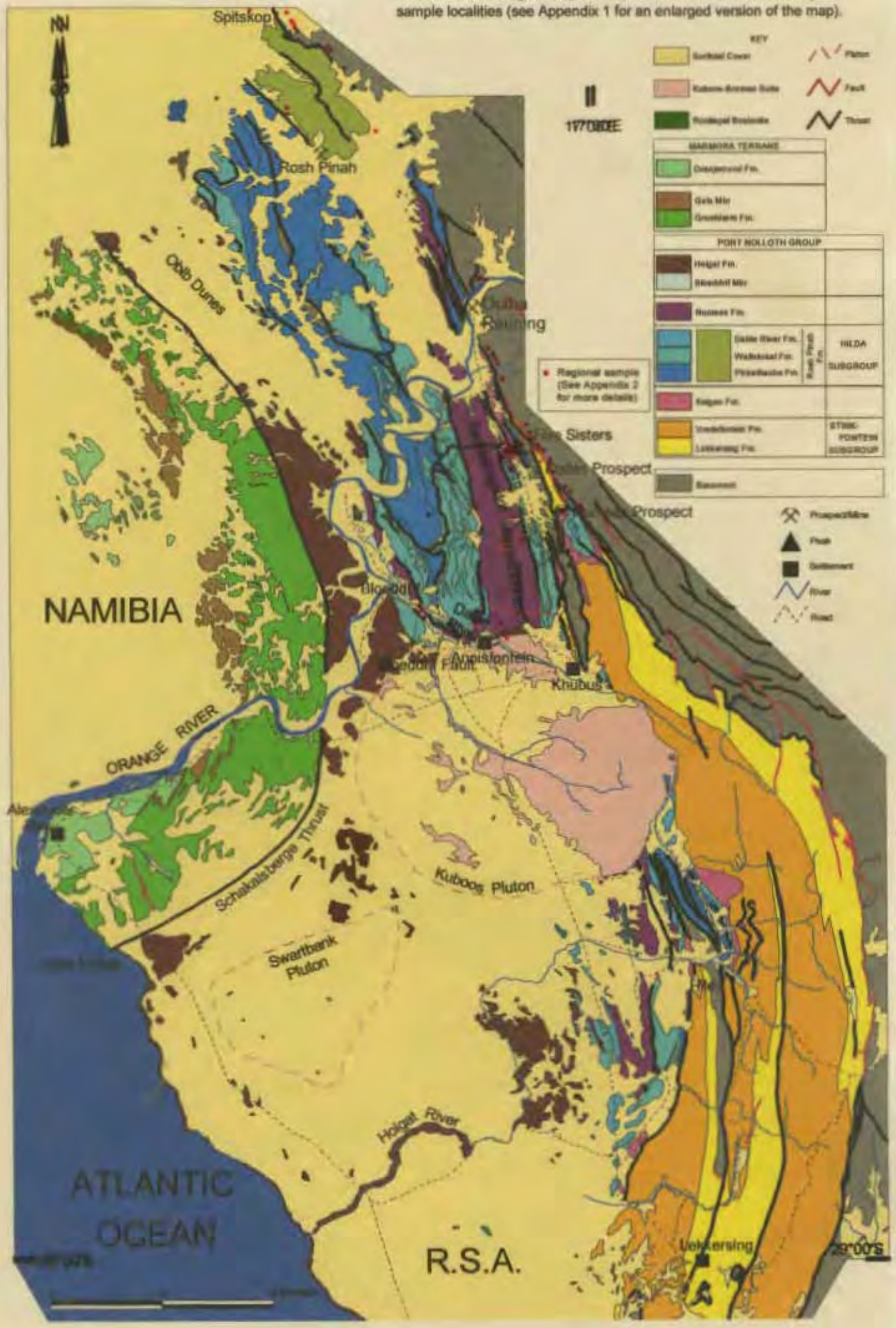

Bloeddrif Member (Fig. 2.3; Fig 3.1). Similarly the paucity of quartz veins hosted within the carbonate rocks making up the hills of the Five Sisters (Pickelhaube Formation) and the carbonates in the Dabie River north of Annisfontein (Dabie River Formation) contrasts with the abundance of quartz veins in the adjacent siliciclastic rocks. The relative abundance of the quartz veins hosted within siliciclastic units appears to be fairly uniform throughout the outer margin of the Gariep Belt.

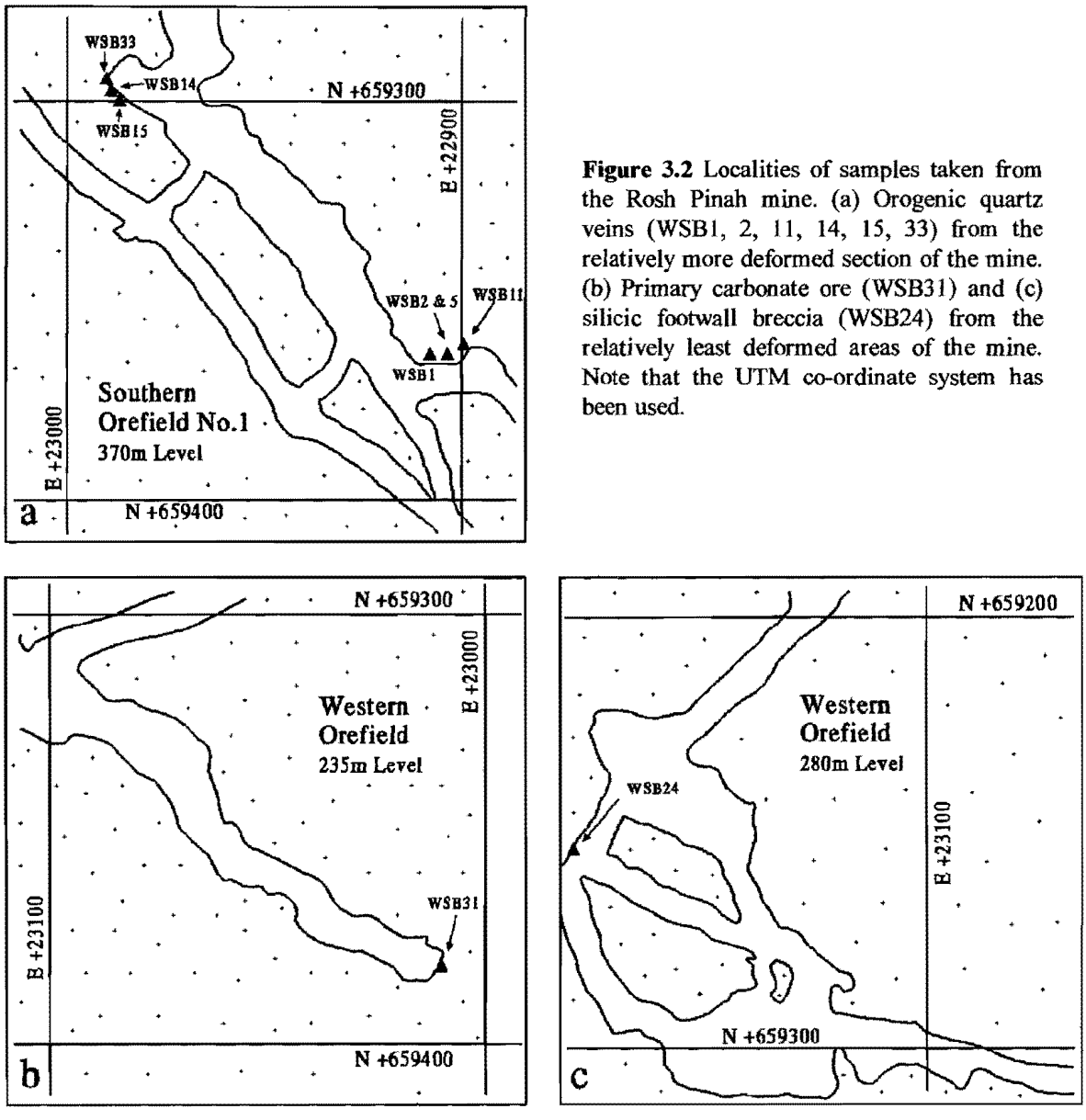

Figure 3.2 Localities of samples taken from the Rosh Pinah mine. (a) Orogenic quartz veins (WSB1, 2, 11, 14, 15, 33) from the relatively more deformed section of the mine. (b) Primary carbonate ore (WSB31) and (c) silicic footwall breccia (WSB24) from the relatively least deformed areas of the mine. Note that the UTM co-ordinate system has been used.

3.1.2 Pre-orogenic veins

The majority of the quartz veins present within the Gariep Belt are orogenic, but samples of pre-orogenic quartz veins were obtained from the Rosh Pinah mine. The predominantly quartz-rich footwall breccia (Fig. 3.3), syngenetic with respect to the ore body (Siegfried, 1990), has been crosscut (in places) by the various orogenic veins (see 3.1.3).

Figure 3.3 Silicic footwall breccia. Western Orefield 235m level, Rosh Pinah mine.

This breccia is considered to have been formed by the entrapment of hydrothermal ore-bearing solutions following earlier extensive silicification of the footwall rocks, and the subsequent adiabatic boiling of these solutions on their passage through the sea floor (Siegfried, 1990). Consequently the silicic footwall breccia most likely contains relics of the primary ore-forming fluids. Samples of primary ore were collected for similar reasons. The footwall breccia and primary carbonate ore samples were collected from the least deformed areas within the mine (WSB24 and WSB31; Figs 3.2b and 3.2c) and further sample details can be found in Appendix 2.

3.1.3 Orogenic veins

Four generations, which can be related to the various deformation events described in section 2.4, are recognisable. The earliest and most abundant generation, hosted within shear, fault and fracture zones, lies parallel to the regional S_1/S_2 foliation (undifferentiated here as S_1 and S_2 are typically coaxial throughout - see section 2.4), exhibits pinching and swelling within the foliation and is wrapped by the foliation (Fig. 3.3). This suggests that these veins were emplaced along the lines of weakness defined by the foliation, and were subsequently deformed within the foliation, implying a syntectonic (with respect to the regional foliation) origin for these veins.

Figure 3.3 D_1/D_2 quartz vein lying parallel to, and wrapped by, the S_1/S_2 foliation. Hosted by basement metavolcanics, near Kodas Prospect, Richtersveld National Park.

A summary of the structural data for both the earliest vein generation and the S_1/S_2 foliation is provided in Figs 3.4a and 3.4b, respectively (see Appendix 3 for a listing of structural data). The parallel relationship between the earliest vein generation (pole to best-fit-girdle: 333/02) and the regional S_1/S_2 foliation (pole to best-fit-girdle: 333/01) is evident in these figures. The pole to the best-fit-girdle for the regional S_1/S_2 foliation (333/01, this study) is comparable with the average pole to best-fit-girdle (339/05) for the regional

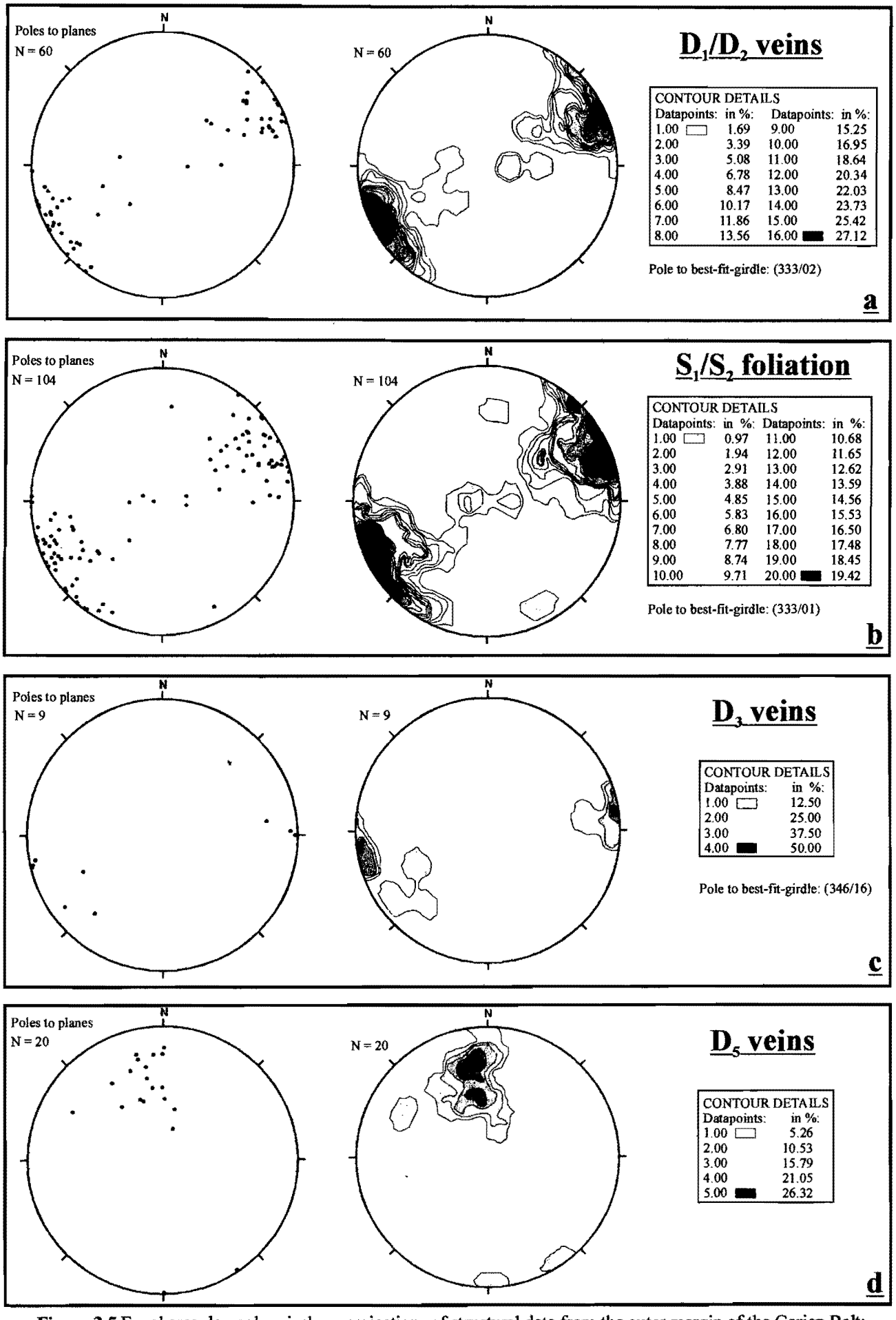

Figure 3.5 Equal area, lower hemisphere projections of structural data from the outer margin of the Gariep Belt: (a) all D_1/D_2 veins, (b) S_1/S_2 foliation, (c) all D_3 veins, (d) all D_5 veins. Note that all structural datapoints represent poles to planes.

foliation of Von Veh (1993; Domains IV, V, VII and VIIb). The steepening-up of the structures towards the east can be seen in Figs 3.4a and 3.4b, with the majority of the data points being structural data from the outer (eastern proximal subzone of Hälbich and Alchin, 1995) margin of the Gariep Belt. The cluster of data points in the centre of the stereonets represents the shallower dipping structures of the western distal subzone (after Hälbich and Alchin, 1995; samples WSB74, 75, 76) of this belt. The boundary between these two subzones is taken to be the western faulted limb of the Sendelingsdrif synclinorium (Hälbich and Alchin, 1995; see Fig. 3.1). The combined field observations and structural data for the earliest vein generation and the regional S_1/S_2 foliation suggests that these veins were formed during the peak of regional metamorphism (i.e. between D_1 and D_2 - see section 2.4). These veins are therefore referred to as D_1/D_2 quartz veins in this work.

The D_1/D_2 veins vary from small lenticular pods (<10cm in length and <2cm in thickness) to large pinch-and-swell quartz veins (>30m in length in places, and up to 3m in thickness). They consist predominantly of quartz (>90 vol.%, generally >99 vol.%), although varying amounts of ankerite (up to ~10 vol.%, commonly <5 vol.%), haematite (up to ~5 vol.%), chlorite (up to ~5 vol.%) and malachite (up to ~5 vol.%) are present in various combinations in different veins. Within the Rosh Pinah mine, coarse aggregates of remobilised sulphides (chalcopyrite, pyrite, galena and sphalerite; up to ~5 vol.%) are present within these veins (Fig. 3.5). The D_1/D_2 quartz veins hosted by a large shear zone between the Rosh Pinah Formation and the basement granites in southern Namibia are associated with epidote pods, pink Mn-bearing(?) carbonate veins, haematite, chlorite and ankerite of the same generation. These quartz veins are generally coarse-grained, vary from semi-transparent blue-grey to milky white and exhibit a granoblastic texture. They do not display extensional growth fibres. Rare D_1/D_2 quartz veins hosted in carbonate rocks are generally very thin (up to 6 cm thick), creamy white to dark brown in colour, and have a medium-grained sugary texture.

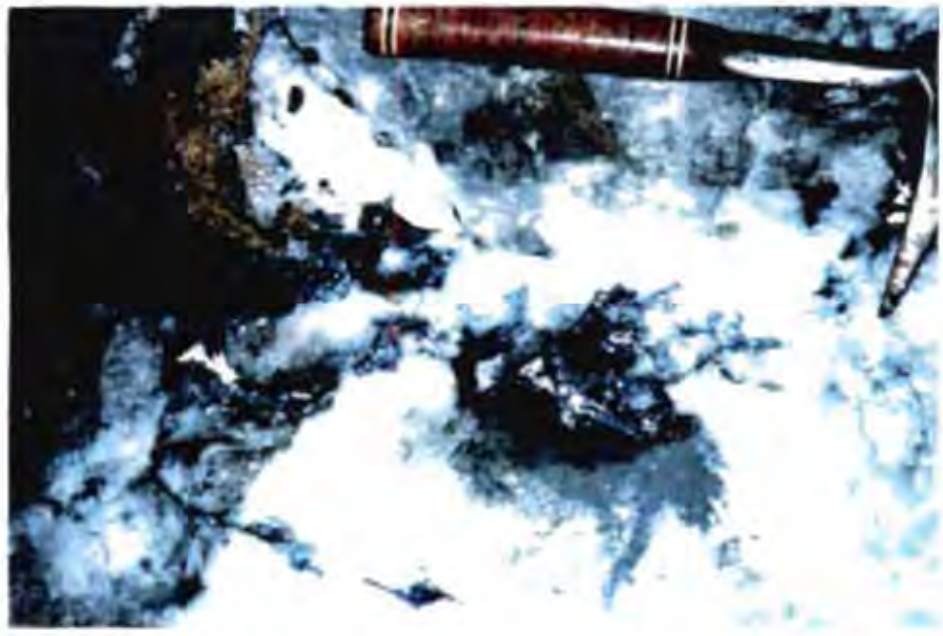

Figure 3.5 Coarse aggregates of secondary galena, pyrite and sphalerite (darker patches in association with the galena) hosted by a D_1/D_2 quartz vein. Southern Orefield 370m level, Rosh Pinah mine.

The second generation of veins has a generally NNW-SSE trend which almost lie parallel to that of the regional S_1/S_2 foliation (Figs 3.4b and 3.4c). These veins crosscut the regional foliation and exhibit undeformed extensional growth fibres normal to the generally straight vein margins (Fig. 3.6). The relationship between these veins and the regional foliation indicates that they are younger than the more abundant, deformed D_1/D_2 veins. The similarity between the orientations of these second-generation veins and the orientations of the structures related to the D_3 event (section 2.4) suggests that they are related to this event. This is supported by the fact that these veins are crosscut, in places, by E-W trending fractures and veins (the D_5 orientation - see section 2.4). Quartz veins with these characteristics are termed D_3 veins in this work.

The D_3 veins consist predominantly of quartz (generally 100 vol.%), although minor amounts of ankerite (1-2 vol.%) and haematite (<1 vol.%) are present in a few of the veins sampled. These veins exhibit a range in size from ~50 cm long and ~4 cm thick to ~10 m long and ~24 cm thick. No D_3 veins were found hosted in carbonate rocks, and none were observed within the Rosh Pinah mine.

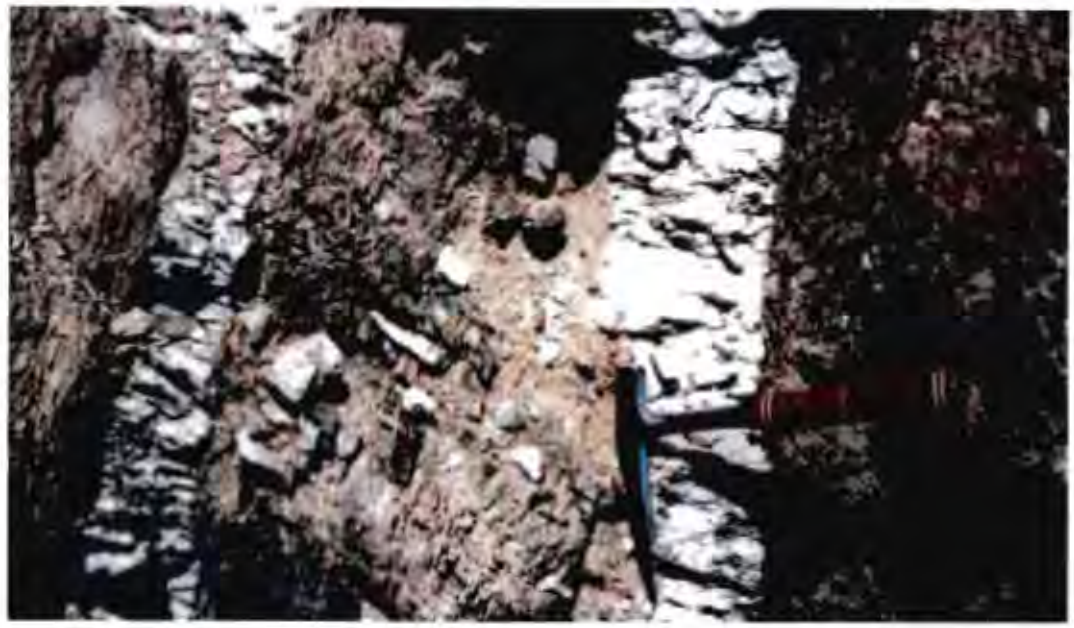

Figure 3.6 D_3 quartz veins hosted by basement granite, east of the Five Sisters, Richtersveld National Park. Note the undeformed nature of the veins (straight edges) and their crosscutting, yet nearly coaxial, relationship with the S_1/S_2 foliation (trending diagonally to the top right in this photo).

The third generation of veins is restricted to the aureole of the Kuboos Pluton, and crosscuts the S_1/S_2 foliation. These veins are transected by E-W trending features characteristic of the D_5 event. No relationship between these veins and the D_3 veins was observed, but the fact that these veins are restricted to the aureole and lie sub-parallel to the pluton contact suggests that they are related to the emplacement of the pluton. Veins with these characteristics are termed D_4 veins in this work.

The D_4 veins are generally transparent grey to milky white (with a pink tinge close to the pluton) and exhibit a coarse-grained granoblastic texture. Close to the pluton contact (<500 m) the D_4 veins consist of quartz (~80 vol.%) and pink feldspar (~20 vol.%) whilst further away (~1 km) the veins are characterised by quartz (>98 vol.%) and minor amounts of ankerite (<2 vol.%). The D_4 veins exist as irregularly shaped veins which appear to have utilised the foliation as a zone of weakness during their emplacement, hence they lie parallel to the regional foliation in places. The thickness along the length of the veins varies from 5 cm to 50 cm as a result of their irregular nature.

The fourth recognisable generation of quartz veins displays a general E-W trend (Fig 3.4d) with a moderately steep dip (~53°) to the south and exhibits crosscutting relationships with the regional foliation (Fig 3.7) and, in places, the D_3 veins. These veins

Figure 3.7 Looking west along a D_5 quartz vein that crosscuts the S_1/S_2 foliation (trending from left to right across the photo). The vein is hosted by Numees Fm diamictite and has truncated a clast of basement granite (outlined in green).

lie parallel to an E-W trending fracture cleavage that crosscuts the D_4 veins implying that, although no direct relationship between these veins and the D_4 veins was observed, they are younger than the D_4 veins. The fact that the orientations of these veins are similar to those exhibited by structures related to the D_5 event (section 2.4), combined with the structural observations, suggests that these veins are related to that event. Quartz veins exhibiting these characteristics are termed D_5 veins in this study. The D_5 veins are less abundant than the D_1/D_2 veins, but are more abundant than the D_3 and D_4 veins.

The fourth recognisable generation of quartz veins displays a general E-W trend (Fig 3.4d) with a moderately steep dip (~53°) to the south and exhibits crosscutting relationships with the regional foliation (Fig 3.7) and, in places, the D_3 veins. These veins

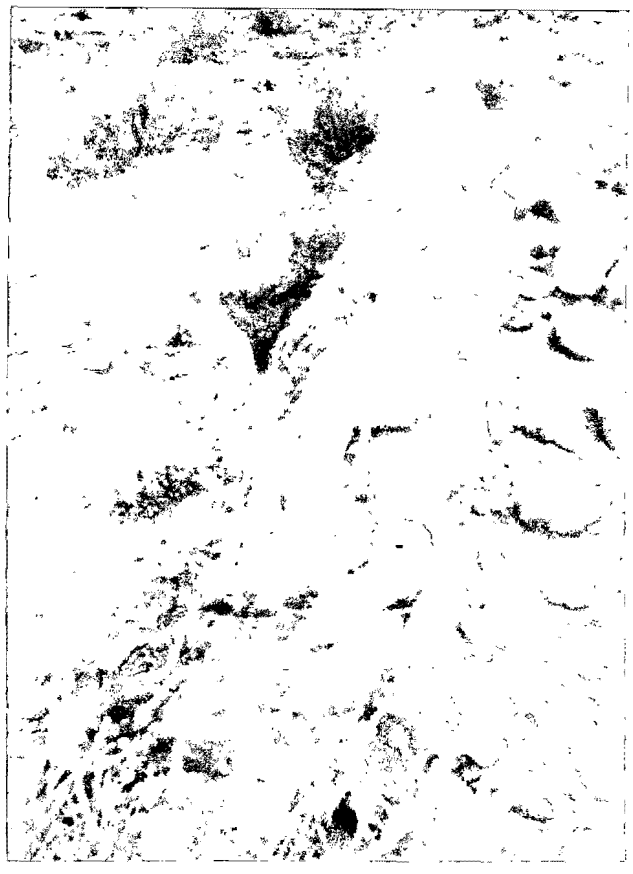

Figure 3.7 Looking west along a D_5 quartz vein that crosscuts the S_1/S_2 foliation (trending from left to right across the photo). The vein is hosted by Numees Fm diamictite and has truncated a clast of basement granite (outlined in green).

lie parallel to an E-W trending fracture cleavage that crosscuts the D_4 veins implying that, although no direct relationship between these veins and the D_4 veins was observed, they are younger than the D_4 veins. The fact that the orientations of these veins are similar to those exhibited by structures related to the D_5 event (section 2.4), combined with the structural observations, suggests that these veins are related to that event. Quartz veins exhibiting these characteristics are termed D_5 veins in this study. The D_5 veins are less abundant than the D_1/D_2 veins, but are more abundant than the D_3 and D_4 veins.

The D_5 veins are generally milky white (rarely transparent blue-grey), coarse-grained, straight-edged veins consisting of quartz (generally 100 vol.%, although trace amounts of haematite and ankerite are present in a few of the samples). The D_5 veins are generally rectangular (with the pod shape exhibited by WSB84 being the only exception) in cross-section and maintain their thickness along their length, except at the extremities of the veins, where some of the veins taper to a point. Extensional growth features are developed in several of the veins, and the overall texture is granoblastic. The veins vary from ~9 cm to ~1 m in thickness and from ~1 m to >25 m in length.

3.2 Carbonate veins

These veins are regionally far less abundant than the quartz veins, and only four orogenic carbonate veins, from a variety of different host rocks (basement granite, WSB123; Kaigas Fm, WSB91; Pickelhaube Fm, WSB113 and Numees Fm, WSB137), were found (Fig. 3.1). The carbonate veins exhibit similar relationships to the regional S_1/S_2 foliation as their quartz counterparts (section 3.1), and veins related to the D_1/D_2 as well as the D_5 events were recognised (Appendix 2). These veins are comprised of 100 vol.% calcite, and are generally creamy white in colour, although the vein (WSB123) found within a shear zone between the Rosh Pinah Formation and the basement granite in southern Namibia is pink. The carbonate veins are smaller (up to ~25 cm thick and ~1.5 m in length) than the quartz veins.

4. ANALYTICAL TECHNIQUES

4.1 Fluid Inclusion Microthermometry

A fluid inclusion study was undertaken in order to characterise the physico-chemical (i.e. salinity, nature of dissolved ions, density of the fluid, nature of any gaseous phases present) properties of the vein-forming solutions. Thin (60-90 μm) doubly polished sections were prepared from selected samples using techniques similar to those outlined in Barker and Reynolds (1984). These techniques ensure that the sample is not subjected to temperatures exceeding 30°C during cutting, grinding and polishing. A FLUID INC.-adapted U.S.G.S. gas-flow heating-freezing system, which operates by passing cooled N_2 gas or heated air directly above or beneath the sample, was used to determine temperatures of various phase changes. Synthetic fluid inclusions in quartz, provided by SYNFLINC (Sterner and Bodnar, 1984), were used to calibrate the system at –56.6°C (the triple point of CO_2), 0.0°C (the triple point of pure H_2O), and 374.1°C (the critical point of pure H_2O). Reproducibility of measurements during calibrations was within 0.2°C of the –56.6°C standard, within 0.1°C of the 0.0°C standard and within 1.0°C of the 374.1°C standard. The accuracy of the system, provided that the thermocouple tip is not farther than 2.5mm from the inclusion analysed thus minimising the effects of thermal gradients (e.g. Roedder, 1984), is estimated to be better than ±0.2°C below 0.0°C, and better than ±1.0°C on heating. In order to obtain the optimal balance between quality and quantity, the resolution of the system for the heating phase was chosen to be within ±2.5°C.

It has been shown that both the isochoric and the isoplethic nature of fluid inclusions in quartz may be changed after their entrapment by numerous possible mechanisms (e.g. Roedder, 1984; Sterner and Bodnar, 1989; Barker, 1995; Vityk and Bodnar, 1995), making the interpretation of such data extremely difficult. In order to avoid erroneous and therefore meaningless salinity and homogenisation temperature (T_h) measurements, this study employs the general techniques and philosophy of conducting a fluid inclusion study as outlined in Goldstein and Reynolds (1994). After petrographically defining suitable fluid inclusion assemblages (e.g. microfractures and planes), microthermometric analyses,

employing the cycling technique, were made. Data were collected from fluid inclusions of different sizes and shapes existing in various fluid inclusion assemblages (e.g. healed microfractures and clusters) showing consistent vapour to liquid ratios. Data from each fluid inclusion trail with less than ±10°C variability were then averaged to produce a single data point for that trail. In this way, erroneous data related to post-trapping modifications like thermal re-equilibration and necking-down after a phase change could be removed from the dataset.

4.2 Stable Isotope Analysis

Oxygen and hydrogen-deuterium stable isotope analyses were conducted on selected quartz and carbonate veins, as well as a few selected host-rock samples in order to assist in the characterisation of the Gariepian fluids and their evolution.

4.2.1 Oxygen Isotopes

Silicates

Selected vein samples were crushed to ~1.5 mm in size from which quartz chips (optically >99% pure) were handpicked with the aid of a binocular microscope. The quartz chips were cleaned in de-ionised water and acetone prior to being crushed to a fine powder (generally <200#, with the coarsest grains passing through the 120# sieve) in an acetone-cleaned agate mortar and pestle. Although evidence in Borthwick and Harmon (1982) suggests that the sample should be crushed to <200# (<0.074 mm), Vennemann and Smith (1990) showed that the relatively coarser grain size fractions of ~40 to 120# (0.420 mm to 0.125 mm) are suitable when using ClF_3 as a reagent (see below). The powders were then dried in an oven at 110°C. A portion of each powdered sample was bathed in dilute HCl as a check for the presence of carbonate minerals that may have been missed in the hand picking. No effervescence was noted in any of the quartz vein samples.

It was decided that the host-rock samples for selected veins would be analysed as bulk rock samples in order to assess the degree of host-rock control on the fluids in the Gariep Belt. These samples were subjected to a similar process to that used for the quartz vein samples outlined above, except that they were not washed in acetone, nor treated with HCl. All of the host-rock samples were crushed to <200#.

The extraction of oxygen from silicates and oxides, as conducted at the Department of Geological Sciences, University of Cape Town (UCT), employs the use of a vacuum line built to the principles of Clayton and Mayeda (1963). Further details can be found in Borthwick and Harmon (1982), Vennemann and Smith (1990) and Harris and Erlank (1992). An aliquot of between 7 and 12 mg of each sample was loaded into nickel reaction vessels, which were then evacuated at 200°C to ~10^{-5} mbar for 2 hours. The samples were then reacted with approximately a 7:1 molar excess of ClF_3 (Borthwick and Harmon, 1982; Vennemann and Smith, 1990) at 550°C for 3 h for quartz and for 7 h for host-rock samples. The oxygen extraction line at UCT consists of ten reaction vessels and during each run two splits of the quartz standard NBS-28 and eight samples were analysed. Oxygen release can be described by the reaction:

$$3SiO_2(s) + 4ClF_3(g) \rightarrow 3SiF_4(g) + 2Cl_2(g) + 3O_2(g)$$

The extracted oxygen from each reactor vessel was sequentially converted to CO_2 by passing it over a hot platinized carbon rod:

$$C(s) + O_2(g) \rightarrow CO_2(g)$$

The amount of CO_2 produced was then measured manometrically prior to being collected in glass sample bottles or break-seal tubes. The line is "dumped" after each run by passing the residual gases (excess reagent and SiF_4) through a heated KBr trap (to remove the fluorine) and freezing them into a waste trap. Residual powders (e.g. AlF_3, CaF_2, FeF_2, NaF, MgF_2 etc. - only present after whole rock and incomplete extractions) are routinely dumped from the reaction vessels.

The $^{18}O/^{16}O$ isotope ratios of the CO_2 produced by the extraction procedure were determined using a Finnigan MAT252 mass spectrometer (housed at the Department of Archaeology, UCT). The average NBS-28 values were used to convert the raw data to the V-SMOW (Vienna Standard Mean Oceanic Water) scale using the accepted value of 9.64‰ for NBS-28 (Coplen *et al.*, 1983) and the data are reported in the δ notation where:

$$\delta^{18}O = [(^{18}O/^{16}O_{(Sample)} - {}^{18}O/^{16}O_{(Std)}) / (^{18}O/^{16}O_{(Std)})] \times 1000$$

The average difference between 12 pairs of NBS-28 determinations obtained during this study was 0.11‰. According to Vennemann and Smith (1990) a minimum O_2 yield of 95% is required in order to achieve the accepted analytical error of ±0.15‰. The O_2 yields for quartz samples in this study were all >95%, as were those for the NBS-28 standards.

Carbonates

Selected carbonate vein samples were hand crushed down to chips ~3 mm in size which were rinsed 3 times in 18 MΩ.cm water (water passed through a MilliQ deionisation purification unit; hereafter referred to as MilliQ water). These chips were then washed with MilliQ water in an ultrasonic bath for 30 minutes after which they were crushed to a fine powder using an agate mortar and pestle. This mortar and pestle was cleaned 6 times before each sample by rinsing (using MilliQ water) and "crushing" (simulating the crushing process, with only MilliQ water in the mortar).

The carbonate samples (40-50 μg) were loaded into the sample carousel of a Finnigan MAT Automatic Carbonate Preparation Device, and a brief outline of the process that occurs within this device is given below. Each sample is reacted with a fresh aliquot of acid (99% H_3PO_4 at 70-73°C) liberating CO_2 and H_2O by the reaction:

$$2H_3PO_4(aq.) + 3\ CaCO_3(s) \rightarrow Ca_3(PO_4)_2(aq.) + 3H_2O(l) + 3CO_2(g)$$

The CO_2 and H_2O are thermally separated using a multi-loop trap, and the CO_2 is then released into the mass spectrometer. Isotope ratios were determined using a Finnigan MAT252 mass spectrometer, and raw $\delta^{18}O$ values were corrected using the in-house laboratory standard NM 95 ($\delta^{18}O$ = 25.10‰) which has been calibrated to the V-SMOW scale using the NBS-19 carbonate standard ($\delta^{18}O$ = 28.65‰; Coplen *et al.*, 1983). The oxygen that has been liberated from the reaction (above) will fractionate between the CO_2 and H_2O end products. Consequently, in order to obtain the true $\delta^{18}O$ value of the sample, a corrective fractionation factor must be applied to the $\delta^{18}O$ value of the acid-liberated CO_2. The fractionation factor between the sample carbonate and the extracted CO_2 at 71°C is given by the ISODAT software manual as $\alpha_{Calcite\text{-}CO2}$ = 1.0081069. The precision is better than ±0.2‰, as estimated from repeated analyses of standard NM 95.

4.2.2 Hydrogen-Deuterium Isotopes by Decrepitometry

A few quartz vein samples were analysed by this technique in order to obtain a direct measurement of the D/H ratio of the fluid inclusions within the quartz veins. Samples with the greatest possibility of containing of only one generation of fluid inclusions (as evidenced by microthermometry measurements) were selected and were crushed down to chips ~3-5 mm in size. These chips were then cleaned in de-ionised water before being dried in an oven at 110°C.

Hydrogen extraction, adhering to the general principles of Coleman *et al.* (1982), was conducted using a vacuum line (housed at the Department of Geological Sciences, UCT) built to the principles of Vennemann and O'Neil (1993). The quartz chips (between 3 and 4g) of each sample were loaded, together with pre-roasted quartz wool, into a quartz tube which was placed into a resistance furnace. The line was then evacuated (~10^{-2} mbar) at 120°C for 20 minutes after which the sample was heated (incrementally) at 300°C for 5 minutes, then 400°C (5 minutes), then 500°C (5 minutes), and ultimately 600°C for 5 minutes. Water and CO_2 (from each sample) were separated using a propanol-liquid nitrogen 'slush' and were then collected in glass break-seal tubes. Excess Zn shavings

(about five times that normally required to reduce the water; Chris Harris, *pers. comm.*, 1997) were placed in those tubes used to collect H_2O. Hydrogen extraction was completed by the reaction of water with zinc

$$H_2O(l) + Zn(s) \rightarrow ZnO(s) + H_2(g)$$

in a furnace at 480°C for 10 minutes.

D/H ratios were measured using a Finnigan MAT252 Mass Spectrometer. The data were calibrated to the V-SMOW scale using an internal water standard (CTMP, δD = -9‰) and were normalised so that SLAP (Standard Light Antarctic Precipitate) gave a value of -428‰ on the V-SMOW scale, as recommended by Coplen (1988). The analytical error is ±1‰ (Chris Harris, *pers. comm.*, 1997).

4.3 Crush-leach Analysis of Fluid Inclusions

This technique was used to provide a direct measure of the ionic composition of the fluid present within the fluid inclusions. As a result of the low concentrations (several ppm) of ionic species within the fluid inclusions (Roedder, 1984), great care was necessary not to introduce contamination at any stage of the process from sample preparation to data collection.

Selected samples of quartz and carbonate veins, secondary vein-hosted sphalerite, silicic footwall breccia and primary ore were crushed down to chips of ~1-2 mm in size. Hand-picking (in those samples which were not too fine-grained) with the aid of a binocular microscope ensured an optical purity of 100% for each chip. It was decided to obtain a bulk analysis for the very fine-grained samples (generally ore and silicic breccias from the Rosh Pinah mine), because handpicking was extremely difficult. The chips were placed in glass vials and rinsed 3 times in MilliQ water (see section 4.2.1) before being washed (in MilliQ water) in an ultrasonic bath for 60 minutes. The samples were dried in an oven at 50°C.

The principles of, and problems associated with, the liberation (from fluid inclusions) and subsequent analysis of a leachate by the crush-leach process are discussed in Roedder (1984). The method used in this study is similar to the process described in Kesler *et al.* (1996) and Chetty (1998) and is outlined below. The leachate compositions reported in this study were obtained from 400 to 700 mg of each cleaned sample that were then crushed in MilliQ water (5ml) using a boron-carbide mortar and pestle. Leachates and blanks (see below) were analysed for Li^+, Na^+, NH_4^+, K^+, Mg^{2+}, Mn^{2+}, Ca^{2+}, F^-, Cl^-, NO_2^-, Br^-, NO_3^{2-}, PO_4^{3-} and SO_4^{2-} with a Dionex DX300 Gradient Ion Chromatography System housed at the Department of Geological Sciences at UCT.

MilliQ water blanks were run at the start of each day's analysis, and whenever the water tank had to be refilled. After confirming the purity of the water (in terms of ionic composition), all of the glassware and syringes to be used were rinsed in MilliQ water. The equipment used for this technique was isolated from other users as a further precaution against contamination. The mortar and pestle were cleaned 12 times simulating the crushing process by 'crushing' MilliQ water. The twelfth 'crush' was then collected and run on the ion chromatograph (IC) to check the cleanliness of the mortar and pestle. The fourth 'crush' usually yielded a chromatograph the same as that of the MilliQ water). Standards of different concentrations (5 levels) of the important ions were prepared and run after the water blanks. Comparing the theoretical concentrations of the standards (and their corresponding intensities) with those determined by running the standards on the IC (using the Calplot option of the AL-450 v. 3.31 software package, ©Dionex Corporation, 1992) consistently yielded regression coefficients (R^2) of better than 0.999 (generally better than 0.9999) for each ion. The mortar and pestle were cleaned 12 times with MilliQ water between each sample using this 'crushing' method, and blanks were collected and run after every three samples. The syringe used for sample injection was cleaned with MilliQ water a total of 40 times between each sample and blank and syringe blanks were frequently run on the IC (always producing chromatographs identical to that of the MilliQ water). The extent of the contamination adsorbed to the surface of the samples was checked by submerging the aliquot of sample to be crushed in MilliQ water, swirling it around, and then running this water on the IC. The resultant chromatographs were identical to those of the MilliQ

water. The leachates were filtered through a 0.5 μm Millex-LCR_{25} filter, and 3-3.5 ml was stored in Nalgene bottles for the anion runs as were all blanks that were run during the collection of the cation data.

Cations were run using a sample loop of 25 μl, an HPIC-CG12A guard column, an HPIC-CS12A separator column and a cation self-regenerating CSRS-I supressor. The eluant used for the cation runs was 22 mM methane sulphonic acid (M.S.A.) at a flow rate of 1 ml/min with an expected background conductivity of 4-8 μS. Anions were run using both a 50 μl and a 200 μl sample loop. The latter was used in order to increase the sensitivity of the system so as to identify any bromine that was not detected using the 50 μl loop. An HPIC-AG4A guard column, an HPIC-AS4A separator column and an Anion self-regenerating ASRS-I supressor were used during the anion runs. The eluant used during the anion runs is a combined carbonate-bicarbonate eluant (1.80 mM Na_2CO_3, 1.70 mM $NaHCO_3$) with a flow rate of 2 ml/min. The expected background conductivity for the anion runs is 15 to 20 μS. Concentrations of the various ions present in the blanks are summarised in Table 4.1 below.

Table 4.1 Table of values of ionic species as determined in various blanks.

ION	HIGHEST VALUE (ppm)	AVE. VALUES (ppm)
Li^+	0.002	0.000 (n=16)
Na^+	0.100	0.023 (n=16)
NH_4^+	0.062	0.029 (n=16)
K^+	0.033	0.009 (n=16)
Mg^{2+}	0.114	0.047 (n=16)
Mn^{2+}	0.021	0.012 (n=16)
Ca^{2+}	0.282	0.157 (n=16)
F^-	0.000	0.000 (n=17)
Cl^-	0.206	0.048 (n=17)
NO_2^-	0.000	0.000 (n=17)
Br^-	0.000	0.000 (n=17)
NO_3^{2-}	0.000	0.000 (n=17)
PO_4^{3-}	0.000	0.000 (n=17)
SO_4^{2-}	0.000	0.000 (n=17)

4.4 SEM-Cathodoluminescence

Cathodoluminescence (CL) microscopy allows for the identification of textures not normally visible when using standard optical or scanning electron microscope (SEM) techniques (Gartz *et al.*, 1995). As a result of this, it was decided to use this technique to view several sections containing the quartz vein/host-rock boundary in order to assess the nature of the contact and the degree (if any) of contamination by host-rock quartz within the vein quartz.

Standard polished probe sections (~60 μm) were prepared and cleaned with ethanol prior to being loaded into the Cambridge Stereoscan S440 SEM housed at the Electron Microscope Unit at UCT. This SEM is fitted with backscatter electron (BSE), secondary electron (SE), Leica CL and Oxford Mono CL detectors. An electron beam is used to excite the sample which, if subjected to high enough energy levels, results in the emission of CL (Gartz *et al.*, 1995). Other detectable emissions include x-rays, secondary electrons and backscatter electrons (D. Gerneke, *pers. comm.*, 1997). All work was conducted at room temperature, with an acceleration voltage of 15 kV being applied to overcome the threshold voltage of 10 kV for quartz, below which no CL emission occurs (Marshall, 1984). CL images were collected (with the Leica CL detector) using a beam current of approximately 20-85 nA, and the magnification used was between 200 times and 880 times. More details on the application of the SEM-CL technique to quartz samples (especially the analysis of CL emission spectra) can be found in Gartz *et al.* (1995).

4.5 Raman Microspectrometry

This technique was employed to complement the microthermometry technique by investigating the nature of other gaseous species present within the CO_2 inclusions. The presence of such species was indicated by the lowering of the melting temperature of pure CO_2 during microthermometry measurements.

A Microdil-28 multichannel Raman microspectrometer (manufactured by Dilor Co., Lille, France) housed at the Institute for Earth Sciences at the Free University (Amsterdam) was used and technical descriptions of the instrument can be found in Delhaye *et al.* (1982), Deffontaine *et al.* (1984) and Burke and Lustenhouwer (1987).

The following outline of the technique is adapted from Burke and Lustenhouwer (1987). An argon ion laser (using the 514.5 nm green line) is used to irradiate the sample (the standard doubly polished sections used for microthermometry; see section 4.1) by means of a high magnification (50 or 100X) objective mounted on an optical microscope operating in the reflected light mode. The scattered light is collected through the same objective and directed to the multichannel detector system via an *F*/5 double monochromator and a stigmatic spectrograph. The multichannel detector system enables the simultaneous recording of a spectral range of ~300-400 cm^{-1}, depending on the wavelength position, with a spectral resolution of ~3 cm^{-1}. This characteristic of simultaneous detection allows for a very short counting time (1-5 s) in order to obtain a spectrum of any given spectral range. This, in turn, allows for the accumulation of a number of recordings of each spectrum which result in an averaged spectrum with a good signal to noise ratio. After the detection of the presence of components (other than CO_2) by Raman analysis of the vapour phase, spectra of each component were obtained and averaged, providing a quantitative analysis for each component. Spectra were obtained using a laser power of 1500 mW with an acquisition time of between 4 s and 6 s and were averaged from 10 accumulations each.

5. RESULTS

In view of the known variation in the peak metamorphic grade within the external Gariep Belt (Frimmel, 1995; section 2.4), any presentation and subsequent interpretation of (at least) the D_1/D_2 data should be subjected to this geological control. For the purposes of this study, the external Gariep Belt is subdivided into four areas: northern (north of Sendelingsdrif), central (south of Sendelingsdrif and north of the Kuboos Pluton), southern (south of the Kuboos Pluton in the Lekkersing area) and Vanrhynsdorp (the inlier to the west of Vanrhynsdorp) areas. The subdivision of the Gariep Belt south of the Orange River and north of Port Nolloth into a central and a southern area has been made purely for the sake of simplicity in terms of data presentation.

5.1 Fluid Inclusion Study

Twenty-two quartz vein samples of various generations, both pre-orogenic (silicic footwall breccia from the Rosh Pinah mine) and orogenic (samples of the 5 deformation-related veins on both a regional scale and from the mine), were selected for the fluid inclusion studies.

5.1.1 Petrography

The majority of the fluid inclusions within these samples are of secondary origin, being hosted within microfractures. Numerous inclusions of unknown origin (e.g. isolated clusters, isolated inclusions) do also occur. Except for the possibility of a few of the larger isolated inclusions (with completely random distributions in three dimensions) representing primary inclusions (Roedder, 1984), no direct evidence for the presence of such inclusions was found. A complete description of every fluid inclusion analysed is provided in Appendix 4. Five different types of fluid inclusions were identified.

Type I - Aqueous two-phase (L_{aq} + V_{aq})*

These are by far the most abundant type of inclusion and are present within all samples. These inclusions vary in size from ~1 μm to ~36 μm in maximum dimension and are generally colourless. Type I inclusions exhibit a variety of different shapes: irregular, ovoid, rectangle, square, triangle, rhombus, parallelogram, trapezium, diamond and negative crystal. The vapour to liquid (V/L) ratio varies between 5 vol.% and 25 vol.% (volume percentages estimated using Fig. 4-10 from Roedder, 1984) and a rough V/L ratio trend of $D_4 > D_1/D_2 > D_3 > D_5$ is evident.

Type II - Carbonic three-phase (L_{aq} + L_{carb} + V_{carb})*

These are the next most dominant type of inclusion present, are generally colourless with a dark "double bubble" (carbonic vapour and liquid) and comprise variable proportions of aqueous and carbonic components. The volume proportions of carbonic to aqueous vary between 15 vol.% and 95 vol.% at the temperature of homogenisation of CO_2 (T_hCO_2), although it must be stressed that these values are estimates at best in view of the uncertainty in the third dimension. Type II inclusions have similar shapes to Type I inclusions and their size ranges from less than 3 μm to ~68 μm in maximum dimension. Type II inclusions were found together with Type I inclusions in several microfractures.

Type III - Carbonic two-phase (L_{carb} + V_{carb})

These rare inclusions were observed in several regional orogenic quartz vein samples. They are generally dark in colour and display variable shapes and sizes (~2 μm to ~18 μm) similar to those of Types I and II. The V/L ratio varies between ~18 vol.% and 50 vol.% and the coexistence of Type III inclusions with Type II inclusions within the same cluster or microfracture was observed in places.

* aq = aqueous, carb = carbonic

Type IV – Carbonic four-phase (L_{aq} + L_{carb} + V_{carb} + S_{salt})

These inclusions are restricted to the silicic footwall breccia of the Rosh Pinah mine and contain a dark "double bubble" of carbonic-rich liquid and vapour as well as a transparent solid phase. These solid phases are most likely daughter crystals as they consistently occupy similar volumetric proportions within their host inclusions (Roedder, 1984), too coincidental for them to be solid inclusions. The estimated V/L ratio of carbonic to aqueous components varies between 15 vol.% and 50 vol.% (at T_hCO_2) whereas the daughter crystal consistently occupies between 5 vol.% and 10 vol.% of the inclusion. Type IV inclusions exhibit a range of shapes that are similar to those of Type II inclusions, and vary from ~2 μm to ~13 μm in maximum dimension. These inclusions occur in a variety of different assemblages including isolated inclusions that are large in relation to their host grain (quartz), isolated groupings of inclusions, and trails of inclusions that all seemingly terminate at the edge of the host quartz grain. No inclusions were observed in the adjacent carbonate grains. These observations appear to indicate a primary and/or pseudo-secondary (in the sense of Roedder, 1984) origin for the Type IV (and Type II) inclusions in the footwall breccia. The termination of the trails at the interface between the quartz and carbonate may just be a function of the different strengths of the two minerals and hence their ability to maintain trapped inclusions. Consequently an unknown origin has been ascribed to inclusions with these characteristics. The coexistence of Type II and Type IV inclusions was observed in several assemblages.

Type V – Aqueous three-phase (L_{aq} + V_{aq} + S_{salt})

These are the least abundant fluid inclusion type observed (only 4 inclusions!) and are only present within the silicic footwall breccia (Rosh Pinah mine). They contain both a vapour bubble (~15 vol.%) and a daughter crystal (~15 vol.%). Shapes similar to those of Type II inclusions are exhibited, and these inclusions vary between ~4 μm and ~5 μm in size. Type V inclusions were found in the same array as several Type II inclusions.

5.1.2 Microthermometry

Type I inclusions

These inclusions were cooled through –70° and the following phase changes were observable on heating: first melting of ice, final melting of ice and total homogenisation. The temperatures at which these various phase changes occurred were recorded and are discussed below. The Type I inclusions are further subdivided into Type Ia (most abundant) and Type Ib inclusions for reasons discussed below.

The temperature of first melting (eutectic temperature or T_e) is reported as the lowest temperature at which liquid is definitely visible (after the suggestion of Goldstein and Reynolds, 1994). Larger inclusions clearly show a gradual change to the "orange peel" texture through heating, whilst the T_e measurements in the smaller inclusions (using a visible change in size and shape of the vapour bubble) were more difficult to obtain (and in many cases impossible). The T_e data for the D_1/D_2 veins, irrespective of geographical location, generally range between -40°C to -30°C with minimum and maximum values obtained being <-60°C and <-17°C, respectively. The first melt observable in the Type I inclusions hosted within the D_3 veins ranges from <-60°C to <-30°C, with most of the observations ranging between -40° and -30°C. The Type I inclusions in the D_4 and D_5 veins exhibit similar T_e values, ranging from <-56°C to <-29°C and <-45°C to <-12°C, respectively, which also tend to cluster within the -40°C to -30°C interval. The T_e values from the D_3, D_4 and D_5 veins are essentially the same. Note that no distinction has been made between the Type Ia and Ib inclusions here as their T_e data are essentially the same. First melting was observed in the pre-orogenic sample at less than -50°C.

The visual disappearance of ice was readily observable in most of the larger Type I inclusions (>~10 μm), followed by the "freeing" of the vapour bubble whilst the temperature of final melting of ice ($T_m$ice) in the smaller inclusions was recorded when the bubble finally "jerked" free. Temperature cycling confirmed the $T_m$ice values. Numerous Type I inclusions from the D_1/D_2, D_4 and D_5 veins exhibit final melting temperatures

greater than 0°C, indicating the presence of a gas hydrate or clathrate (Roedder, 1984; Goldstein and Reynolds, 1994). This suggests the further subdivision of the Type I inclusions into Type Ia (Type I inclusions with $T_m$ice values less than 0°C) and Type Ib (those Type I inclusions with final melting temperatures indicative of the presence of a clathrate) inclusions. In all cases the temperature of the final phase change observed (temperature of total homogenisation, T_hH_2O) was characterised by the disappearance of the vapour bubble (i.e. homogenisation to the liquid phase).

Figs. 5.1 and 5.2 show the range of $T_m$ice and T_hH_2O values for Type Ia inclusions present within the various quartz vein generations. The data points on these plots are the average values for each different fluid inclusion trail, i.e. each datum point represents a different trail (see section 4.1). The D_1/D_2 data from the northern area (Fig. 5.1a) exhibit a wide range of T_hH_2O values (107°C to 274°C) clustering in two apparent populations in terms of $T_m$ice (-11.9°C to -10.1°C and -8.1°C to -0.6°C, respectively). It should be noted that the individual ranges in T_hH_2O data for each sample plotted (with the exception of WSB1 from which data collection was limited by the general lack of inclusions larger than 1μm) are essentially the same as the overall range in this dataset. Data from the D_1/D_2 veins from the central area (Fig. 5.1b) show a narrower range of both $T_m$ice (-8.9°C to -0.3°C), mostly between -4.5°C and -0.3°C, and T_hH_2O (147°C to 216°C) than those from the northern area. The highest T_hH_2O values recorded from the central area are lower than those from the northern area, whereas the central veins tend to have higher $T_m$ice values. Type Ia inclusions present within the D_1/D_2 sample from the southern area (WSB149) exhibit the lowest maximum T_hH_2O values of the four areas (Fig. 5.1c). The total homogenisation data range between 146°C and 174°C. The T_hH_2O data for these veins, ranging between -4.6°C and -3.0°C, are similar to those from the central area D_1/D_2 veins. T_hH_2O data from the Vanrhynsdorp area range between 162°C and 263°C, with the majority of the data occurring between 215°C and 263°C (Fig. 5.1d). Apart from the single datum point at -8.2°C, the $T_m$ice values form a tight cluster ranging between -3.6°C and -0.8°C.

The D_3 veins (Fig. 5.2a) show a spread of T_hH_2O and $T_m$ice data varying between 157°C

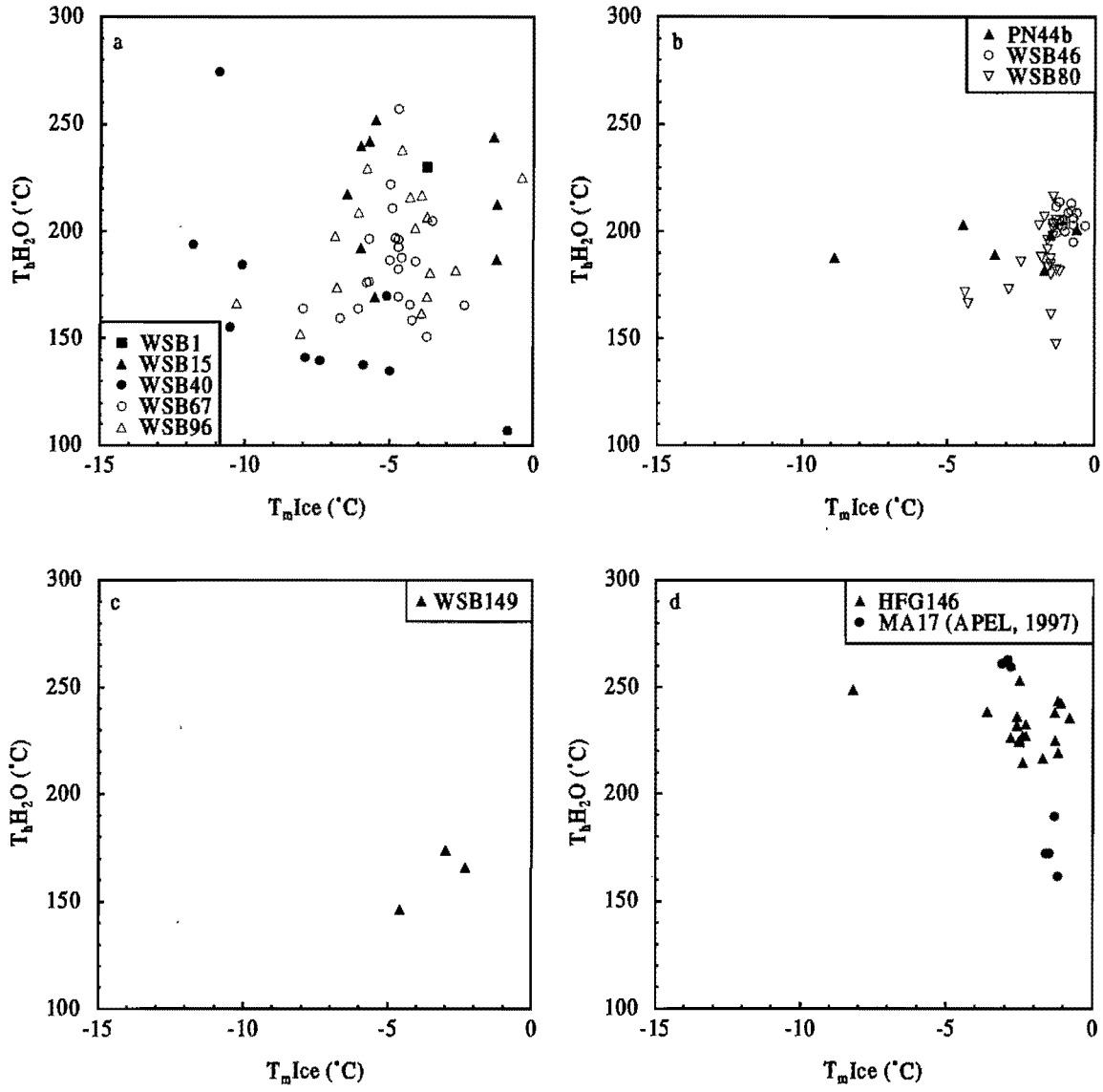

Figure 5.1 Summary of ice melting temperatures and total homogenisation temperatures for Type Ia inclusions from D_1/D_2 quartz veins: (a) northern area, (b) central area, (c) southern area, (d) Vanrhynsdorp area. Individual datum points correspond to averages of each individual trail.

and 210°C and -9.3°C and -0.1°C, respectively. The majority of the data range between 180°C and 210°C (T_hH_2O) and -7.2°C to -0.1°C ($T_m$ice). Lower T_hH_2O data tend to correspond to lower $T_m$ice data. The range in T_hH_2O and $T_m$ice for the northern area sample (WSB100) is essentially coincident with the ranges of these variables for the central area veins (WSB86, 139 and 144). The highest T_hH_2O data are recorded from the D_4 veins (Fig. 5.2b), although there is an overlap with the maximum T_hH_2O data from the northern area. The T_hH_2O data vary between 221°C and 287°C with no low T_hH_2O data recorded in these veins. A wide spread of $T_m$ice values (-12.3°C to -1.5°C) is evident in Fig. 5.2b. The

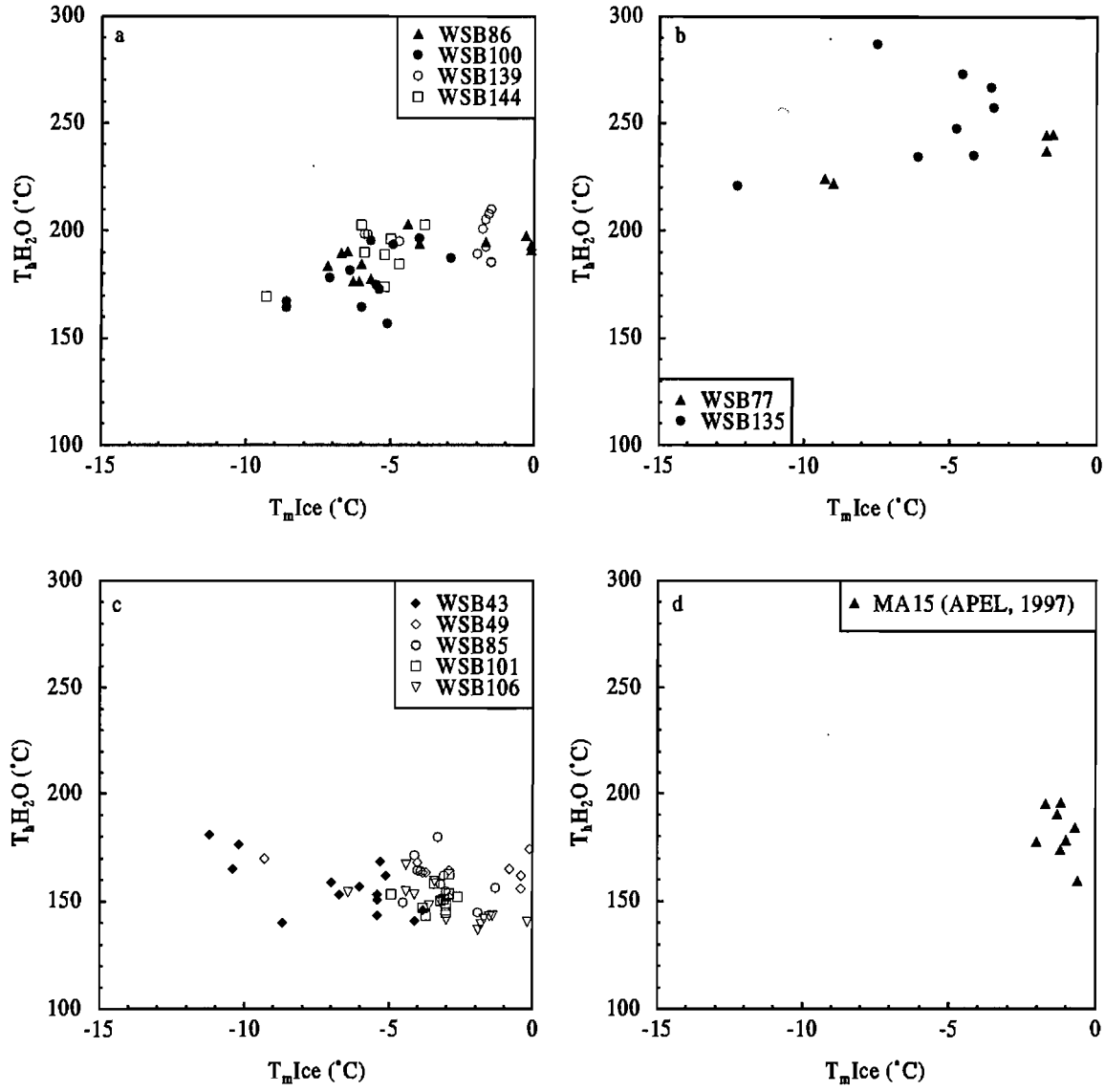

Figure 5.2 Summary bivariate plots of ice melting temperatures and total homogenisation temperatures for post-D_1/D_2 orogenic veins: (a) D_3 veins, (b) D_4 veins, (c) D_5 veins, (d) late stage veins (undifferentiated) from the Vanrhynsdorp area. Each datum point represents the average of a particular trail.

maximum T_hH_2O values from the vein furthest away from the pluton contact (WSB77) are lower than those from the sample taken closer to the edge of the pluton (WSB135). The D_5 veins show a narrow range of T_hH_2O data (137°C to 181°C) over a wide spread of $T_m$ice data (-11.2°C to -0.1°C)(Fig. 5.2c). The ranges in the ThH_2O and $T_m$ice data for the northern area D_5 veins (WSB43, 101 and 106) are essentially the same as those from the southern area D_5 veins (WSB49 and 85), but a cluster of lower $T_m$ice values from sample WSB43 (-11.2°C to -8.7°C) should be noted. No differentiation, in terms of vein generation, of the late stage veins from the Vanrhynsdorp area was made by Apel (1997),

hence the data are plotted separately here. A tight cluster of T_hH_2O (160°C to 196°C) and $T_m$ice values (-2.0°C to -0.6°C) is evident (Fig. 5.2d). A single, secondary trail of Type Ia inclusions (very rare) are present within the pre-orogenic sample from the Rosh Pinah mine (WSB24). Averages of the T_hH_2O and $T_m$ice data are 212°C and -2.7°C, respectively. These averages lie within the general range of orogenic data from the northern area. The T_hH_2O data from the Type Ia inclusions indicate a general trend of $D_4 \geq D_1/D_2$ northern $\geq D_1/D_2$ Vanrhynsdorp $> D_1/D_2$ central $\geq D_3 > D_1/D_2$ southern $\approx D_5$, whilst the $T_m$ice values are generally similar for the different areas and vein generations.

The Type Ib inclusions are petrographically identical to the Type Ia inclusions, yet yield final melting temperatures indicative of the formation of a clathrate at lower temperatures and hence the presence of some gas within the inclusion. Fig. 5.3a shows that most of the final melting temperatures of the clathrate ($T_m$clath), essentially regardless of vein generation, lie between 5.4°C and 10.7°C (mode = 8.4°C). The $T_m$clath values from the D_4 veins (9.2°C to 10.7°C) are, however, generally higher than those from the D_1/D_2 and D_5 veins. The ranges in $T_m$clath values from the four areas overlap.

The homogenisation temperature data of the Type Ib inclusions are summarised in Figs. 5.4a (all T_hH_2O data) and 5.4b (averages of trails). Two populations can be seen on the histogram in Fig. 5.4a: a higher temperature population between ~260°C and~295°C, and a lower temperature population between ~180°C and ~220°C. Considering the higher temperature population, it can be seen that the D_1/D_2 veins from the northern area together with the D_4 veins yield the highest T_hH_2O values. Lower values are observed in the sample from the Vanrhynsdorp area. Within the lower temperature population, no discrimination can be made between the D_1/D_2 veins from the northern, central and southern areas and the D_5 veins as their ranges overlap the total range of the population. The two populations are evident in Fig. 5.4b, and the data show a similar trend to that discussed above. The Type Ib T_hH_2O data indicate a general trend of $D_4 \approx D_1/D_2$ northern $> D_1/D_2$ Vanrhynsdorp $> D_1/D_2$ central $\approx D_1/D_2$ southern $\approx D_1/D_2$ northern (low T population) $\approx D_5$.

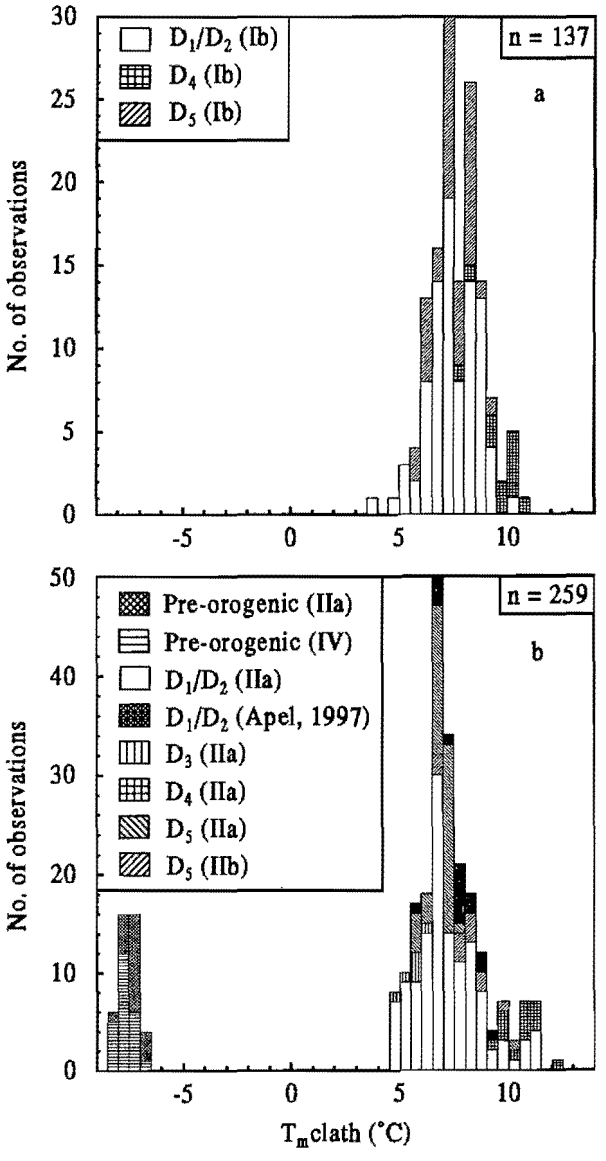

Figure 5.3 Frequency histograms of final melting temperatures of clathrates: (a) Type Ia inclusion from orogenic quartz veins, (b) Type IIa inclusions from both pre-orogenic and orogenic samples. Note that all the $T_m$clath data have been plotted, not the average values from separate trails.

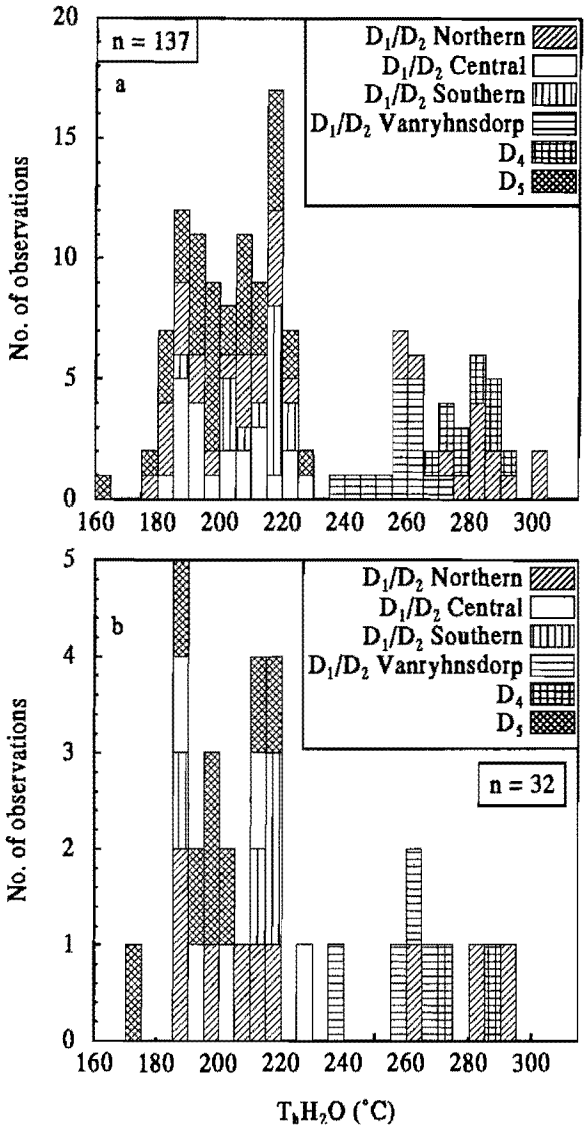

Figure 5.4 Frequency histograms of the total homogenisation temperature of Type Ib inclusions from orogenic quartz from the various areas: (a) all T_hH_2O data, (b) average T_hH_2O data from separate trails (i.e. each unit block represents a separate trail).

Type II inclusions

These inclusions were cooled through -110°C and definite freezing of the carbonic component (as recognised by distortion in the shape of the carbonic bubble together with the apparent disappearance of the second bubble) occurred between -100°C and -95°C. The phase changes observed during the heating of these inclusions were: the triple-point of CO_2, the first melting of ice (very rarely), the final melting of the gas hydrate and the homogenisation temperature of the CO_2. No total homogenisation temperature readings

were obtained due to the continual decrepitation of the Type II inclusions (over a wide range of temperatures) before total homogenisation.

The triple-point melting temperature of CO_2 (T_mCO_2; -56.6°C for pure CO_2), or the depression thereof, was readily observable by the sudden reformation of a "double bubble" consisting of carbonic liquid and vapour. Visible changes in the morphology of the bubble were recorded as T_e estimates, although $T_m$ice was not observed in these inclusions. The final melting of the gas hydrate was recognised by the "smoothing out" of the "jagged" edges of the carbonic bubble, and was usually accompanied by the "freeing" of both the carbonic bubble as a whole, and the carbonic vapour bubble. Homogenisation of the carbonic component is mostly to the liquid phase, although several trails from a D_5 vein (WSB106) in the northern area exhibit homogenisation to the vapour phase. Consequently the Type II inclusions in this study have been divided into Type IIa (those homogenising to the liquid phase) and Type IIb inclusions (those homogenising to the vapour phase). The few T_e values determined for the Type II inclusions vary between <-38°C and <-24°C, irrespective of generation and geographical position.

Two distinct clusters are evident in the Type IIa data from the northern area D_1/D_2 veins (Fig. 5.5a): a cluster corresponding to high T_hCO_2 (25.4°C to 29.6°C) and T_mCO_2 (-57.4°C to -56.6°C) values, and another corresponding to low T_hCO_2 (-0.3°C to 17.1°C) and T_mCO_2 (-59.4°C to -58.1°C) values. The D_1/D_2 data from the central area generally plot within a cluster similar to that of the high T_hCO_2 and T_mCO_2 values from the northern area (Fig. 5.5b). The T_hCO_2 data and T_mCO_2 data range from 22.5°C to 30.6°C and from -57.4°C to -56.6°C, respectively. Data obtained for the southern area D_1/D_2 vein exhibit a narrow range of T_hCO_2 values (23.8°C to 30.7°C)(Fig. 5.5c) as do those obtained for D_1/D_2 veins from the Vanrhynsdorp area (28.6°C to 29.7°C; T_mCO_2 = -56.7°C to -56.6°C)(Fig. 5.5d). These populations are similar to the high T_hCO_2 and T_mCO_2 clusters of the northern and central area data. The limited Type IIa inclusion data obtained from the D_3 veins (a single datum point at -58.1°C, 16.1°C) is shown in Fig. 5.6a. This corresponds to the low T_hCO_2 and T_mCO_2 cluster exhibited by the D_1/D_2 data. The D_4 veins show a grouping of T_hCO_2 (11.0°C to 15.6°C) and T_mCO_2 (-59.1°C to -58.9°C)(Fig. 5.6b) similar to the low T_hCO_2

and T_mCO_2 cluster of the D_1/D_2 veins. Two populations, seemingly characteristic of the Type IIa inclusions from the orogenic veins, are also present within the D_5 veins (Fig. 5.6c). The T_hCO_2 data range from 21.1°C to 27.9°C over a T_mCO_2 interval of -56.8°C to -56.6°C. A single datum point indicates the presence of a lower temperature cluster (-60.0°C, -6.1°C). The central, southern and Vanrhynsdorp D_1/D_2 vein data all plot within the high T_hCO_2 and T_mCO_2 cluster described, as do data from the D_5 veins in both the northern and central areas. Data from the D_4 and central area D_5 veins define a lower T_hCO_2 and T_mCO_2 cluster that is very similar to the lower temperature cluster developed within the northern area D_1/D_2 veins. A distinctly different cluster of Type IIa data is evident from the pre-orogenic footwall breccia sample from the Rosh Pinah mine (Fig. 5.6d). The T_mCO_2 data (-61.1°C to -60.4°C) are generally lower than those from the orogenic samples, whilst a narrow range of T_hCO_2 values (between 2.9°C and 5.3°C) further highlights the difference. Type IIb inclusions were only encountered in one sample (WSB106, D_5). The T_hCO_2 (19.3°C to 28.7°C) and T_mCO_2 (-58.2°C to -56.6°C) data from these inclusions, with the exception of the single datum point at (-58.2°C, 19.3°C), generally exhibit a high T_hCO_2 and T_mCO_2 cluster similar to that described for the Type IIa inclusions above (Fig. 5.6c).

The $T_m$clath values for the orogenic veins (regardless of geographical locality and vein generation) form a well-defined population ranging between 4.6°C and 12.1°C (mode = 6.8°C)(Fig. 5.3b). The D_4 vein $T_m$clath values generally lie on the high temperature side (9.5°C to 12.1°C) of the population similar to the $T_m$clath values from the D_4 Type Ib inclusions (see Fig. 5.3a). The $T_m$clath values of the Type IIa inclusions from the pre-orogenic silicic footwall breccia (WSB24) plot in a lower temperature, completely separate population ranging between -8.1°C and -6.8°C (mode = -7.7°C).

Type III inclusions

These inclusions were cooled as for the Type II inclusions, and the temperatures of the two phase changes observed (viz. the triple-point of CO_2 and the homogenisation,

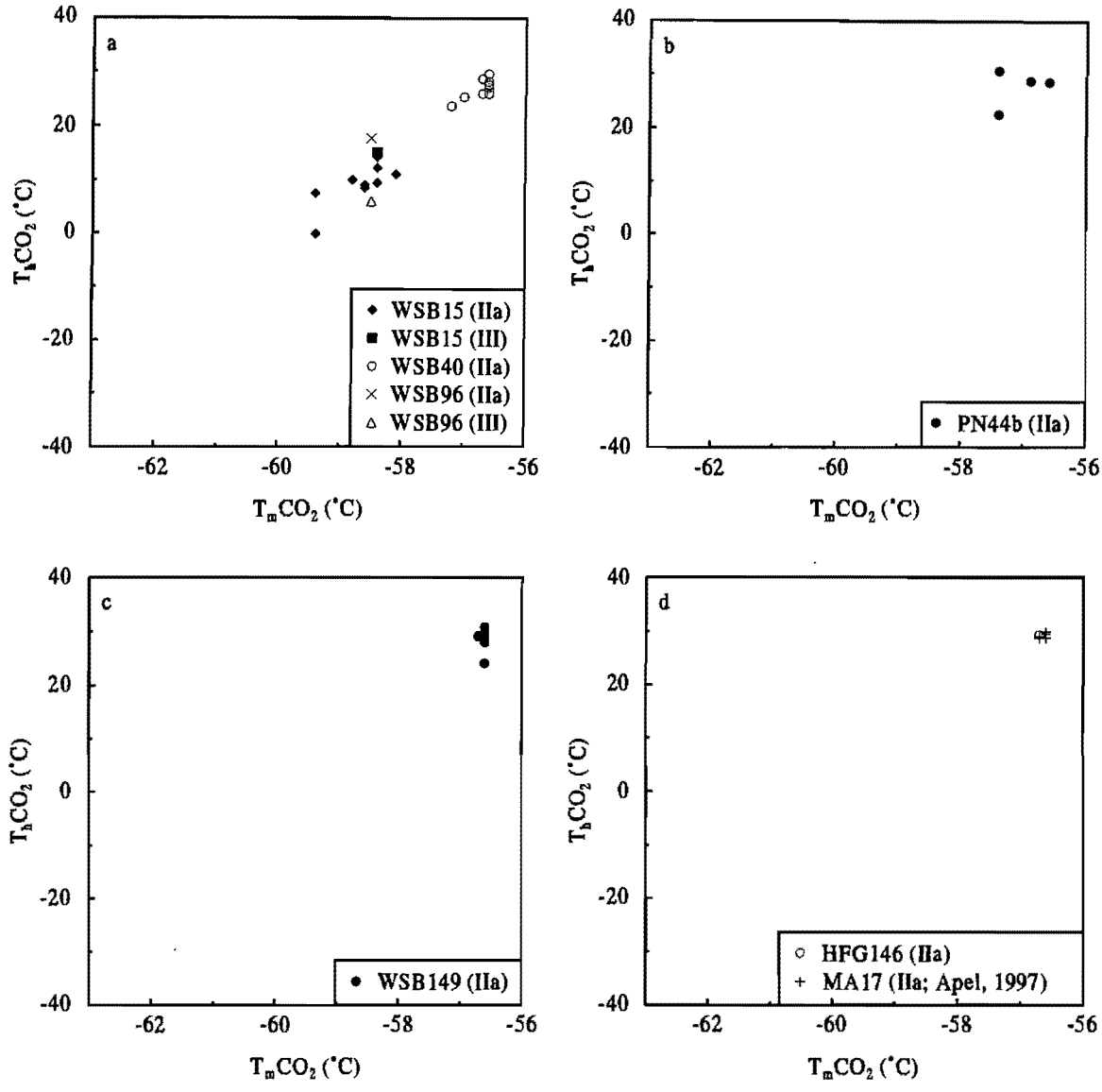

Figure 5.5 Summary bivariate plots of the triple-point depression (T_mCO_2) and the CO_2 homogenisation temperatures for Type II and Type III inclusions from post-D_1/D_2 quartz veins: (a) northern area, (b) central area, (c) southern area, (d) Vanrhynsdorp area.

always to the liquid phase, of the CO_2) were recorded. Type III inclusions from D_1/D_2 veins were only observed in the northern area. Their microthermometric data (T_hCO_2 = 5.9°C to15.0°C, T_mCO_2 = -58.9°C to -58.4°C) form a population that is similar to the low T_hCO_2 and T_mCO_2 cluster defined for the Type II inclusions (see Fig. 5.5a). The T_hCO_2 (-8.6°C to -7.7°C) and T_mCO_2 (-59.7°C to -59.4°C) data from the D_3 veins (Fig. 5.6a) show a similar grouping into a lower temperature cluster. Data from the D_4 veins (Fig. 5.6b)

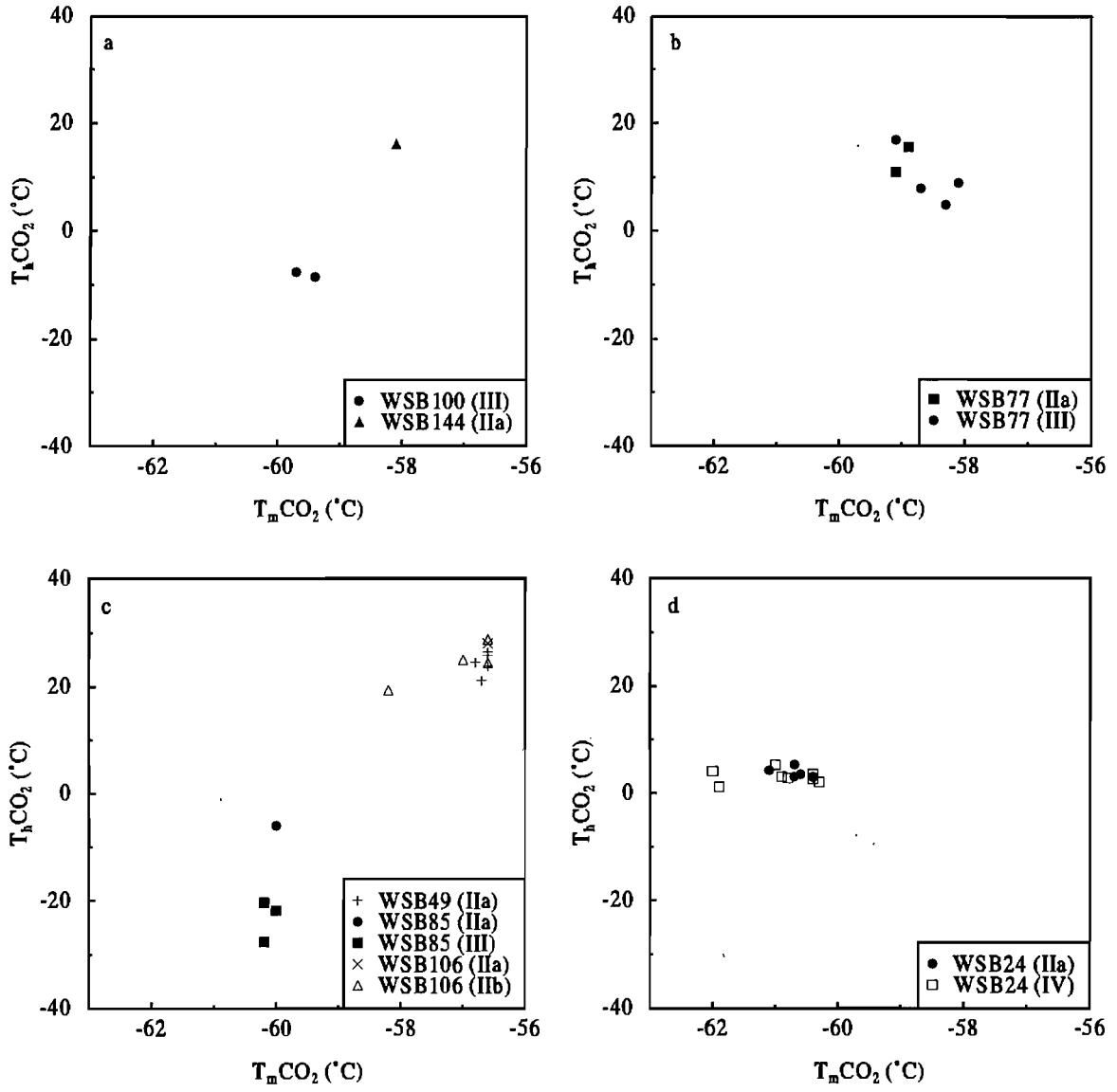

Figure 5.6 Summary bivariate plots of the triple-point depression (T_mCO_2) and the CO_2 homogenisation temperatures for Type II and Type III inclusions from post-D_1/D_2 quartz veins: (a) D_3, (b) D_4, (c) D_5, and pre-orogenic quartz: (d) silicic footwall breccia, Rosh Pinah mine.

essentially cluster within the low T_hCO_2 and T_mCO_2 population described for the Type IIa inclusions. The T_hCO_2 data for the D_4 veins range from 4.9°C to 16.9°C, whereas the T_mCO_2 data vary between -59.1°C and -58.1°C. The lowest T_hCO_2 (-27.7°C to -20.4°C) and T_mCO_2 (-60.2°C to -60.0°C) data were obtained for the D_5 veins (see Fig. 5.6c). The Type III inclusions from any given vein lie within the same T_hCO_2 and T_mCO_2 cluster as their Type II counterparts.

Type IV inclusions

These inclusions are, except for the presence of a daughter crystal, essentially the same as the Type II inclusions, and phase changes similar to those in the latter were observed. Although the temperatures of these phase changes were readily observable, the melting temperature of the daughter crystal was beyond the safe upper temperature limit of the instrument. Decrepitation precluded the measurement of the total homogenisation of the Type IV inclusions. The carbonic component always homogenised to the liquid phase. The T_hCO_2 (1.1°C to 5.3°C) and T_mCO_2 (-62.0°C to -60.3°C) data lie in the same cluster as those for the Type IIa inclusions from the same sample (WSB24, see Fig. 5.6d). No first melting of ice was evident and the clathrate melting temperatures fall into the same low $T_m$clath interval (-8.2°C to -6.8°C) as their Type IIa counterparts (Fig.5.3b). The daughter crystals were still present in the inclusions at 500°C.

Type V inclusions

The phase changes in these inclusions are essentially the same as those of the Type Ia inclusions, with the possibility of a fourth phase change: the melting of the daughter crystal. Total homogenisation of these inclusions was always to the liquid phase. The Te values from these inclusions vary between <-57°C and <-52°C, and a definite $T_m$ice value (-27.0°C) was only observed in one of the inclusions. Total homogenisation occurred between ~340°C and ~390°C, and the daughter crystal was still present within the inclusions at 500°C.

5.2 Stable Isotopes

5.2.1 Oxygen

The $\delta^{18}O$ values (relative to V-SMOW) were determined for 65 orogenic quartz veins, 4 orogenic calcite veins and 28 host-rocks. Values from five carbonate host-rocks, spatially

related to the carbonate-hosted quartz veins that were analysed, were obtained from P. Fölling (unpublished data).

The oxygen isotopes from the various generations (regardless of area) are plotted in Fig. 5.7a. The quartz vein D_1/D_2 data vary between 6.8‰ and 25.0‰, and the $\delta^{18}O$ values for the calcite veins of the same generation (11.7‰ to 23.3‰) also fall within this range (see Appendix 5). Data from the D_3 quartz veins range between 7.7‰ and 14.1‰, and the $\delta^{18}O$ values from the D_4 quartz veins range between 11.9‰ and 15.3‰. The single D_5 calcite vein yielded a value of 14.9‰ and this lies within the range of $\delta^{18}O$ values from quartz veins of the same generation (9.0‰ to 23.0‰). The ranges in $\delta^{18}O$ values from the D_3, D_4 and D_5 veins lie within the range of $\delta^{18}O$ values from the D_1/D_2 data. The variation in $\delta^{18}O$ is clearly not a function of vein generation or composition.

The range in D_1/D_2 $\delta^{18}O$ values (regardless of vein composition) from the Rosh Pinah mine (11.3‰ to 13.4‰), the northern area (8.7‰ to 23.3‰) and the southern area (11.7‰ to 16.1‰) fall into range of D_1/D_2 $\delta^{18}O$ values from the central area (6.8‰ to 25.0‰)(see Fig. 5.7b). A single $\delta^{18}O$ value from a D_3 vein in the northern area (12.8‰) lies within the range of $\delta^{18}O$ values for the central area D_3 veins (7.7‰ to 14.1‰)(Fig. 5.7c). The northern area D_5 $\delta^{18}O$ values (9.7‰ to 10.7‰) fall within the range of central area D_5 $\delta^{18}O$ data (9.0‰ to 23.0‰)(Fig. 5.7c). Variation in $\delta^{18}O$ is not a function of geographical position.

The variation in $\delta^{18}O$ as a function of host-rock, regardless of generation and vein composition, is shown in Fig. 5.7d. Note that veins hosted in granite, quartzite and metapelite rocks have been grouped together under "other host" due to the similarity in their $\delta^{18}O$ values for the same stratigraphic unit. Most of the veins are hosted by metapelites. Veins hosted within rocks other than carbonate, for any given formation, generally have lower $\delta^{18}O$ values than those hosted within carbonate rocks. The carbonate-hosted vein from the Rosh Pinah Formation has a higher $\delta^{18}O$ (14.4‰) value than the metapelite-hosted veins (12.1‰ to 13.4‰) from this formation. Regionally, veins from the

Pickelhaube Formation carbonates (17.5‰ to 25.0‰) are enriched in the heavier isotope relative to those hosted within non-carbonate rocks (6.8‰ to 17.3‰).

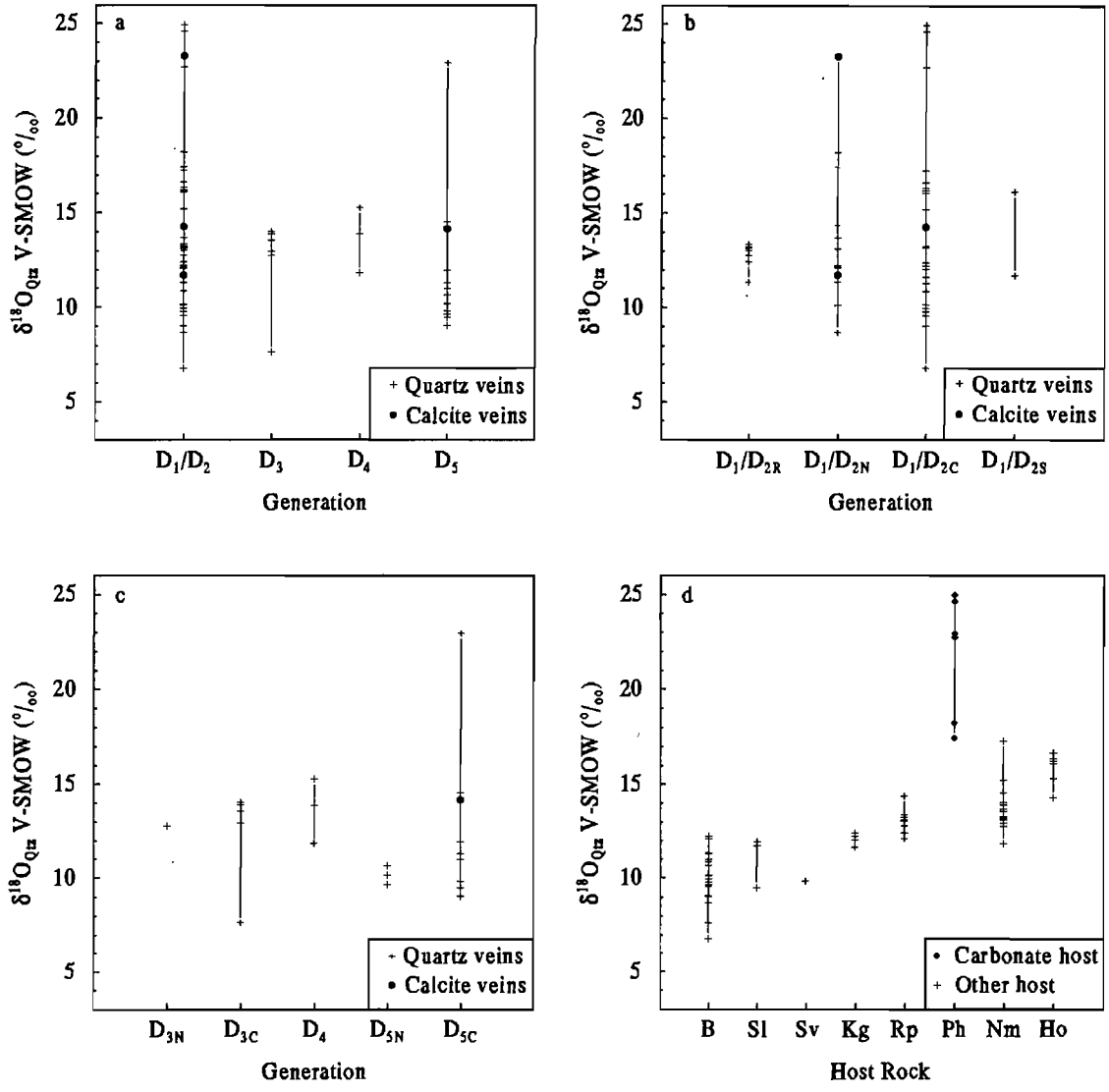

Figure 5.7 Ranges in $\delta^{18}O$ value (relative to V-SMOW) obtained from vein quartz and vein calcite for: (a) the various vein generations, (b) D_1/D_2 veins from different areas, (c) post-D_1/D_2 veins from different areas, (d) different host-rocks, in stratigraphic sequence. Note that R = Rosh Pinah mine, N = northern area, C = central area, S = southern area, B = basement, Sl = Lekkersing Fm, Sv = Vredefontein Fm, Kg = Kaigas Fm, Rp = Rosh Pinah Fm, Ph = Pickelhaube Fm, Nm = Numees Fm, Ho = Holgat Fm.

The veins hosted in rocks other than carbonate show a general trend towards higher $\delta^{18}O$ values as a function of stratigraphic position (Fig. 5.7d), although the ranges in $\delta^{18}O$ do overlap. Quartz veins hosted in basement granites and metapelites (6.8‰ to 12.2‰) exhibit the lowest recorded $\delta^{18}O$ values. The ranges in $\delta^{18}O$ from those veins hosted in the

Lekkersing Formation (9.5‰ to 12.0‰) and the Vredefontein Formation (9.9‰) fall within the $\delta^{18}O$ interval of the basement-hosted veins. The $\delta^{18}O$ values (11.7‰ to 12.4‰) from the veins hosted within the Kaigas Formation are within the upper end of the above range. The veins hosted by the Rosh Pinah Formation metapelites (12.1‰ to 13.4‰) show generally higher $\delta^{18}O$ values relative to the aforementioned units. Those quartz veins hosted by the Numees (including the basal Jakkalsberg Member) and Holgat Formations yielded ranges in $\delta^{18}O$ values of 11.9‰ to 17.3‰ and 14.2‰ to16.6‰, respectively.

The quartz vein $\delta^{18}O$ values and the $\delta^{18}O$ values of their host-rocks exhibit a linear relationship (see Fig. 5.8). Quartz veins have $\delta^{18}O$ values which are generally higher (by ~1.7‰) than those of their host-rocks. The subtle trend of an increase in $\delta^{18}O$ values corresponding to higher stratigraphic levels (described above) is also evident on this graph. Furthermore, the relationship between $\delta^{18}O_{host}$ and $\delta^{18}O_{vein}$ for each individual host-rock is similar to the overall linear relationship between these two variables for all the samples.

5.2.2 Hydrogen

The δD values of the fluid (from fluid inclusions) were determined for 4 quartz veins (Fig. 5.9). Note that the $\delta^{18}O$ values of the quartz vein are plotted, and that the $\delta^{18}O$ values of the fluid will be shifted further to the left on this diagram because of the quartz-water fractionation factor (see section 6.2).

There is a wide range in δD values (-35.0‰ to -75.6‰) for a small range in $\delta^{18}O$ vein quartz (10.2‰ to 13.0‰). The vein hosted within the Kaigas Formation (WSB46, D_1/D_2) yielded the lowest δD value (-75.6‰). Those veins hosted within the basement granite, WSB40 (D_1/D_2) and WSB101 (D_5), exhibit similar δD values (-53.9‰ and -46.3‰, respectively), and the highest δD value (-35.0‰) was obtained from the vein hosted within the Rosh Pinah metapelites, WSB2. Although there does not appear to be any variation in terms of vein generation in this limited dataset, it may be significant that all the veins from

the northern area plot within the so-called metamorphic fluid field, whereas the southern area vein plots outside this field.

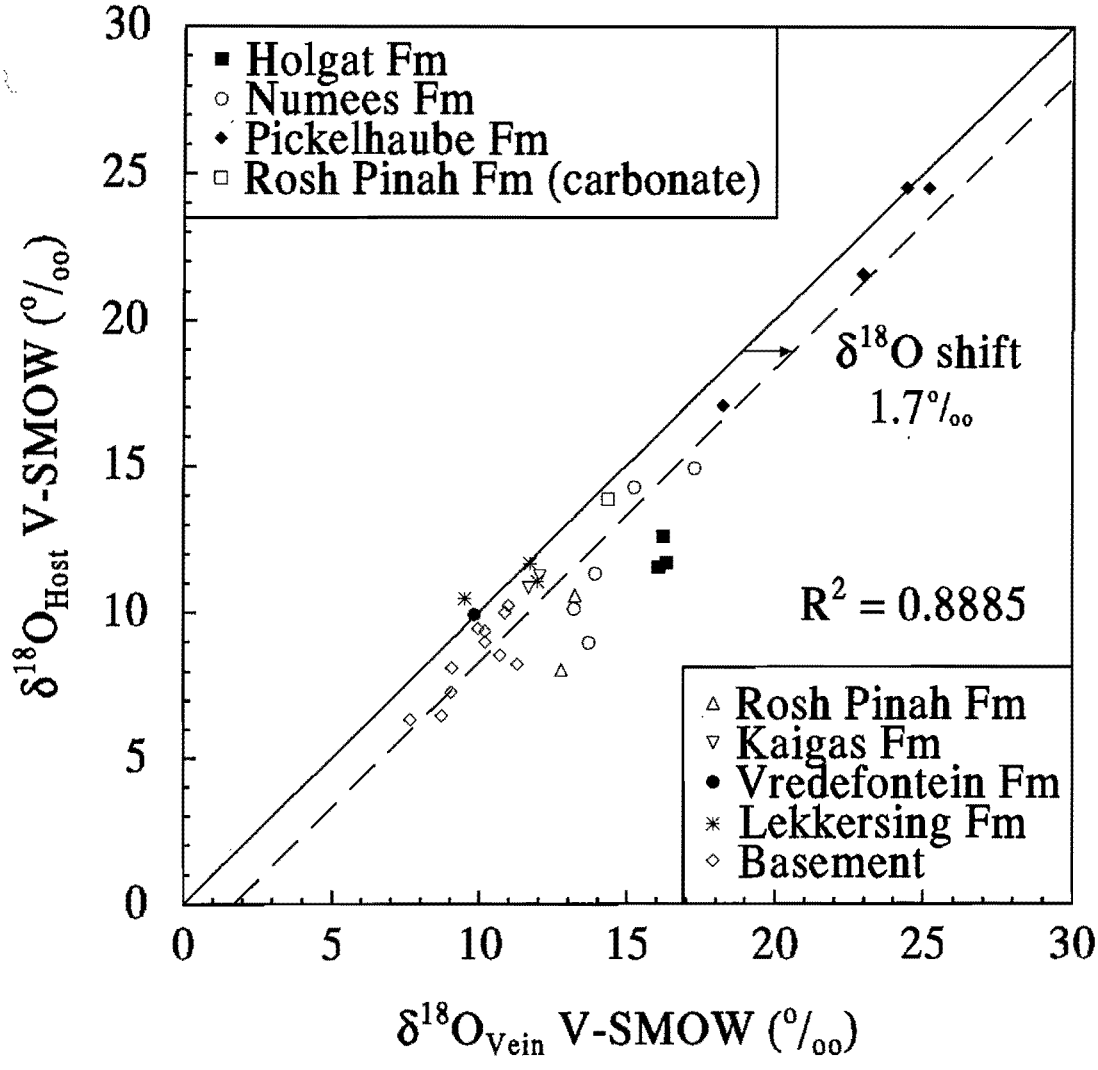

Figure 5.8 Bivariate plot of $\delta^{18}O_{vein}$ against $\delta^{18}O_{host\text{-}rock}$ for orogenic quartz veins, regardless of generation and geographical locality, hosted by different stratigraphic units.

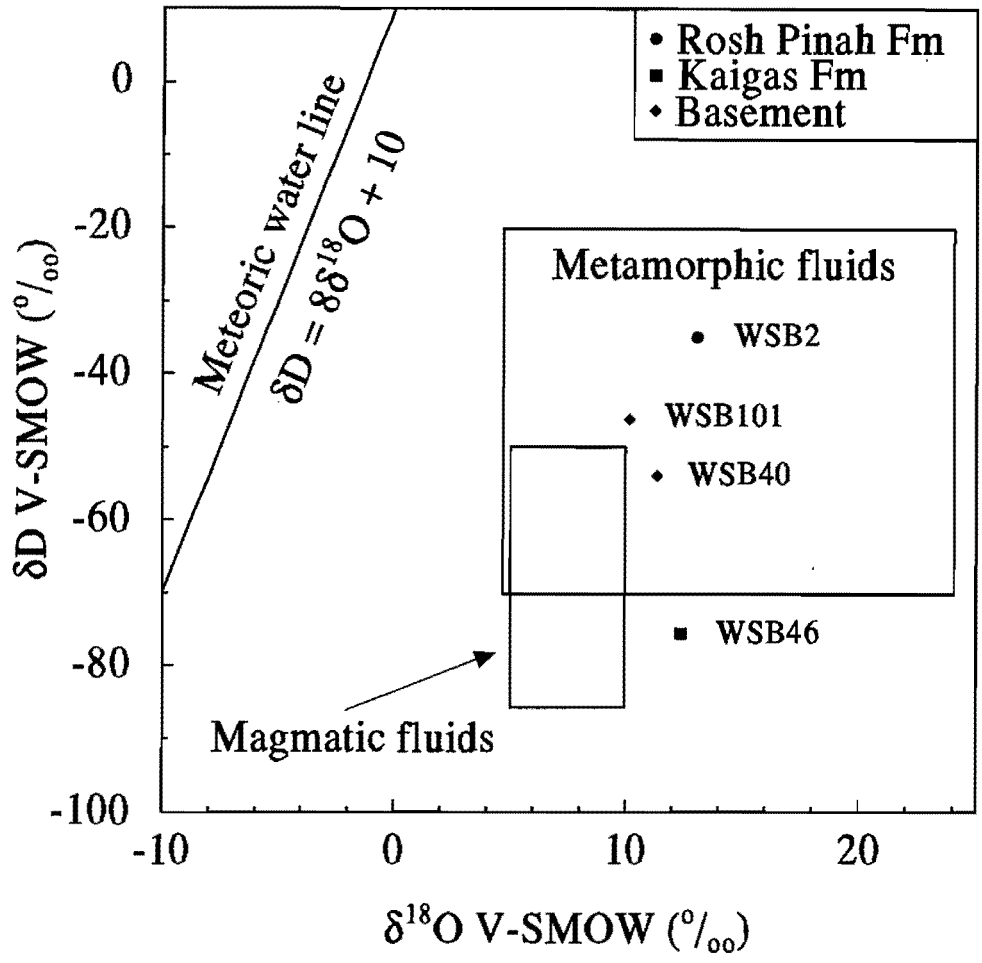

Figure 5.9 Plot of $\delta^{18}O_{vein\ quartz}$ vs δD_{fluid}. The fields of metamorphic fluids and magmatic fluids, together with the global meteoric water line ($\delta D = 8\delta^{18}O+10$, after Craig, 1961) are shown for reference purposes. It should be noted that whilst vein quartz $\delta^{18}O$ values have been plotted, the ranges in $\delta^{18}O$ for the aforementioned fields and the meteoric water line correspond to ranges in $\delta^{18}O$ of the fluid.

5.3 Crush-leach Analysis

Crush-leach analysis of dissolved ionic species in bulk fluid inclusion sets (using ion-chromatography; see section 4.3) was carried out on 11 samples. These samples are made up of 7 orogenic quartz veins, 1 orogenic calcite vein and a secondary, vein-hosted sphalerite from the Rosh Pinah mine, a sample of primary Rosh Pinah ore and a sample of the silicic footwall breccia at the mine. The primary ore consists predominantly of very fine-grained primary sphalerite, with associated chalcopyrite, galena, gangue carbonate and quartz, whereas the secondary sphalerites are very coarse-grained, and associated with vein

quartz. The results of these analyses are tabulated in Appendix 6, and plotted in Figs. 5.10a-d and 5.11a-d.

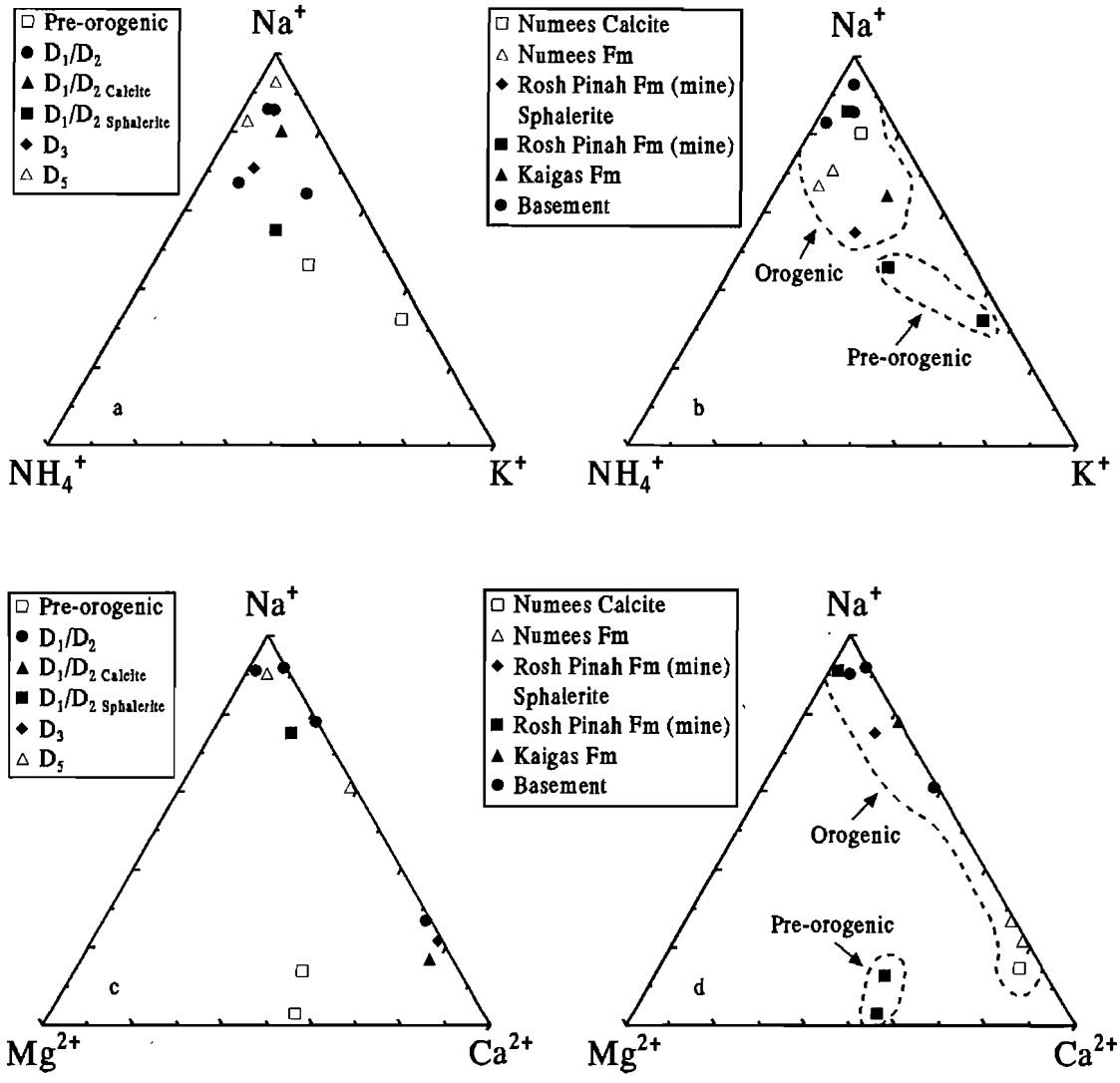

Figure 5.10 Ternary diagrams of the most abundant cations (molar values) present within fluid inclusion leachates for the various samples analysed: (a, b) Na^+-NH_4^+-K^+, (c, d) Na^+-Mg^{2+}-Ca^{2+}. Individual data points represent the average of the various sub-samples of each sample. Different vein generations, regardless of host-rock, are indicated in (a) and (c), whereas (b) and (d) show the different host-rocks for the various samples.

Variable amounts (unknown) of fluid inclusions within any given chip are a cause of variability in the concentrations of various sub-samples of any given sample, especially evident when each leachate is diluted in the same amount of water (in this case, 5 ml; see section 4.3). Bearing this in mind, it is evident that ratios are more important than absolute values.

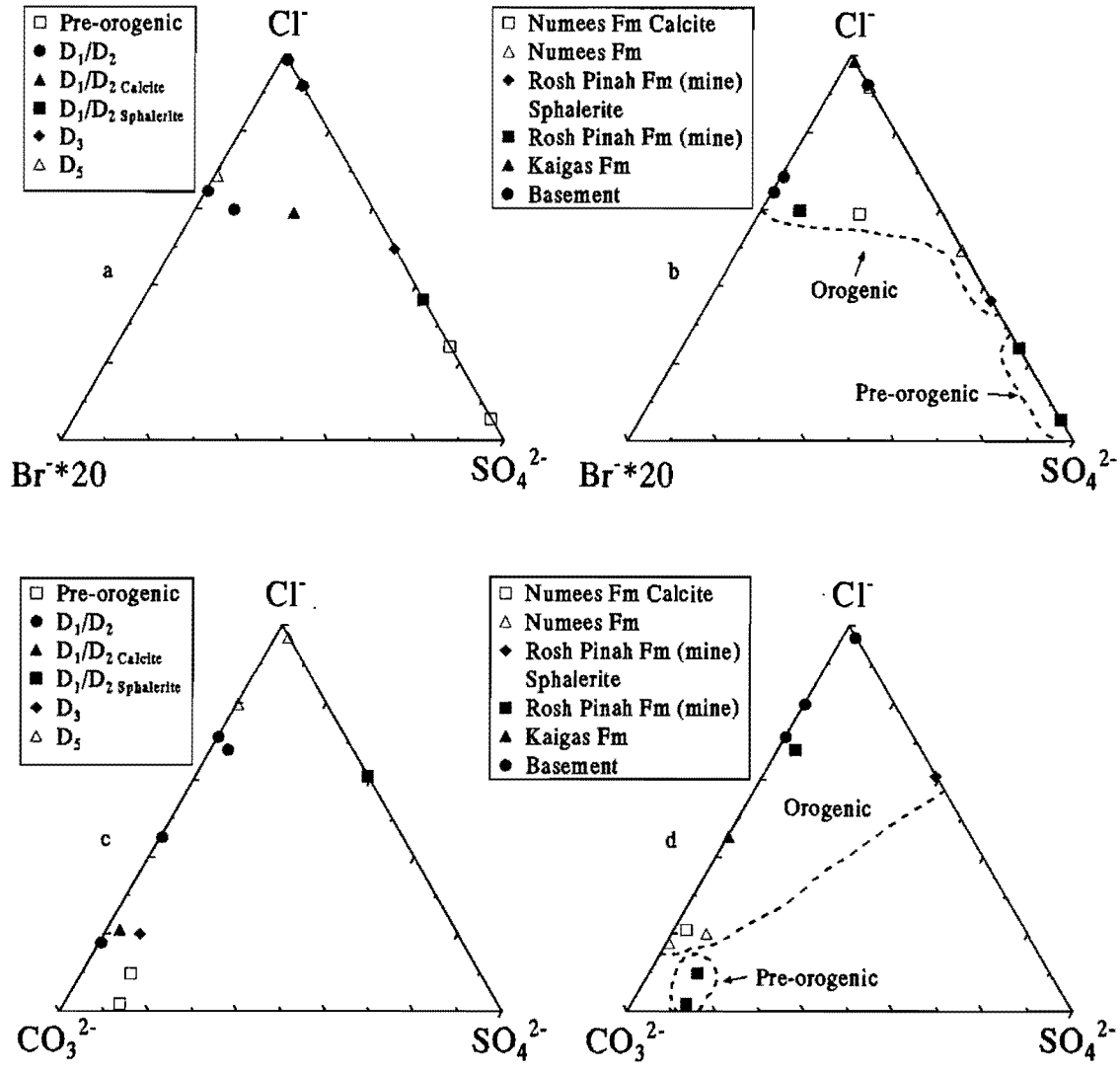

Figure 5.11 Ternary diagrams of the most abundant anions (molar values) present within fluid inclusion leachates for the various samples analysed: (a, b) Cl^--Br^--SO_4^{2-}, (c, d) Cl^--CO_3^{2-}-SO_4^{2-}. Individual data points represent the average of the various sub-samples of each sample. The variation of the important anions as a function of different vein generations (regardless of host-rock), and as a function of host-rock, are indicated in (a) and (c), and (b) and (d), respectively. Note that the CO_3^{2-} component has been estimated from charge balance calculations (see text for discussion).

Charge balancing of the crush-leach data, using the method described in Shepherd *et al.* (1985), indicates a general excess of cations over anions, although sample WSB5 shows a deficiency of cations with respect to anions (Table 5.1). The, in places, substantial shortfall on the anion side of the charge balance equations indicates that a fairly dominant anion was not analysed for. The spatial relationship between the primary samples from the mine and carbonate horizons, together with common presence of ankerite in orogenic quartz veins,

suggests the presence of, at least, the CO_3^{2-} anion. This anion was not determined during routine analysis due to the use of a $Na_2CO_3/NaHCO_3$ eluant. It should be noted that the term CO_3^{2-} in this study is an estimate of this anion at best because there may be other anions present (e.g. HCO_3^-).

Table 5.1 Cation charge, anion charge and charge balance data for each sample. Note that the cation and anion charge data are averages of the various sub-samples of each sample, and that they are expressed in atomic proportions.

Sample	Cation charge sample average (atomic proportions)	Anion charge Sample average (atomic proportions)	Charge balance (Cations/Anions)
WSB05	0.051	0.151	0.339
WSB15	0.108	0.065	1.655
WSB24	0.655	0.181	3.620
WSB31	0.960	0.075	12.747
WSB40	0.288	0.161	1.786
WSB43	0.202	0.134	1.501
WSB86	0.248	0.049	5.106
WSB96	0.155	0.016	9.608
WSB96C	0.840	0.127	6.599
WSB106	0.035	0.036	0.990
PN44b	0.110	0.033	3.366

Li^+ and Mn^{2+} are present only in amounts close to the detection limit. Primary samples from the Rosh Pinah mine are distinctly different, in terms of their cation ratios, to mine-hosted and regional orogenic samples (Fig. 5.10a-d). The pre-orogenic samples are enriched in terms of both K^+ and Mg^{2+} relative to both the mine-hosted and regional orogenic samples. The mine-hosted orogenic veins are similar to the regional orogenic veins in terms of Na^+, NH_4^+, Mg^{2+} and Ca^{2+}, and the orogenic veins, regardless of generation and host-rock, are very similar in terms of these ions. Orogenic samples from the Numees Formation (regardless of composition) are, however, more enriched in Ca^{2+} (Fig. 5.10d).

No F^-, NO_2^-, NO_3^{2-} and PO_4^{3-} were detected in the samples (Appendix 6). Only Cl^- and SO_4^{2-} were present in all samples, whilst Br^- was only found in 4 orogenic veins (WSB15, 40, 43 and 96C), all from the northern area. The difference between the pre-orogenic and orogenic samples, as highlighted by the cations, is also evident in terms of their anions

(Figs. 5.11a and b). The pre-orogenic veins are enriched in SO_4^{2-} relative to the orogenic veins. The orogenic veins from the mine are essentially similar to the regional orogenic veins in terms of the SO_4^{2-} ion, although the sample of secondary sphalerite was more enriched in this anion. The difference in fluid inclusion leachate chemistry between the pre-orogenic and orogenic samples is again apparent on the Cl^--CO_3^{2-}-SO_4^{2-} ternary diagrams (Figs. 5.11c and d), although not as pronounced as on the cation and Cl^--Br^--SO_4^{2-} plots. The pre-orogenic veins are generally depleted in Cl^- relative to the orogenic samples, although those samples from the Numees Formation (irrespective of vein composition and generation) are similarily depleted. Note that a value of 0 ppm for the CO_3^{2-} component was assumed for those samples for which the charge balance showed a cation excess.

5.4 SEM-Cathodoluminescence

A total of 6 samples, showing the contact between the vein quartz and the host-rock, were analysed using this technique in order to ascertain the extent (if any) of host-rock quartz within the vein quartz. Images representative of the dataset are presented in Fig. 5.12. The boundary between the host-rock and the vein can be seen as a sharp contact on both the back-scatter electron (Fig. 5.12a) and the cathodoluminescence images (Fig. 5.12b). The CL signature of the vein quartz is fairly uniform, showing no evidence of contamination by host-rock quartz.

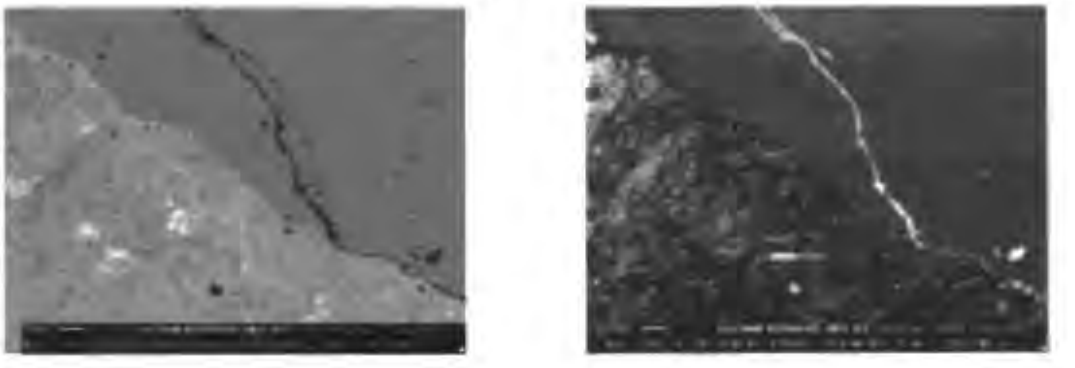

(a) (b)

Figure 5.12 SEM (a) back-scatter electron and (b) cathodoluminescence images for the basement (Vioolsdrif Suite) granite/quartz vein contact (sample WSB101).

5.5 Raman Spectroscopy

Preliminary Raman Spectroscopy data were obtained from one orogenic sample (WSB15) for which a significant depression in the $TmCO_2$ was determined by the fluid inclusion studies (see section 5.1). Two Type IIa inclusions were analysed and the results are presented in Table 5.3. The triple-point of CO_2 in this sample has been depressed by the presence of methane. No other gases were found to be present.

Table 5.2 Summary of Raman Spectroscopy data for sample WSB15.

Inclusion #	$TmCO_2$ (°C)	Component	Proportion (%)
1	-58.1	CO_2	89
1	-58.1	CH_4	11
2	-57.9	CO_2	89
2	-57.9	CH_4	11

6. DATA INTERPRETATION AND DISCUSSION

6.1 Fluid Inclusions

Two distinct populations of fluid inclusions can be distinguished based on their composition and host-rock associations: those related to the pre-orogenic Rosh Pinah ore-forming fluid, and those associated with the orogenic fluids.

6.1.1 Pre-orogenic Inclusions: Rosh Pinah Ore-forming Fluid

Petrographically, the Type II, IV and V inclusions hosted within the pre-orogenic silicic footwall breccia appear to satisfy the criteria (after Roedder, 1984) for a pseudo-secondary origin (section 5.1). If these inclusions are truly pseudo-secondary and the isolated inclusions primary, then the fluid in such inclusions is most likely a sample of the ore-forming fluid as the footwall breccia is syngenetic in terms of the formation of the ore deposit (Siegfried, 1990). The similarity, in terms of ionic composition, between the inclusion fluids of the silicic footwall breccia to those of the primary carbonate ore, as well as their significant compositional differences when compared to the orogenic fluids (sections 5.1, 5.3, 6.1.2) supports this contention.

The complex ionic composition of the ore-forming fluid (see section 5.3), especially the dominance of Ca^{2+} and Mg^{2+} (in approximately equal proportions) over Na^{+}, precludes the use of an H_2O-NaCl model system for the interpretation of the microthermometric results obtained from these inclusions. The presence of daughter crystals together with the low $T_m$clath values (Fig. 5.3b) from the Type II and Type IV inclusions suggest that the ore-forming fluids were fairly saline. The fact that the daughter crystal is transparent, not cubic in shape and does not appear isotropic under cross-polarised light indicates that it is not halite. Furthermore, as it does not show any signs of melting below 500°C, chlorides of K, Ca and Mg are precluded (e.g. Roedder, 1984; Dubois and Marignac, 1997), and carbonates are suggested (Shepherd *et al.*, 1985). Calculating atomic ratios (e.g. Shepherd *et al.*, 1985) for various ions determined in the

leachate derived from crushing the two mine-hosted pre-orogenic samples, a possible fluid chemistry of: $CaMg(CO_3)_2$, NaCl and various sulphates, carbonates and chlorides of Na, K, Ca, Mg (in minor quantities) and possibly base metals is suggested for the ore-forming fluid (section 5.3; Appendix 6; Table 6.1).

Table 6.1 Atomic ratios of various ions determined in the leachate derived by crushing samples of the silicic footwall breccia (WSB24) and primary carbonate ore (WSB31) from the Rosh Pinah mine. See text for further discussion.

Sample	Na^+/Cl^-	Mg^{2+}/CO_3^{2-}	Ca^{2+}/CO_3^{2-}	Mg^{2+}/Ca^{2+}
WSB24	0.98	0.60	0.52	1.15
WSB31	3.33	0.58	0.46	1.28

It must be noted that only CO_3^{2-} has been considered as the "missing" anion (as shown by the cation excess in the charge balance) due to the fact that a $Na_2CO_3/NaHCO_3$ eluant was used for the anion runs (see section 4.3). Consequently there may be other undetermined anions that are not explained by this assumption and hence other compounds in solution. As samples WSB24 and WSB31 are bulk rock samples and not individual veins, two possible sources (in terms of liberation during crushing) for the Ca^{2+} and Mg^{2+} ions present within the leachate exist. They may have been released either from the fluid inclusions, or by the partial dissolution of the host-rock dolomite. Chetty (1998) showed that the release of Ca^{2+} and Mg^{2+} into the leachate by the partial dissolution of the host carbonate (either calcite or dolomite) during crushing under room temperature conditions is negligible. She accomplished this by showing that there was no systematic variation in the charge balance calculated for leachates derived from either calcitic or dolomitic host-rocks, even though there is an order of magnitude difference in terms of their solubilities at 25°C (Krauskopf and Bird, 1995).

Observed Ca^{2+}/CO_3^{2-} and Mg^{2+}/CO_3^{2-} ratios of ~0.5 and ~0.6, respectively, suggest that these components occur in dolomitic proportions, with an excess of Mg^{2+} relative to Ca^{2+}. As Ca^{2+}, Mg^{2+} and CO_3^{2-} are (relatively) the most abundant ions present within the pre-orogenic fluid inclusions, and as the host-rock is essentially dolomitic, the daughter crystals are most likely dolomite. This is supported by the high relief exhibited by these crystals and the fact that they show no visible signs of melting below 500°C (e.g.

Hartman *et al.*, 1996). The petrographic distribution of the daughter crystals (i.e. their presence within some, but not all inclusions within the same grouping) indicates that the pre-orogenic ore-forming fluid was saturated (and in places supersaturated) with respect to dolomite. The fact that the fluid from the Type II and Type IV inclusions in WSB24 is essentially the same (as evidenced by microthermometric results) even though no daughter crystals are developed within the former, supports this argument. The presence of daughter crystals of dolomite is consistent with a fairly saline fluid as the solubility of CO_2 (and hence that of dolomite) is particularly low in such saline solutions (Roedder, 1984).

The suppression of the melting point of pure CO_2 (-56.6°C) can be ascribed to the presence of other constituents (e.g. CH_4 and N_2) within the inclusion (Roedder, 1984). The pre-orogenic ore-forming fluid inclusions plot over a range of T_mCO_2 values (-62.8°C to -59.4°C) that is indicative of the presence of other gaseous constituents, at fairly constant T_hCO_2 values (0.4°C to 6.0°C)(Fig. 6.1). Considering the linear trend

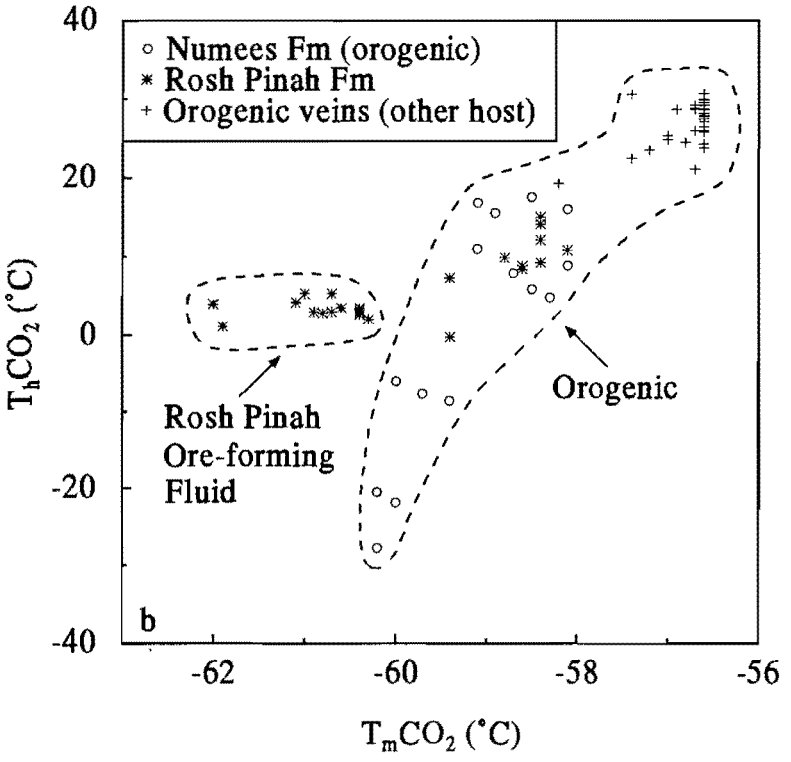

Figure 6.1 Depression of the triple-point of CO_2 versus homogenisation temperatures for Type II, III and IV inclusions (see Figs 5.5a-d and 5.6a-d) from the pre-orogenic mine-hosted samples and various orogenic quartz veins.

developed within the orogenic carbonic inclusion data as a CO_2-CH_4 mixing line (see section 6.1.2; Fig. 6.1), it becomes apparent that other constituents, in addition to CH_4, are present within the ore-forming fluids. As the Rosh Pinah ore deposit is a massive sulphide deposit, the presence of H_2S can be expected.

The relative abundance and petrographic occurrence of the Type V inclusions suggests that they represent a carbonic-bearing end-member that was formed due to immiscibility between CO_2 (and other gases) and H_2O prior to inclusion entrapment. Alternatively, they may have been formed by the necking down of inclusions after the unmixing of CO_2 (and various gases) and the H_2O. Consequently, they are ignored in this discussion.

The association of the Skorpion and Rosh Pinah base metal deposits with felsic (and minor mafic) volcanism (e.g. Frimmel *et al.*, 1996b), suggests that their base metal content was derived directly from the magma, with the former deposit representing mineralisation proximal to the volcanic activity (e.g. Erongo Exploration and Mining Company Ltd and Reunion Mining PLC, 1996), and the latter representing more distal mineralisation. The rift-related magmatism would have induced a hydrothermal circulation system in which hot, chemically evolved hypersaline brines were most probably responsible for the transport of base metals and their subsequent, more distal, expulsion onto the sea floor (e.g. McKibben and Hardie, 1997). The silicic footwall breccia is most probably a manifestation of the passage of these brines through the sea floor (e.g. Siegfried and Moore, 1990). The K component of the Rosh Pinah ore-forming fluid supports the contention of a direct input into the hydrothermal system by the felsic magmatism.

6.1.2 Orogenic Inclusions

Goldstein and Reynolds (1994) indicate that T_e values between -40°C to -30°C are difficult to interpret. Although the majority of the first melting temperatures observed occur within this interval, it must be remembered that these temperatures are maximum temperature estimates of the T_e and that the true T_e is probably lower. The presence of T_e

values lower than -40°C indicate that Ca^{2+} and/or Mg^{2+} are present in addition to the Na^{+} (Davis *et al.*, 1990), but the difficulty in determining the T_e with a high degree of confidence complicates the choice of model system. The crush-leach data confirm the presence of Na^{+} and indicate that Ca^{2+} is the dominant divalent cation present in inclusions from the majority of the samples. This suggests the use of the NaCl-$CaCl_2$-H_2O model system for the interpretation of the microthermometric results obtained from the orogenic vein-hosted inclusions. The absence (related to optical limitations given the generally small sizes of the inclusions) of intermediate melting phenomena prior to final melting precludes the use of this model system in the determination of salinity (see Oakes *et al.*, 1990). As the cotectic surfaces where ice melts for various systems show relatively small variations (see Crawford, 1981 and Oakes *et al.*, 1990), especially the NaCl, NaCl + $CaCl_2$ and $CaCl_2$ curves which essentially lie on top of one another (~2 wt% maximum deviation), an H_2O-NaCl model system is considered a reasonable simplification.

Salinity estimates for aqueous inclusions (Type Ia) are provided by the $T_m$ice values (see Chapter 5) because the degree of depression of the highest temperatures at which ice can exist is directly dependant on the salinity of the fluid (Roedder, 1984). The salinities of carbonic-bearing inclusion fluids (Types Ib and II) can be estimated by using their $T_m$clath values (Collins, 1979; Roedder, 1984). The Type Ib inclusions are regarded as carbonic-bearing inclusions due to the presence of a clathrate melting temperature and their petrographic association with Type II inclusions. Salinity estimates of aqueous inclusions have been calculated using the equation of Bodnar (1993). The equation of Chen (1972) has been used to calculate the salinities of the carbonic inclusions as it provides a better fit for the experimental data over the full range of $T_m$clath values (-10.0°C to 10.0°C) than the equation of Bozzo *et al.* (1973)(Darling, 1991). Calculated salinity estimates of inclusion fluids from the different types of inclusions hosted within the various vein generations from the different areas are summarised in Appendix 7. Note that the salinities are expressed in terms of the equivalent amount of NaCl required to obtain the observed freezing point depression or clathrate melting temperature (for the reasons discussed above) and are hereafter referred to as wt% $NaCl_{eq}$.

In order to unravel the evolution of the orogenic fluids, the nature of the fluids related to each deformation event must be characterised. As the orogenic fluids appear to be dominantly aqueous, with similar ranges in $T_m$ice data (and hence salinity data) for the fluid inclusions from the various vein generations (section 5.1), the fluids related to the different generations are best distinguished by using the T_hH_2O data of the Type Ia inclusions. The ranges in T_hH_2O data for the orogenic vein-hosted Type Ia inclusions are summarised in section 5.1 and are plotted against salinity on Figs 6.2a-d and 6.3a-d. Due to the multiple stages of deformation related to the Gariepian orogeny, it can be expected that the earliest formed veins (D_1/D_2) will contain inclusions related to the later events. Consequently the fluid inclusion data related to each orogenic event need to be characterised, starting with the latest event (D_5), and working back to the earliest event (D_1/D_2).

The T_hH_2O data for inclusions related to the D_5 event occur between 140°C and 180°C (Fig.6.2a), with salinities generally <10 wt% $NaCl_{eq}$ (although there are a few values between 10 and 15 wt% $NaCl_{eq}$), and show no variation in terms of host-rock or geographical position. Consequently data from earlier veins occurring within this range are ascribed to the D_5 event in this study. Inclusions within the late stage quartz vein from the Vanrhynsdorp area (MA17) exhibit T_hH_2O values between 160°C to 200°C, and salinities of <5 wt% $NaCl_{eq}$ (Fig. 6.2b). The T_hH_2O range overlaps with that obtained for inclusions from both the D_3 (see below) and D_5 veins from the central and northern areas. This may mean that either the late stage vein in the Vanrhynsdorp area is a D_3 vein with a D_5 component (in the sense of the outer margin of the southern Gariep Belt), or that there were only two deformation events in the Vanrhynsdorp area. Due to the lack of further information regarding the subdivision of the late stage veins in the Vanrhynsdorp area, the range of T_hH_2O data for the inclusions hosted within these veins is considered (in this study) to represent one generation.

No inclusions ascribable to the D_5 event were found within the D_4 veins (Fig. 6.2c), although such inclusions are present within the D_3 veins (Fig. 6.2d). The T_hH_2O values of inclusions ascribed to the D_4 event generally range between ~220°C and ~290°C.

Inclusions from the vein sampled closest to the Kuboos pluton (WSB135) yield, on average, higher T_hH_2O values (~253°C) than those from the vein taken from the outer margin of the aureole (WSB77; ~235°C). This is in agreement with a decrease in temperature away from the pluton. Salinities are generally <10 wt% $NaCl_{eq}$, although there are a few values between 10 and ~16 wt% $NaCl_{eq}$. The localised D_4 event is not represented in the inclusions from the D_3 and D_1/D_2 veins as no samples of these vein generations were taken from the aureole of the Kuboos pluton.

Ascribing a D_5 origin to inclusions within the D_3 dataset that exhibit T_hH_2O values between ~140°C and ~180°C, yields a T_hH_2O range of 180°C to 200°C for the D_3 event (Fig. 6.2d). Salinities of the D_3 fluid inclusions are generally <10 wt% $NaCl_{eq}$, with a few values between 10 and 15wt% $NaCl_{eq}$. Note that whilst there are T_hH_2O values higher than the upper limit defined for inclusions related to this event (e.g. WSB139), the inclusion data for this sample show two trends: a trend towards higher T_hH_2O values and a trend towards higher salinity values (Fig 6.2d). These trends indicate both stretching and leakage (with refilling), respectively, of the inclusions after entrapment due to thermal equilibration (see Fig.11.42 in Goldstein and Reynolds, 1994), and according to these authors, the intersection of the two trends represents the initial conditions. Consequently the initial conditions of entrapment for the fluid inclusions from WSB139 can be represented by a salinity of ~3 wt% $NaCl_{eq}$ and a T_hH_2O of ~190°C. These conditions clearly plot within the general range defined for inclusions related to the D_3 event. No variation as a function of area or host-rock can be seen in the T_hH_2O values from the D_3 vein-hosted inclusions. Consequently inclusions within the D_1/D_2 dataset that exhibit characteristics similar to those described for the D_3 and D_5 inclusions can be ascribed to these later events, regardless of area. As the Vanrhynsdorp area is considered separately, those inclusions within the D_1/D_2 dataset (for this area) that exhibit T_hH_2O data that plot within the range defined for the late stage vein-hosted inclusions, are ascribed to the D_{late} event.

Ascribing inclusions of the D_1/D_2 dataset from the northern area (Fig. 6.3a) and the central area (Fig. 6.3b) to the D_3 and D_5 events, yields T_hH_2O ranges of 200°C to 275°C

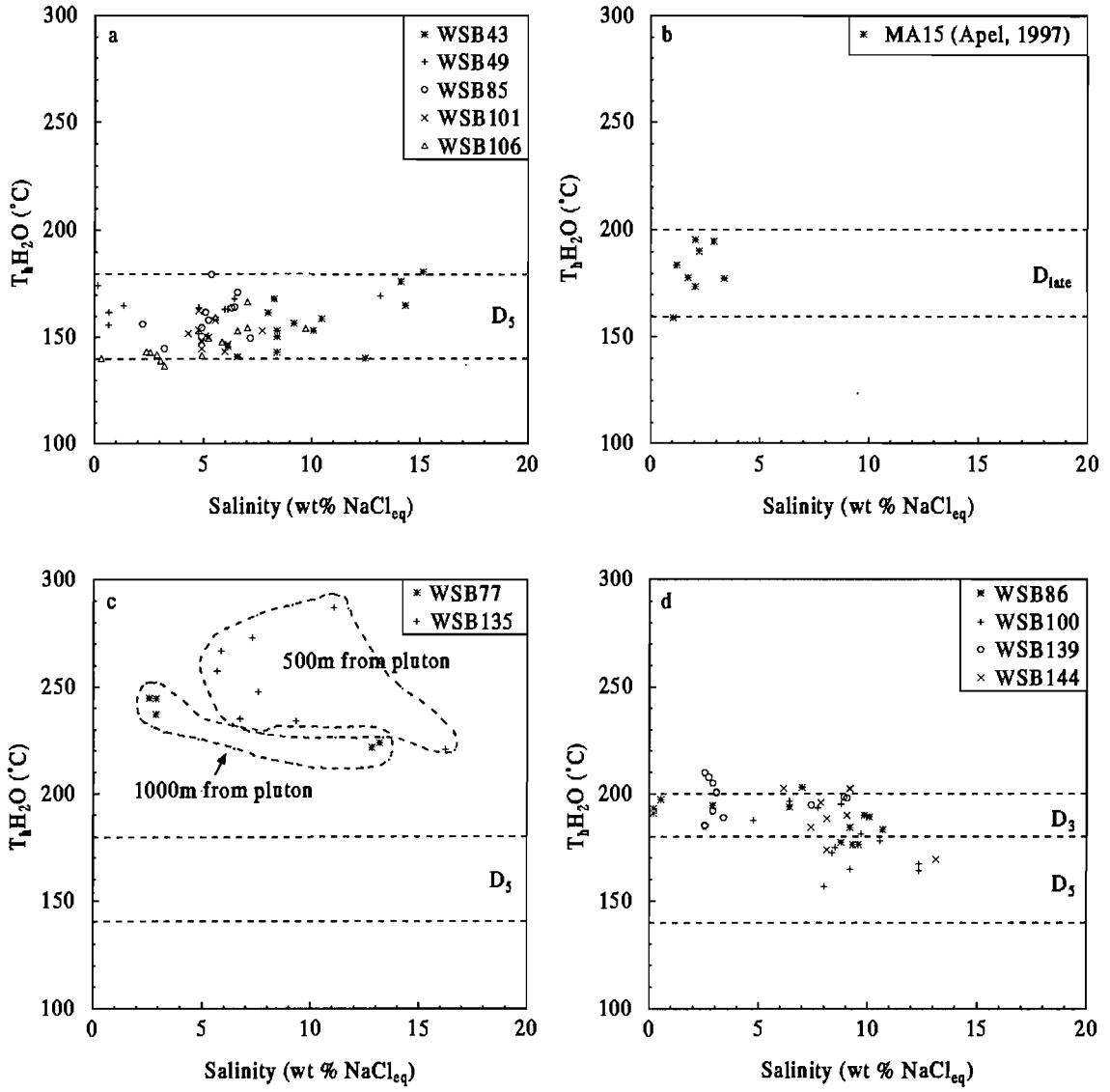

Figure 6.2 Total homogenisation temperatures versus salinity estimates for Type Ia inclusions from various generations of post-D_1/D_2 quartz veins: (a) D_5 veins, (b) D_{late} veins from the Vanrhynsdorp area, (c) D_4 veins, (d) D_3 veins. The ranges in T_hH_2O ascribed to the various orogenic events are shown bordered by stippled lines. See text for discussion.

and 200°C to 220°C, respectively. Salinities are predominantly <10 wt% $NaCl_{eq}$, although the averages of several trails yield salinities in the 10-16 wt% $NaCl_{eq}$ interval (e.g. WSB40 and WSB96). Ascribing a D_{late} origin to those inclusions from the Vanrhynsdorp area D_1/D_2 dataset (Fig. 6.3d) exhibiting T_hH_2O data plotting within the range defined for the D_{late} event, yields a T_hH_2O range from 210°C to 260°C, similar to that of the northern area D_1/D_2 vein-hosted inclusions. Salinities are <10 wt% $NaCl_{eq}$.

The D_1/D_2 inclusion data from the southern area (145°C to 175°C, salinities <8 wt% $NaCl_{eq}$; Fig. 6.3c) all

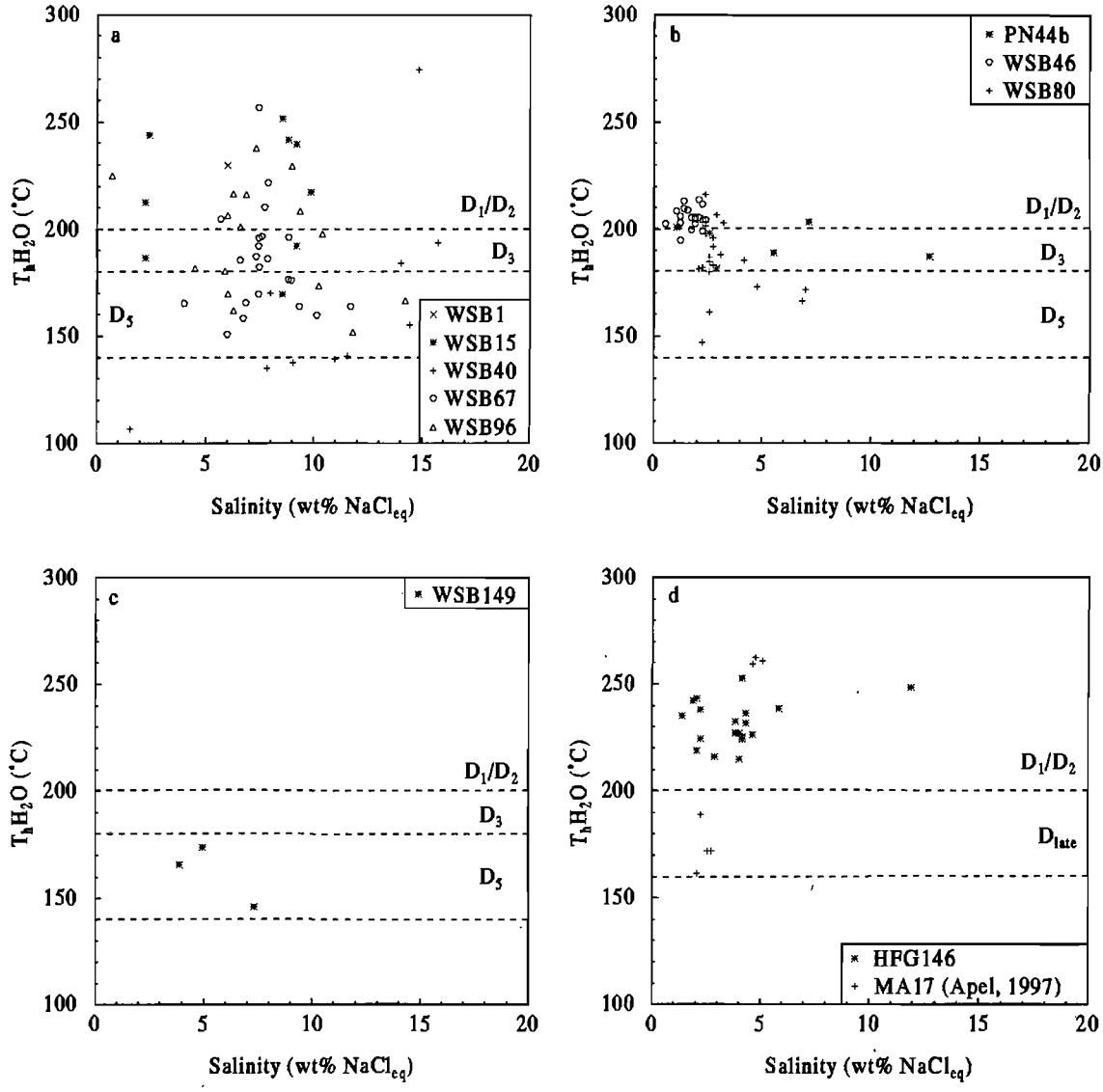

Figure 6.3 Total homogenisation temperatures versus salinity estimates for Type Ia inclusions from various D_1/D_2 quartz veins from the different areas: (a) northern area, (b) central area, (c) southern area, (d) Vanrhynsdorp area. The ranges in T_hH_2O ascribed to the various orogenic events are shown bordered by stippled lines. See text for discussion.

plot within the range of T_hH_2O data characteristic of inclusions ascribed to the D_5 event.This could mean that the D_1/D_2-related fluids in the southern area are of a lower temperature than those related to the same event elsewhere in the belt. It is most likely, however, that these data are from secondary inclusions that are related to the D_5 event. The variation in the T_hH_2O of the D_1/D_2 vein-hosted inclusions as a function of area is in

accordance with the findings of Frimmel (1995). Consequently the orogenic fluids from the northern and Vanrhynsdorp areas were hotter than the fluids from the central area.

The within-trail consistency of the T_hH_2O data for the majority of the Type Ia inclusions indicates that the post-trapping effects of thermal re-equilibration and necking-down after a phase change were minimal (Goldstein and Reynolds, 1994). Those data derived from the few trails with a greater within-trail variability (those with <90% of the T_hH_2O values occurring within a 10-15°C interval; section 4.1) have been ignored in this discussion. Consequently the variability between different trails (i.e. the ranges in theT_hH_2O data; Figs 6.2a-d and 6.3a-d) cannot be ascribed to the subsequent alteration of these inclusions after their entrapment. Thus the ranges in the T_hH_2O data from the D_1/D_2 veins are most likely due to the entrapment of different trails of inclusions over a period of time and under a range of different P-T conditions. Consequently, the highest T_hH_2O data should be representative of the peak metamorphic conditions, with the trend towards lower data representing microfracture closure during various stages along the retrograde path.

The lower salinity Type Ia inclusions (<10 wt% $NaCl_{eq}$) are far more abundant than the higher salinity fluids (10-16 wt% $NaCl_{eq}$) suggesting that the orogenic fluids are predominantly low salinity fluids, which is consistent with their derivation from sediments within a continental margin setting (e.g. Yardley, 1997). The higher salinity fluid inclusions do not appear to be dependent on vein generation or locality, although the majority of these data are from veins of various generations from the northern area (WSB40, 43, 96, 100). The nature of the sedimentary succession provides an important control on the composition of the metamorphic fluid at all grades (Yardley, 1997), and this is especially the case when evaporites are present within the succession. Consequently, the presence of higher salinity inclusions suggests that some of the orogenic fluids have interacted with horizons capable of raising the salinity (e.g. evaporites). Na-Cl-Br systematics provide a simple way of discriminating between different solute sources for brines (e.g. Kesler *et al.*, 1995a), and for those samples (WSB15, 40, 43, 96) in which Br contents were above the detection limit, very low Cl/Br

and Na/Br ratios were established (Fig. 6.4). These low ratios indicate that either the orogenic fluids were sourced within, or interacted with, evaporite horizons (Kesler *et al.*, 1995a), and this is consistent with the fact that the samples in which these low ratios were determined yielded the highest salinity estimates.

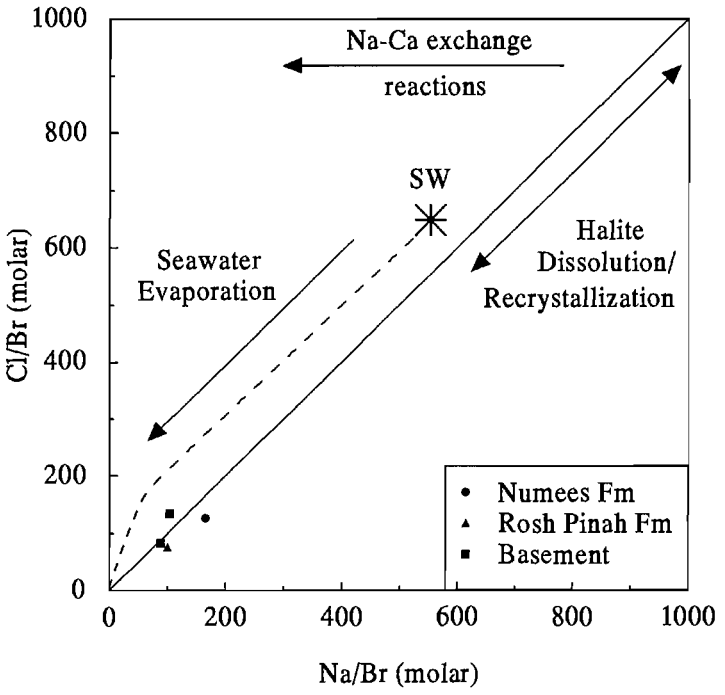

Figure 6.4 Na-Cl-Br systematics (after Kesler *et al.*, 1995a) of Gariepian fluids. Note the low molar Cl/Br and Na/Br ratios for those samples in which Br was determined.

A single trail of inclusions exhibiting low salinities (~4 wt% $NaCl_{eq}$) and a range in T_hH_2O from ~200°C to ~210°C (Appendix 4), was found in the pre-orogenic silicic footwall breccia. These data are significantly different to those related to the Rosh Pinah ore fluid (section 6.1.1), and plot within the lower portion of the range of data defined for northern area vein-hosted inclusions ascribed to D_1/D_2 event. Consequently they are regarded as orogenic inclusions.

Using the Type Ia inclusion data in conjunction with the temperature constraints from peak metamorphic mineral assemblages (Frimmel, 1995), better constraints can be placed on the poorly defined maximum metamorphic pressures recorded (Table 6.2). These new constraints indicate that higher metamorphic pressures were experienced within the

northern area (~3.4-3.6 kbar at 520°C) than elsewhere in the belt. Similar maximum metamorphic pressures (~3.1 kbar) are suggested for the central and southern areas.

Table 6.2 The ranges in maximum (recorded) metamorphic P and peak metamorphic T estimates for the various areas as determined by Frimmel (1995), and the new constraints on maximum metamorphic P estimates as determined from fluid inclusions (this study). Note that a distinction has been made between the low salinity (LS) and the high salinity (HS) inclusions present within the northern area. The new pressure constraints were calculated using the isochores shown in Fig. 6.5.

Area	Maximum metamorphic P estimates (Frimmel, 1995)	Peak metamorphic T estimates (Frimmel, 1995)	Highest T_hH_2O value and related salinity in wt% $NaCl_{eq}$	Maximum metamorphic P estimates (this study)
Northern (LS)	3.4-5.0 kbar	478-523°C	257°C; 7.5	3.0-3.6 kbar
Northern (HS)			274°C; 14.9	2.9-3.5 kbar
Central	1.3-2.9 kbar	400-420°C	216°C; 2.4	2.9-3.1 kbar
Vanrhynsdorp	2.5-5.0 kbar	400-500°C	263°C; 4.8	1.8-3.1 kbar

As the Type Ia fluid inclusions within the D_3 (Fig. 6.2d) and D_5 (Fig. 6.2a) veins exhibit T_hH_2O data which show no variation as a function of area, the P-T conditions of these events are considered to be consistent on a belt-wide scale. Consequently, the maximum pressure estimate for the D_3 and D_5 events is constrained to 3.1 kbar, as this is the maximum pressure estimate of the D_1/D_2 event in the central area. The maximum pressure estimate of 3.1 kbar can also be imposed on the D_4 veins as they are highly localised within the central area. Using these pressure constraints, together with the isochores determined for those fluid inclusion planes that yielded the highest T_hH_2O values, maximum temperature estimates of 390°C and 360°C can be calculated for the D_3 and D_5 veins, respectively (Fig. 6.5a-d). Note that the isochores were calculated using the program FLINCOR (Brown, 1989), and assuming an NaCl-H_2O system. The Brown and Lamb (1989) equation of state was used. In a similar way, maximum temperature estimates of 530°C and 470°C can be calculated for the D_4 veins close to and further away from the pluton, respectively (Fig. 6.5b). Consequently, the fluids related to the emplacement of the pluton were hotter than the fluids related to the peak regional metamorphic event in the central area. Furthermore, the inclusion fluids hosted within the two D_4 quartz vein samples exhibit the expected decrease in temperature away from the pluton. Viewing the isochores (Fig. 6.5a-d), it can be seen that, given the maximum

pressure constraints on the D_3 and D_5 events, the retrograde P-T path has to be clockwise, which is in accordance with the tectonic setting of the Gariepian orogeny. The late stage fluids from the Vanrhynsdorp area, in the light of the previous discussion, are most probably cooler than the D_1/D_2 fluids of the same area.

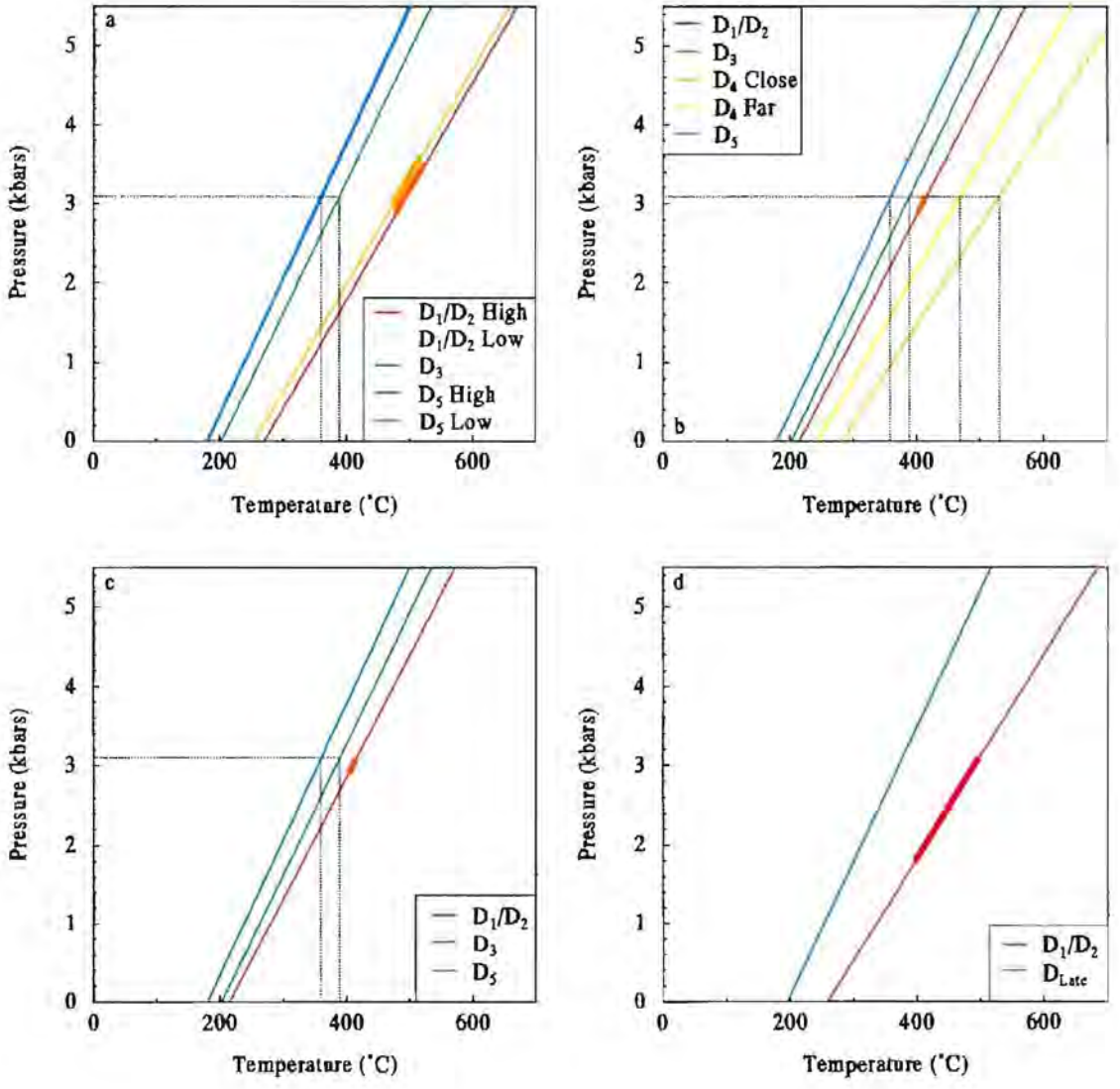

Figure 6.5 Isochores calculated for Type Ia inclusion planes, yielding the highest T_hH_2O data, hosted within the various generations of orogenic quartz veins from the various areas: (a) northern area, (b) central area, showing isochores related to the D_4 event, (c) central area, (d) Vanrhynsdorp area. The ranges in the maximum metamorphic P-T conditions (as shown in Table 6.2) are represented by the thicker sections of the isochores. The stippled lines give the temperature estimates corresponding to a maximum pressure estimate of 3.1 kbar. See text for discussion.

An approximately linear trend is developed within the data derived from the orogenic carbonic-rich inclusions (Types II and III; Fig. 6.1). Raman spectroscopy confirmed the

presence of CH_4 (and no other constituents) in the orogenic vein-hosted carbonic-rich inclusions (see section 5.5). The observed suppression of the T_hCO_2 is also related to the presence of CH_4, although it is more sensitive to changes in the amount of methane (Roedder, 1984). Consequently the approximately linear trend developed within the orogenic carbonic-rich inclusion data most probably represents a mixing line between CO_2 and CH_4. The proportion of CH_4, as determined by Raman spectroscopy (Table 5.3), within the inclusions is in good agreement with the microthermometric results (see Fig. 2 in Hall and Bodnar, 1990). As much as 20-25% CH_4 (Hall and Bodnar, 1990) is suggested by the lowest T_mCO_2 values (-60.4°C) obtained from the orogenic vein-hosted inclusions. It should be noted that only those carbonic inclusions from veins hosted by graphitic schists of the Rosh Pinah Formation and black schists of the Numees Formation, yield significantly suppressed T_mCO_2 and T_hCO_2 values. This fact, together with the observation that the rest of the orogenic vein-hosted carbonic-rich inclusions (from a wide variety of host-rocks) yield T_mCO_2 and T_hCO_2 values near those expected for pure CO_2, suggests a degree of host-rock control (with respect to the CH_4 content) on the orogenic fluids.

The significantly greater abundance of the Type Ia inclusions relative to the carbonic-rich inclusions (Types II and III) within the orogenic veins, suggests that the orogenic fluids were dominantly aqueous, and that the carbonic component was derived by the interaction of the orogenic fluids with carbonate-bearing host-rocks. The presence of carbonic-rich inclusions within veins hosted by essentially carbonate-free host-rocks (e.g. WSB 40, WSB49, WSB106 and WSB149) from the outer margin of the belt suggests that fluid flow during the orogeny occurred on a larger, more regional scale than on a localised (intra-formational) scale. The expulsion of the fluids related to the D_1/D_2 event towards the foreland (i.e. to the east and southeast; Frimmel, 1995), suggests that the carbonates of the Hilda Subgroup are the most probable source of the carbonic component within the orogenic fluids.

According to Shepherd *et al.* (1985), there is an extremely high probability of trapping immiscible fluids in the system H_2O-NaCl-CO_2 due to fluid unmixing. Consequently, the Type Ib and the orogenic Type II inclusions are possibly representatives of the carbonic-

bearing and the carbonic-rich end-members, respectively, that were formed due to immiscibility between CO_2 and H_2O prior to inclusion entrapment. In order to determine the bulk composition (in terms of CO_2 and H_2O) of the original fluid from which the fluid in the Type Ib and Type II inclusions unmixed, the relative proportions of CO_2 and H_2O at the temperature of unmixing need to be known. The large errors involved in the visual estimation of the volume proportions of the CO_2-rich bubble (Type II inclusions) precludes the calculation of the relative proportions of CO_2 and H_2O using the various equations that exist for the H_2O-CO_2-NaCl system (e.g. Bowers and Helgeson, 1983; Brown and Lamb, 1989). The Type II inclusions continually decrepitated over a range of temperatures before total homogenisation had occurred, thus precluding the use of the homogenisation temperatures of these inclusions as estimates of the unmixing temperature. Furthermore, as the relationship between the majority of the Type Ib and Type II inclusions is unknown, there is no way of assessing which of the Type II inclusions corresponds to which of the Type Ib inclusions. Consequently, the total homogenisation temperatures of the Type II inclusions cannot be estimated by using the T_hH_2O data of the Type Ib inclusions. As a result of this, the temperature of unmixing cannot be estimated and consequently no statements can be made about the proportions of CO_2 and H_2O within the parent fluid. The similarity in the clathrate values of the Type Ib and orogenic Type II inclusions, however, indicates that the salinity estimates of these inclusions are most probably representative of the bulk salinity of the parent fluid.

6.2 Stable Isotopes

The observed trend towards higher orogenic vein $\delta^{18}O$ values up stratigraphy (Fig. 5.7d) could be due to polythermal exchange between the host-rock and the orogenic fluids (Valley, 1986) in response to the existence of a temperature gradient across the belt (an increase in T towards the MT). Frimmel (1995) indicates that there are no apparent differences in the peak metamorphic P-T conditions as a function of stratigraphy within the outer margin of the belt (PNZ), and consequently the variation in the orogenic vein $\delta^{18}O$ values with stratigraphy is probably not reflective of a polythermal trend.

The lack of variation in the orogenic vein $\delta^{18}O$ values in terms of vein generation, geographical position and vein mineralogy (Fig. 5.7a-c), together with the trend in the $\delta^{18}O$ values as a function of host-rock (Fig. 5.7d), are suggestive of a rock-buffered fluid system (e.g. Gray *et al.*, 1991). The strong correlation between the $\delta^{18}O$ values of the quartz veins and their respective host-rocks (Fig. 5.8) strengthen this argument. The lack of evidence for contamination of the vein quartz by host-rock quartz (as shown by the SEM-Cathodoluminescence images; Fig. 5.12) precludes the possibility that the correlation between the $\delta^{18}O_{qtz}$ and $\delta^{18}O_{host}$ values is due to such contamination. The average shift (1.7‰) towards higher $\delta^{18}O_{qtz}$ values relative to corresponding $\delta^{18}O_{host}$ values is rather due to the fact that the latter are whole rock values, which are dependant on mineralogy (Valley, 1986), and not the values of host-rock quartz grains.

The existence of carbonic-rich inclusions in veins hosted within essentially carbonate-free rocks (e.g. quartzites of the Stinkfontein Subgroup), suggests that a completely rock-dominated orogenic fluid system, characterised by little or no fluid communication between stratigraphic levels (e.g. Evans and Battles, 1997), is probably not the case in the outer Gariep Belt. The few 'outlier' values in Fig. 5.8 (those with a >2.5‰ shift towards higher $\delta^{18}O_{qtz}$ values for a given $\delta^{18}O_{host}$) may be indicative of a degree of open system behaviour (e.g. Evans and Battles, 1997), supporting the contention of fluid flow on a more regional scale. Advective fluid flow through the lithosphere can be subdivided into two extremes: pervasive and channelled flow (e.g. Valley, 1986; Frimmel, 1992), with real systems representing a combination of the two extremes. As the orogenic veins are hosted by fractures, faults and shear zones, the latter type of fluid flow is most probably dominant within the outer margin of the Gariep Belt. This implies that flow rates were probably relatively high, with a fairly low degree of infiltration from the fracture surface into the country rock (e.g. Frimmel, 1992). Consequently, a fairly rapid rate of oxygen isotope exchange between the orogenic fluids and the host-rock is suggested in order to explain the observed host-rock control on $\delta^{18}O$.

The range in $\delta^{18}O$ values for orogenic quartz veins hosted within carbonate rocks is much higher than for those veins hosted within all other rock types (Fig. 5.7d),

suggesting that a different fluid system is developed within the carbonates. The scarcity of veins hosted within carbonate horizons compared with the abundance of veins hosted within the metapelites and other host-rock types (section 3.1.1), indicates that the carbonates were relatively more impermeable with respect to fluid flow than the other host-rocks. This is consistent with the contention in the literature that marbles are relatively impermeable units in metamorphic terranes (e.g. Schwarcz *et al.*, 1970). The strong host-rock control with respect to the $\delta^{18}O_{qtz}$ values (Fig. 5.8), coupled with the generally small size and relative abundance of the veins hosted within the carbonates (section 3.1.1), suggests that the vein system within these rocks is largely rock-dominated. Quartz veins, although rare, are present within the Pickelhaube Formation, yet no veins were observed within the Dabie River Formation. This may be due to the fact that the Pickelhaube Formation carbonates contain quartz (albeit in minor proportions) whereas the carbonates of the Dabie River Formation do not (Von Veh, 1993). The carbonic-rich component within the aqueous orogenic fluids most probably represents contamination of these fluids along fractures at the contacts between the carbonate units and adjacent rocks, and from the carbonate component within the highly siliceous, more permeable Wallekraal Formation.

Hydrogen and oxygen stable isotope analyses provide an insight into the source of the H_2O because natural waters of various origins display systematic differences in their deuterium and ^{18}O contents (Taylor, 1997). The few samples from which both $\delta^{18}O_{qtz}$ and δD were determined (see section 5.2.2) are plotted on Fig. 5.9. Taking the quartz-water fractionation factor into account, the $\delta^{18}O_{fluid}$ values would be shifted to the left on this diagram. The fact that there is a strong host-rock control on the orogenic fluids in terms of $\delta^{18}O$ precludes the use of oxygen isotopes in making definitive statements as to the source of the fluids. This is because of the consistency of the T_hH_2O data for each generation from each area (see section 6.1.2) meaning similar fractionation factors, in turn, for each vein generation from each area hosted within different rocks. In other words, the D_1/D_2 veins from the northern area have similar fractionation factors due to similar temperatures of formation, regardless of host-rock, so too the D_1/D_2 veins from the central area, etc. Hence the trend of increasing $\delta^{18}O_{qtz}$ up stratigraphy (Fig. 5.7d) is

mirrored by the $\delta^{18}O_{fluid}$ values, with the ranges in $\delta^{18}O_{fluid}$ being determined by the host-rock. Consequently the ranges in the $\delta^{18}O_{fluid}$ are not reflective of the original $\delta^{18}O_{fluid}$ (if fluid flow is on a regional scale) precluding the use of a δD vs. $\delta^{18}O_{fluid}$ diagram in the determination of possible fluid sources. However, constraints can be placed on the possible sources of the orogenic fluids using the model of fluid circulation within a regional metamorphic belt as proposed by Etheridge *et al.* (1983). As ductile structures are associated with the D_1/D_2 event, it can be expected that fluids related to this event are a mixture of circulating formation waters and the products of metamorphic devolatilisation reactions (e.g. Etheridge *et al.*, 1983; Yardley, 1997). The brittle structures associated with the D_3 to D_5 events (Von Veh, 1993) suggest shallower crustal levels during the transtensive events, and hence fluid flow was most probably dominated by meteoric fluid circulation (Etheridge *et al.*, 1983).

7. CONCLUSIONS

Two principally different types of fluid were distinguished, on the basis of their chemistry and host-rock associations, in the external zone of the Gariep Belt: the pre-orogenic, rift-related Rosh Pinah ore-forming fluid, and the orogenic fluids. The Rosh Pinah ore-forming fluid is far more saline than, and chemically distinct from, the orogenic inclusion fluids from within the mine and on a regional scale. The ore-forming fluid is chemically complex, with a suggested chemistry of $CaMg(CO_3)_2$, NaCl, CO_2 and other gaseous species like CH_4 and H_2S, various sulphates, carbonates and chlorides of Na, K, Ca, Mg (in minor quantities), and probably base metals. The ore-forming fluid is most likely a representative of hot, chemically evolved hypersaline brines that were induced by rift-related magmatism and which were most probably responsible for the transport of base metals away from centres of magmatic and volcanic activity, and the subsequent replacement of dolomitic horizons with associated base metal sulphide mineralisation. Sedimentological evidence (section 2.2) suggests the expulsion of some of these fluids onto the sea floor.

On a regional scale, four generations of orogenic veins can be recognised on the basis of their relationship to the regional structure: D_1/D_2; D_3; D_4 and D_5. Inclusion fluids from these veins are chemically similar (generally NaCl, $CaCl_2$ and H_2O), dominantly aqueous and generally exhibit moderate to low salinities (<10 wt% $NaCl_{eq}$), regardless of host-rock and geographical position. Higher salinity (10-16 wt% $NaCl_{eq}$) orogenic fluids are recognised from the northern area. Low Cl/Br and Na/Br ratios correspond to these higher salinity fluids, suggesting that either these fluids were sourced within, or interacted with, evaporite horizons (Kesler *et al.*, 1995a).

A general trend, in terms of T_hH_2O data, of $D_4>D_1/D_2>D_3>D_5$ can be recognised within the aqueous inclusion dataset, regardless of host-rock. D_1/D_2 inclusion fluids from the northern and Vanrhynsdorp areas were hotter than the central area fluids, whereas the D_3 and D_5 inclusion fluids exhibit no apparent T_hH_2O variation as a function of geographical position. The D_4 veins closest to the Kuboos Pluton yield higher T_hH_2O values than those

further from the pluton. The aqueous inclusion microthermometric data from this study, together with the peak metamorphic temperature constraints determined from the mineral assemblages (Frimmel, 1995), place better constraints on the poorly defined maximum metamorphic pressure estimates. New maximum metamorphic pressure estimates for the northern area, central area and Vanrhynsdorp areas are 2.9-3.6 kbar, 2.9-3.1 kbar and 1.8-3.1 kbar, respectively.

The presence of carbonic inclusions within essentially carbonate-free host-rocks (e.g. basement granite and quartzites of the Stinkfontein Subgroup), their relative abundance, and the general chemical uniformity of the orogenic inclusion fluids, suggests fluid flow on a regional rather than on an intra-formational scale. The carbonates of the Hilda Subgroup are the most likely source of the carbonic component within the orogenic fluids, and this component probably represents contamination of these fluids along fractures at the contacts between the carbonate units and adjacent rocks. Similarly, the CH_4 present within a few samples probably represents contamination of fluids passing through CH_4-bearing host-rocks (e.g. graphitic schists).

No variation, in terms of $\delta^{18}O$ as a function of geographical position, vein generation and vein type, is evident. The strong correlation between the $\delta^{18}O$ values of the quartz veins and their respective host-rocks suggest that the oxygen isotopic composition of the orogenic fluids is completely rock-buffered. The range in $\delta^{18}O$ values for orogenic quartz veins hosted within carbonate rocks is much higher than for those veins hosted within all other rock types, suggesting that a different fluid system is developed within the carbonates. The strong host-rock control with respect to the $\delta^{18}O_{qtz}$ values, coupled with the generally small size and relative abundance of the veins hosted within the carbonates suggests that the vein system within these rocks is largely rock-dominated.

As channeled fluid flow, evidenced by fracture-, fault- and shear zone-hosted veins, appears to be the most dominant type of flow within the outer margin of the Gariep Belt, relatively high flow rates, with a fairly low degree of infiltration into the country rock (Frimmel, 1992), are implied. Consequently, a fairly rapid rate of oxygen isotope exchange

between the orogenic fluids and the host-rock is suggested in order to explain the observed host-rock control on $\delta^{18}O$. Similarly, the CO_2 and CH_4 contents of the orogenic fluids necessitate fairly rapid exchange (in terms of these components) between the host-rock and the fluid.

The D_1/D_2 fluids were most probably circulating formation and metamorphic waters that were forced by advective, channeled flow out of the orogen and into the foreland, whereas channeled meteoric fluid flow most likely dominated during the transtensive phase of the orogeny. The fluids related to the D_4 event probably contain a magmatic fluid component (as evidenced by the presence of feldspar within these veins) in addition to the meteoric component.

Mineralising potential

Within the mine, minor localised remobilisation of the ore-forming minerals can be seen in the orogenic veins that crosscut the ore bodies. The chemistry of the fluids from the mine-hosted orogenic quartz veins and secondary remobilised sulphides is very similar to that of the regional orogenic fluids, with the exception of (expected) high SO_4^{2-} contents within the sulphide-hosted inclusion fluids. These observations indicate that the orogenic fluids have neither the required salinities, nor the required chemistry necessary in order to transport sufficient metals to produce a massive sulphide deposit the size of Rosh Pinah. This is highlighted by the fact that fluids with high salinities have compositions favourable for the transportation of metals whereas only a few elements are mobile in low-salinity fluids (Phillips *et al.*, 1994). Given that the moderate to low salinities of the orogenic fluids are sufficient to induce minor, localised remobilisation of base-metals within the mine, the scavenging and transport of very low concentrations of metals by these fluids is quite plausible (e.g. Phillips *et al.*, 1994). Where these orogenic fluids mix with much lower salinity meteoric fluids (e.g. in fractures etc.), precipitation of their metal contents will be induced. This is most likely the explanation of the localised showings of mineralisation throughout the belt (see section 2.3 and De Villiers and Söhnge, 1959). Consequently, the orogenic quartz veins are not considered useful to base metal exploration in the outer

margin of the Gariep Belt. The chemistry of the orogenic fluids are, however, similar to those associated with gold remobilisation and mineralisation (e.g. Frimmel *et al.*, 1993; Manu, 1991) and as such the potential for gold mineralisation related to these orogenic fluids should not be ruled out. Fold hinges could represent ideal structural traps for the deposition of gold.

Recommendations

Base metal sulphide exploration in the outer margin of the Gariep Belt should be confined to rocks of the Hilda Subgroup. Quartz veins which are clearly pre-orogenic, or which show no apparent relationship to the various deformation events, and which contain highly saline and chemically complex fluid inclusions similar to the Rosh Pinah ore-forming fluid of this study, are considered critical to base metal sulphide exploration. Veins hosting low salinity, chemically simple inclusions are most probably orogenic fluids and can be ignored.

ACKNOWLEDGEMENTS

I would like to thank the mine manager, Mr D. Southey, and the staff of the Rosh Pinah mine, in particular Mr D. Alchin, Mr T. Blaauw and Mr B. Briedenhahn, for their advice, assistance and companionship during my stay at the mine. Mr N. Kotze and Mr D. de Bruin are thanked for their kind permission in allowing me to work on the farms Spitskop 111 and Namuskluft respectively. Furthermore, I wish to thank the Head warden of the Richtersveld National Park, Mr Paddy Gordon, and the mine manager of the Ochta Reuning mine, Mr J.S. Mostert, for their kind permission in allowing me to conduct fieldwork, within the National Park and the diamond mining area respectively. I am grateful to Mr Paul Macey and Mr Peter Fölling for their help and companionship during my fieldwork south of the Orange River, and to my supervisor, Assoc. Prof. H. Frimmel, for the loan of his personal 4x4, even if it spent a night on the rocks.

I wish to thank the staff of the University of Cape Town, in particular the staff of the Department of Geological Sciences, for their efficient assistance in both the library and the laboratories. Dane Gerneke from the Electron Microscope Unit is thanked for his assistance with the SEM cathodoluminescence, Nellie Mutemeri for conducting the Raman Spectroscopy and I am grateful to Deshenthree Chetty for her assistance with regards to the crush-leach analysis.

A special word of thanks goes to Mineral Services for allowing me to use their digitising and GIS equipment in the compilation of the map that accompanies this work.

Finally, I wish to thank my parents and sister for their support throughout the duration of this project.

REFERENCES

Allsopp, H.L., Köstlin, E.O., Welke, H.J., Burger, A.J., Kröner, A. and Blignault, H.J., 1979. Rb-Sr and U-Pb geochronology of late Precambrian - early Palaeozoic igneous activity in the Richtersveld (South Africa) and southern South West Africa. *Trans. Geol. Soc. S. Afr.*, **82**: 185-204.

Apel, M.A., 1997. Structural geology and metamorphism of the Namaqualand Metamorphic Complex and Pan-African cover rocks in the Sout River area southwest of Bitterfontein, Northern Cape Province. *Unpubl. Honours thesis*, Univ. Cape Town, 39p.

Barker, A.J., 1995. Post-entrapment modification of fluid inclusions due to overpressure: evidence from natural samples. *J. Metam. Geol.*, **13**: 737-750.

Barker, C.E. and Reynolds, T.J., 1984. Preparing doubly polished sections of temperature sensitive sedimentary rocks. *Jour. of Sed. Petrology*, **54**: 635-636.

Barton, E.S., 1983. Reconnaissance isotopic investigations in the Namaqua Mobile Belt and implications for Proterozoic crustal evolution - Namaqualand Geotraverse. *Geol. Soc. S.Afr. Spec. Publ.*, **10**: 45-66.

Bodnar, R.J., 1993. Revised equation and table for determining the freezing point depression of H_2O-NaCl solutions. *Geochim. et Cosmochim. Acta*, **57**: 683-684.

Bodnar, R.J., Binns, P.R. and Hall, D.L., 1989. Synthetic fluid inclusions VI. Quantitative evaluation of the decrepitation behaviour of fluid inclusions in quartz at one atmosphere confining pressure. *J. Metam. Geol.*, **7**: 229-242.

Borthwick, J. and Harmon, R.S., 1982. A note regarding ClF_3 as an alternative to BrF_5 for oxygen isotope analysis. *Geochim. et Cosmochim. Acta*, **46**: 1665-1668.

Bowers, T.S. and Helgeson, H.C., 1983. Calculation of thermodynamic and geochemical consequences of nonideal mixing in the system H_2O-CO_2-NaCl on phase relations in geologic systems: Equation of state for H_2O-CO_2-NaCl fluids at high pressures and temperatures. *Geochim. et Cosmochim. Acta*, **47**: 1247-1275.

Bozzo, A.T., Chen, H-S., Kass, J.R. and Barduhn, A.J., (1973). The properties of the hydrates of chlorine and carbon dioxide. *In*: A. Delyannis and E. Delyannis (Editors), *The Fourth International Symposium on Fresh Water from the Sea*, **Vol. 3**: 437-451.

Brown, P.E., 1989. FLINCOR: A microcomputer program for the reduction and investigation of fluid inclusion data. *Am. Mineral.*, **74**: 1390-1393.

Brown, P.E. and Lamb, W.M., 1989. P-V-T properties of fluids in the system H_2O-CO_2-NaCl: New graphical presentations and implications for fluid inclusion studies. *Geochim. et Cosmochim. Acta.*, **53**: 1209-1221.

Burke, E.A.J. and Lustenhouwer, W.J., 1987. The application of a multichannel laser Raman microprobe (Microdil-28®) to the analysis of fluid inclusions. *In*: E.E. Horn and H.-J. Behr (Guest Editors), *Current Research on Fluid Inclusions, ECRFI, Göttingen, April 10-12, 1985. Chem. Geol.*, **61**: 11-17.

Chen, H-S., 1972. The properties of carbon dioxide hydrate. Office of Saline Water, *Research and Development Progress Report No. 830, November 1972*, p 1-55.

Chetty, D., 1998. Geochemical fingerprinting of carbonate wall rock alteration at major base metal sulphide deposits in the Otavi mountain land, Namibia. *Unpubl. M.Sc. thesis*, Univ. Cape Town, 147p.

Clayton, R.N. and Mayeda, T.K., 1963. The use of bromine pentafluoride in the extraction of oxygen from oxides and silicates for isotopic analysis. *Geochim. et Cosmochim. Acta*, **27**: 43-52.

Coleman, M.L., Shepherd, T.J., Durham, J.J., Rouse, J.E. and Moore, G.R., 1982. Reduction of water with zinc for hydrogen isotope analysis. *Anal. Chem.*, **54**: 993 -995.

Collins, P.L.F., 1979. Gas hydrates in CO_2-bearing fluid inclusions and the use of freezing data for estimation of salinity. *Econ. Geol.*, **74**: 1435-1444.

Coplen, T.B., 1988. Normalization of oxygen and hydrogen isotope data. *Chem. Geol. (Isot. Geosci. Sect.)*, **72**: 293-297.

Coplen, T.B., Kendall, C. and Hopple, J., 1983. Comparison of stable isotope reference samples. *Nature*, **302**: 236-238.

Coward, M.P., 1983. The tectonic history of the Damara Belt. *In*: R. McG. Miller (Editor), *Evolution of the Damara Orogen*, Geol. Soc. S. Afr. Spec. Publ., **11**: 409-421.

Craig, H., 1961. Isotopic variations in meteoric waters. *Science*, **133**: 1702-1703.

Crawford, M.L., 1981. Phase equilibria in aqueous fluid inclusions. *In*: L.S. Hollister and M.L. Crawford (Editors), *Fluid Inclusions: Applications to Petrology*, Mineral. Assoc. Canada Short Course Handbook **6**: 75-100.

Darling, R.S., 1991. An extended equation to calculate NaCl contents from final clathrate melting temperatures in H_2O-CO_2-NaCl fluid inclusions: Implications for P-T isochore location. *Geochim. et Cosmochim. Acta*, **55**: 3869-3871.

Davies, C.J. and Coward, M.P., 1982. The structural evolution of the Gariep Arc in southern Namibia (South-west Africa). *Precamb. Res.*, **17**: 173-198.

Davis, D.W., Lowenstein, T.K. and Spencer, R.J., 1990. Melting behaviour of fluid inclusions in laboratory-grown halite crystals in the systems NaCl-H_2O, NaCl -KCl-H_2O, NaCl-$MgCl_2$-H_2O, and NaCl-$CaCl_2$-H_2O. *Geochim. et Cosmochim. Acta*, **54**: 591-601.

Deffontaine, A., Bridoux, M., Delhaye, M., Da Silva, E. and Hug, W., 1984. The third generation of multichannel Raman spectrometers. *Rev. Phys. Appl.*, **19**: 415-421.

Delhaye, M., Bridoux, M., Dhamelincourt, P., Barbillat, J., Da Silva, E. and Roussel, B., 1982. A new generation of laser microspectrometers: Micromars. *In*: K.F.J. Heinrich (Editor), *Microbeam Analysis – 1982.* San Francisco Press, Sand Francisco, California, p. 275-278.

De Villiers, J. and Söhnge, P.G., 1959. The Geology of the Richtersveld. *Mem. Geol. Surv. Dep. Min. S. Afr.*, **48**: 295p.

Duan, Z., Møller, N. and Weare, J.H., 1995. Equation of state for the NaCl-H_2O-CO_2 system: Prediction of phase equilibria and volumetric properties. *Geochim. et Cosmochim. Acta*, **59**: 2869-2882.

Dubois, M. and Marignac, C., 1997. The H_2O-NaCl-$MgCl_2$ ternary phase diagram with special application to fluid inclusion studies. *Econ. Geol.*, **92**: 114-119.

Erongo Exploration and Mining Company Ltd and Reunion Mining PLC, 1996. Visit to Skorpion Prospect by members of the Geological Society of Namibia. REF. 13/175/5048/SCK/96/107.

Etheridge, M.A., Wall, V.J. and Vernon, R.H., 1983. The role of the fluid phase during regional metamorphism and deformation. *J. Metam. Geol.*, **1**: 205-226.

Evans, M.A. and Battles, D.A., 1997. Regional syn-orogenic fluid migration in the Central Appalachians: fluid geochemistry and fluid migration pathways. *In*: J.P. Hendry, P.F. Carey, J. Parnell, A.H. Ruffell and R.H. Worden (Editors), *GEOFLUIDS II: Second International Conference on Fluid Evolution, Migration and Interactions in Sedimentary Basins an Orogenic Belts, Extended Abstracts*, Queens University, Belfast, 85-88.

Fernandes, L.A.D. and Koester, E., 1998. The Dorsal de Canguçú strike-slip shear zone: its nature and role in the tectonic evolution of the continental crust in Southern Brazil during the Neoproterozoic. *J. Afr. Earth Sci.* **27**: p.72.

Fernandes, L.A.D., Tommasi, A. and Porcher, C.C., 1992. Deformation patterns in the southern Brazilian branch of the Dom Feliciano Belt, a reappraisal. *J. S. Am. Earth Sci.*, **5**: 77-96.

Frimmel, H.E., 1992. Isotopic fronts in hydrothermally mineralized carbonate rocks. *Mineral. Deposita*, **27**: 257-267.

Frimmel, H.E., 1995. Metamorphic evolution of the Gariep Belt. *S. Afr. J. Geol.*, **98**: 176-190.

Frimmel, H.E. and Frank, W., 1998. Neoproterozoic tectono-thermal evolution of the Gariep Belt and its basement, Namibia and South Africa. *Precamb. Res.*, **90**: 1-28.

Frimmel, H.E. and Hartnady, C.J.H., 1992. Blue amphiboles and their significance for the metamorphic history of the Pan-African Gariep belt, Namibia. *J. metam. Geol.*, **10**: 651-669.

Frimmel, H.E., Hartnady, C.J.H. and Koller, F., 1996a. Geochemistry and tectonic setting of magmatic units in the Pan-African Gariep Belt, Namibia. *Chem. Geol.*, **130**: 101-121.

Frimmel, H.E., Klötzli, U.S. and Siegfried, P.R., 1996b. New Pb-Pb single zircon age constraints on the timing of Neoproterozoic glaciation and continental break-up in Namibia. *Jour. Geol.*, **104**: 459-469.

Frimmel, H.E., Le Roex, A.P., Knight, J. and Minter, W.E.L., 1993. A case study of the postdepositional alteration of the Witwatersrand Basal Reef gold placer. *Econ. Geol.*, **88**: 249-265.

Fyfe, W.S., Price, N.J. and Thompson, A.B., 1978. *Fluids in the Earth's Crust.* Elsevier, Amsterdam, 383p.

Gartz, V.H., Frimmel, H.E. and Gerneke, D., 1995. The Application of SEM -Cathodoluminescence to Witwatersrand Quartz. *In*: J.M. Barton and Y.E. Copperthwaite (Editors*), Centennial Geocongress 1995 – Extended Abstracts Vol. (II)*. Geol. Soc. S. Afr., p. 923-926.

Germs, G.J.B., 1995. The Neoproterozoic of southwestern Africa, with emphasis on platform stratigraphy and paleontology. *Precamb. Res.*, **73**: 137-151.

Germs, G.J.B. and Gresse, P.G., 1991. The foreland basin of the Damara and Gariep orogens in Namaqualand and southern Namibia: stratigraphic and basin dynamics. *S. Afr. J. Geol.*, **94**: 159-169.

Goldstein, R.H. and Reynolds, T.J., 1994. *Systematics of Fluid Inclusions in Diagenetic Minerals.* SEPM Short Course 31, 207p.

Gray, D.R., Gregory, R.T. and Durney, D.W., 1991. Rock-buffered fluid-rock interaction in deformed quartz-rich turbidite sequences, eastern Australia. *J. Geophys. Res.*, **96**: 19681-19704.

Gresse, P.G., Fitch, F.J. and Miller, J.A., 1988. ^{40}Ar-^{39}Ar dating of the Cambro-Ordovician Vanrhynsdorp tectonite in southern Namaqualand. *S.Afr. J. Geol.*, **91**: 257-263.

Gresse, P.G., 1994. Strain partitioning in the Southern Gariep Arc as reflected by sheath folds and stretching directions. *S. Afr. J. Geol.*, **97**: 52-61.

Gresse, P.G. and Germs, G.J.B., 1993. The Nama foreland basin: sedimentation, major unconformity bounded sequences and multisided active margin advance. *Precamb. Res.*, **63**: 247-272.

Grotzinger, J.P., Bowring, S.A., Saylor, B.Z. and Kaufman, A.J., 1995. Biostratigraphic and geochronologic constraints on early animal evolution. *Science*, **270**: 598-604.

Guilbert, J.M. and Park, C.F., 1986. *The geology of ore deposits.* W.H. Freeman and Company, New York, 995p.

Hälbich, I.W. and Alchin, D.J., 1995. The Gariep belt: stratigraphic-structural evidence for obliquely transformed grabens and back-folded thrust stacks in a combined thick-skin thin-skin structural setting. *J. Afr. Earth Sci.*, **21**: 9-33.

Harris, C. and Erlank, A.J., 1992. The production of large volume low-$\delta^{18}O$ rhyolites during the rifting of Africa and Antarctica: the Lebombo Monocline, southern Africa. *Geochim. et Cosmochim. Acta*, **56**: 3561-3570.

Hartman, M., Trnka, O., Veselý, V. and Svoboda, K., 1996. Predicting the rate of thermal decomposition of dolomite. *Chem. Eng. Sci.*, **51**: 5229-5232.

Hartnady, C.J.H., Joubert, P. and Stowe, C.J.H., 1985. Proterozoic crustal evolution in southwestern Africa. *Episodes*, **8**: 236-244.

Hartnady, C.J.H., Ransome, I.G.D. and Frimmel, H.E., 1990. Accreted composite terranes-an example from the Gariep orogenic belt. *Abstracts Geocongress '90*, Geol. Soc. S. Afr., Cape Town, p. 218-221.

Hoffman, P.F., Bowring, S.A. and Isachsen, C.E., 1994. New U-Pb zircon ages for the early Damaran Oas syenite (Welwitchia inlier) and upper Naauwpoort volcanics (Summas Mts), Namibia. *Abstracts Geol. Soc. Namibia, Proterozoic Crustal and Metallogenic evolution*, Windhoek, p. 32.

ISODAT operating manual, Issue: (4/93 REV. A) 8-5 – 8-12. Finnigan MAT.

Kaufman, A.J., Hayes, J.M., Knoll, A.H. and Germs, G.J.B., 1991. Isotopic compositions of carbonates and organic carbon from Upper Proterozoic successions in Namibia: Stratigraphic variation and the effects of diagenesis and metamorphism. *Precamb. Res.*, **49**: 301-327.

Kesler, S.E., Appold, M.S., Martini, A.M., Walter, L.M., Huston, T.J. and Kyle, J.R., 1995. Na-Cl-Br systematics of mineralizing brines in Mississippi Valley-type deposits. *Geology*, **23**: 641-644.

Kesler, S.E., Martini, A.M., Appold, M.S., Walter, L.M., Huston, T.J. and Furman, F.C., 1996. Na-Cl-Br systematics of fluid inclusions from Mississippi Valley-type deposits, Appalachian Basin: Constraints on solute origin and migration paths. *Geochim. et Cosmochim. Acta*, **60**: 225-233.

Krauskopf, K.B. and Bird, D.K., 1995. *Introduction to geochemistry.* 3rd Edition, McGraw-Hill, New York, 647p.

Manu, J., 1991. Fluid inclusions in quartz veins in the Birmian gold deposits of Ghana. *In*: M. Pagel and J.L. Leroy (Editors), *Source, Transport and Deposition of Metals*, Balkema, Rotterdam, p. 673-675.

Marshall, D.J., 1984. *Cathodoluminescence of geological materials.* Unwin Hyman, Boston, 137p.

Martin, H. and Porada, H., 1977. The intracratonic branch of the Damara orogen in South West Africa. Part 1. Discussion of geodynamic models. *Precamb. Res.*, **5**: 311-338.

McKibben, M.A. and Hardie, L.A., 1997. Ore-forming brines in active continental rifts. *In* H.L. Barnes (Editor), *Geochemistry of Hydrothermal Ore Deposits*, 3rd ed., John Wiley and Sons, New York, p. 877-935.

Meert, J.G. and van der Voo, R., 1994. The Neoproterozoic (1000-540 Ma) glacial intervals: No more snowball earth? *Earth Planet. Sci. Lett.*, **123**: 1-13.

Miller, R.M., 1983. The Pan-African Damara orogen of South West Africa-Namibia. *Geol. Soc. S. Afr. Spec. Publ.*, **11**: 431-515.

Oakes, C.S., Bodnar, R.J. and Simonson, J.M., 1990. The system NaCl-$CaCl_2$-H_2O: I. The ice liquidus at 1 atm total pressure. *Geochim. et Cosmochim. Acta*, **54**: 603-610.

Onstott, T.C., Hargraves, R.B. and Reid, D.L., 1986. Constraints on the tectonic evolution of the Namaqua Province III: Palaeomagnetic and $^{40}Ar/^{39}Ar$ results from the Gannakouriep dyke swarm. *Trans. Geol. Soc. S. Afr.*, **89**: 171-183.

Phillips, G.N., Williams, P.J. and De Jong, G., 1994. The nature of metamorphic fluids and significance for metal exploration. *In*: J. Parnell (Editor), *Geofluids: Origin, Migration and Evolution of Fluids in Sedimentary Basins.* Geol. Soc. Spec. Publ., **78**: 55-68.

Porada, H., 1983. Geodynamic model for the geosynclinal development of the Damara orogen, Namibia/South West Africa. *In*: H. Martin and F.W. Eder (Editors), *Intracontinental Fold Belts.* Springer, Berlin, p. 503-542.

Porada, H., 1989. Pan-African rifting and orogenesis in southern to equatorial Africa and eastern Brazil. *Precamb. Res.*, **44**: 103-136.

Prave, A.R., 1996. Tale of three cratons: Tectonostratigraphic anatomy of the Damara orogen in northwestern Namibia and the assembly of Gondwana. *Geology*, **24**: 1115-1118.

Reid, D.L., Ransome, I.G.D., Onstott, T.C. and Adams, C.J., 1991. Time of emplacement and metamorphism of Late Precambrian mafic dykes associated with the Pan-African Gariep orogeny, southern Africa: implications for the age of the Nama Group. *J. Afr. Earth Sci.*, **13**: 531-541.

Roedder, E, 1984. Fluid inclusions. *Mineral. Soc. Am., Rev. Mineral.*, **12**: 644p.

Schwarcz, H.P., Clayton, R.N. and Mayeda, T., 1970. Oxygen isotopic studies of calcareous and pelitic metamorphic rocks, New England. *Geol. Soc. Am. Bull.*, **81**: 2299-2316.

Shepherd, T.J., Rankin, A.H. and Alderton, D.H.M., 1985. *A practical guide to fluid inclusion studies.* Blackie and Son, Glasgow, 239p.

Siegfried, P.R., 1990. Aspects of the geology of the Mountain Ore Body, Rosh Pinah Mine, Namibia. *Unpubl. M.Sc. thesis*, Univ. Cape Town, 146p.

Siegfried, P.R. and Moore, J.M., 1990. The Rosh Pinah Zn-Pb-Cu-Ag massive sulphide deposit - a product of early rift-related volcanism? *Abstracts Geocongress '90*, Geol. Soc. S. Afr., Cape Town, p. 512-513.

Stanistreet, I.G., Kukla, P.A. and Henry, G., 1991. Sedimentary basinal responses to a Late Precambrian Wilson Cycle: the Damara Orogen and Nama Foreland, Namibia. *J. Afr. Earth Sci.*, **13**: 141-156.

Sterner, S.M. and Bodnar, R.J., 1984. Synthetic fluid inclusions in natural quartz. I. Compositional types synthesized and applications to experimental geochemistry. *Geochim. et Cosmochim. Acta*, **48**: 2659-2668.

Sterner, S.M., Hall, D.L. and Bodnar, R.J., 1988. Synthetic fluid inclusions. V. Solubility relations in the system NaCl-KCl-H_2O under vapour-saturated conditions. *Geochim. et. Cosmochim. Acta*, **52**: 989-1005.

Sterner, S.M. and Bodnar, R.J., 1989. Synthetic fluid inclusions. VII. Re-equilibration of fluid inclusions in quartz during laboratory-simulated metamorphic burial and uplift. *J. Metam. Geol.*, **7**: 243-260.

Taylor, H.P. Jr., 1997. Oxygen and hydrogen isotope relationships in hydrothermal mineral deposits. *In*: H.L. Barnes (Editor), *Geochemistry of Hydrothermal Ore Deposits*, 3rd ed., John Wiley and Sons, New York, p. 229-302.

Thomas, R.J., Von Veh, M.W. and McCourt, S., 1993. The tectonic evolution of southern Africa: an overview. *J. Afr. Earth Sci.*, **16**: 5-24.

Valley, J.W., 1986. Stable isotope geochemistry of metamorphic rocks. *In*: J.W. Valley, H.P. Taylor, Jr. and J.R. O'Neil (Editors), *Stable Isotopes in High-Temperature Geological Processes.* Mineral Soc. Am. Rev. Mineral., **16**: 445-489.

Van Vuuren, C.J.J., 1986. Regional setting and structure of the Rosh Pinah zinc-lead deposit, South West Africa/Namibia. *In*: C.R. Anhaeusser and S. Maske (Editors), *Mineral Deposits of Southern Africa.* Johannesburg, Geol. Soc. S. Afr., p.1593-1607.

Vennemann, T.W. and Smith, H.S., 1990. The rate and temperature of reaction of ClF_3 with silicate minerals, and their relevance to oxygen isotope analysis. *Chem. Geol. (Isot. Geosci. Sect.)*, **86**: 83-88.

Vennemann, T.W. and O'Neill, J.R., 1993. A simple and inexpensive method of hydrogen isotope and water analyses of minerals and rocks based on zinc reagent. *Chem. Geol. (Isot. Geosci. Sect.)*, **103**: 227-234.

Vityk, M.O. and Bodnar, R.J., 1995. Do fluid inclusions in high-grade metamorphic terranes preserve peak metamorphic density during retrograde decompression? *Am. Mineral.*, **80**: 641-644.

Von Veh, M.W., 1990. Diamictites in the Gariep Belt. *Abstracts Geocongress '90*, Geol. Soc. S. Afr., Cape Town, p. 586-589.

Von Veh, M.W., 1993. The stratigraphy and structural evolution of the Late Proterozoic Gariep Belt in the Sendelingsdrif-Annisfontein area, northwestern Cape Province. *Bull. Precamb. Research Unit*, Univ. Cape Town, **38**: 174p.

Waters, D.J., Robb, L.J. and Armstrong, R.A., 1996. A new time framework for Kibaran high-grade metamorphism in southern Africa: what drives granulite formation? Abstract. Kingston, September.

Yardley, B.W.D., 1989. *An introduction to metamorphic petrology.* Longman, New York, 254p.

Yardley, B.W.D., 1997. The evolution of fluids through the metamorphic cycle. *In*: B. Jamtveit and B.W.D.Yardley (Editors), *Fluid flow and transport in rocks: mechanisms and effects.* Chapman & Hall, London, p.99-121.

APPENDICES

APPENDIX 2

SAMPLE DETAILS

SAMPLE NO.	SAMPLE TYPE	MINE LOCALITIES	LATITUDE	LONGITUDE	HOST ROCK
WSB1	D_1/D_2 QUARTZ VEIN	S.O.F. No.1: 370m LEVEL	ROSH PINAH	ROSH PINAH	ROSH PINAH FM
WSB2	D_1/D_2 QUARTZ VEIN	S.O.F. No.1: 370m LEVEL	ROSH PINAH	ROSH PINAH	ROSH PINAH FM
WSB5	SECONDARY SPHALERITE	S.O.F. No.1: 370m LEVEL	ROSH PINAH	ROSH PINAH	ROSH PINAH FM
WSB11	D_1/D_2 QUARTZ VEIN	S.O.F. No.1: 370m LEVEL	ROSH PINAH	ROSH PINAH	ROSH PINAH FM
WSB14	D_1/D_2 QUARTZ VEIN	S.O.F. No.1: 370m LEVEL	ROSH PINAH	ROSH PINAH	ROSH PINAH FM
WSB15	D_1/D_2 QUARTZ VEIN	S.O.F. No.1: 370m LEVEL	ROSH PINAH	ROSH PINAH	ROSH PINAH FM
WSB24	SILICIC FOOTWALL BRECCIA	W.O.F. 280m LEVEL	ROSH PINAH	ROSH PINAH	ROSH PINAH FM
WSB31	PRIMARY CARBONATE ORE	W.O.F. 235m LEVEL	ROSH PINAH	ROSH PINAH	ROSH PINAH FM
WSB33	D_1/D_2 QUARTZ VEIN	S.O.F. No.1: 370m LEVEL	ROSH PINAH	ROSH PINAH	ROSH PINAH FM
WSB35	D_1/D_2 QUARTZ VEIN	-	27.8273	16.7113	BASEMENT GRANITE
WSB36	D_1/D_2 QUARTZ VEIN	-	27.8279	16.7114	BASEMENT GRANITE
WSB37	D_1/D_2 QUARTZ VEIN	-	27.8279	16.7114	BASEMENT GRANITE
WSB39	D_1/D_2 QUARTZ VEIN	-	27.8280	16.7110	BASEMENT GRANITE
WSB40	D_1/D_2 QUARTZ VEIN	-	27.8280	16.7118	BASEMENT GRANITE
WSB41	D_1/D_2 QUARTZ VEIN	-	27.8308	16.7138	BASEMENT GRANITE
WSB43	D_5 QUARTZ VEIN	-	27.8342	16.7139	BASEMENT GRANITE
WSB44	D_1/D_2 QUARTZ VEIN	-	27.8373	16.7176	BASEMENT GRANITE
WSB45	D_1/D_2 QUARTZ VEIN	-	27.8519	16.7457	BASEMENT GRANITE
WSB46	D_1/D_2 QUARTZ VEIN	-	28.2314	16.9248	KAIGAS FM
WSB47	D_3 QUARTZ VEIN	-	28.2289	16.9446	BASEMENT GRANITE
WSB48	D_5 QUARTZ VEIN	-	28.2332	16.9464	BASEMENT METAVOLCANICS
WSB49	D_5 QUARTZ VEIN	-	28.2325	16.9458	LEKKERSING FM
WSB50	D_1/D_2 QUARTZ VEIN	-	28.2319	16.9456	BASEMENT METAVOLCANICS
WSB51	D_1/D_2 QUARTZ VEIN	-	28.2294	16.9289	KAIGAS FM
WSB52	D_5 QUARTZ VEIN	-	28.2290	16.9301	PICKELHAUBE FM
WSB53	D_1/D_2 QUARTZ VEIN	-	28.2100	16.9342	BASEMENT METAVOLCANICS
WSB54	D_5 QUARTZ VEIN	-	28.2100	16.9342	VREDEFONTEIN FM
WSB55	D_1/D_2 QUARTZ VEIN	-	28.2175	16.9374	BASEMENT METAVOLCANICS
WSB56	D_1/D_2 QUARTZ VEIN	-	28.2228	16.9397	BASEMENT METAVOLCANICS
WSB57	D_1/D_2 QUARTZ VEIN	-	28.2346	16.9508	BASEMENT METAVOLCANICS
WSB58	D_5 QUARTZ VEIN	-	28.2427	16.9571	BASEMENT METAVOLCANICS

APPENDIX 2 (Continued)

SAMPLE DETAILS

SAMPLE NO.	SAMPLE TYPE	MINE LOCALITIES	LATITUDE	LONGITUDE	HOST ROCK
WSB59	D_1/D_2 QUARTZ VEIN	-	28.2459	16.9566	BASEMENT METAVOLCANICS
WSB60	D_1/D_2 QUARTZ VEIN	-	28.2549	16.9596	BASEMENT METAVOLCANICS
WSB61	D_1/D_2 QUARTZ VEIN	-	28.2626	16.9615	BASEMENT METAVOLCANICS
WSB62	D_1/D_2 QUARTZ VEIN	-	28.2688	16.9713	BASEMENT METAVOLCANICS
WSB63	D_1/D_2 QUARTZ VEIN	-	28.2736	16.9758	BASEMENT METAVOLCANICS
WSB64	D_1/D_2 QUARTZ VEIN	-	28.2863	16.9852	BASEMENT METAVOLCANICS
WSB65	D_3 QUARTZ VEIN	-	28.2911	16.9878	BASEMENT METAVOLCANICS
WSB66	D_5 QUARTZ VEIN	-	28.2954	16.8413	PICKELHAUBE FM
WSB67	D_1/D_2 QUARTZ VEIN	-	28.1377	16.8980	BASEMENT GRANITE
WSB68	D_5 QUARTZ VEIN	-	28.1427	16.9027	BASEMENT GRANITE
WSB69	D_1/D_2 QUARTZ VEIN	-	28.1440	16.9030	BASEMENT GRANITE
WSB70	D_1/D_2 QUARTZ VEIN	-	28.1478	16.9051	BASEMENT GRANITE
WSB71	D_5 QUARTZ VEIN	-	28.1522	16.9075	BASEMENT GRANITE
WSB72	D_5 QUARTZ VEIN	-	28.1654	16.9111	BASEMENT GRANITE
WSB73	D_1/D_2 QUARTZ VEIN	-	28.1673	16.9116	BASEMENT GRANITE
WSB74	D_1/D_2 QUARTZ VEIN	-	28.3922	16.8376	HOLGAT FM
WSB75	D_1/D_2 QUARTZ VEIN	-	28.3879	16.8329	HOLGAT FM
WSB76	D_1/D_2 QUARTZ VEIN	-	28.3819	16.8320	HOLGAT FM
WSB77	D_4 QUARTZ VEIN	-	28.3983	16.9095	NUMEES FM
WSB78	D_1/D_2 QUARTZ VEIN	-	28.2370	16.9343	PICKELHAUBE FM
WSB79	D_1/D_2 QUARTZ VEIN	-	28.2280	16.9293	PICKELHAUBE FM
WSB80	D_1/D_2 QUARTZ VEIN	-	28.2280	16.9293	PICKELHAUBE FM
WSB81	D_1/D_2 QUARTZ VEIN	-	28.2280	16.9293	PICKELHAUBE FM
WSB82	D_1/D_2 QUARTZ VEIN	-	28.2327	16.9203	KAIGAS FM
WSB83	D_1/D_2 QUARTZ VEIN	-	28.2407	16.9106	NUMEES FM
WSB84	D_5 QUARTZ VEIN	-	28.2407	16.9106	NUMEES FM
WSB85	D_5 QUARTZ VEIN	-	28.2425	16.9100	NUMEES FM
WSB86	D_3 QUARTZ VEIN	-	28.2425	16.9100	NUMEES FM
WSB87	D_1/D_2 QUARTZ VEIN	-	28.2421	16.9088	NUMEES FM
WSB88	D_1/D_2 QUARTZ VEIN	-	28.3304	17.0118	BASEMENT METASEDIMENTS

APPENDIX 2 (Continued)

SAMPLE DETAILS

SAMPLE NO.	SAMPLE TYPE	MINE LOCALITIES	LATITUDE	LONGITUDE	HOST ROCK
WSB89	D_5 QUARTZ VEIN	-	28.3282	17.0088	LEKKERSING FM
WSB90	D_1/D_2 QUARTZ VEIN	-	28.3273	17.0073	BASEMENT METASEDIMENTS
WSB91	D_1/D_2 CALCITE VEIN	-	28.2922	16.9698	NUMEES FM
WSB92	D_1/D_2 QUARTZ VEIN	-	28.2922	16.9698	KAIGAS FM
WSB93	D_1/D_2 QUARTZ VEIN	-	28.2351	16.9146	NUMEES FM
WSB94	D_1/D_2 QUARTZ VEIN	-	28.5107	16.7420	HOLGAT FM
WSB95	D_1/D_2 QUARTZ VEIN	-	28.0960	16.8659	NUMEES FM
WSB96	D_1/D_2 QUARTZ VEIN	-	28.0960	16.8659	NUMEES FM
WSB97	D_1/D_2 QUARTZ VEIN	-	28.1014	16.8757	KAIGAS FM
WSB98	D_1/D_2 QUARTZ VEIN	-	28.1006	16.8761	KAIGAS FM
WSB99	D_1/D_2 QUARTZ VEIN	-	28.0999	16.8763	KAIGAS FM
WSB100	D_3 QUARTZ VEIN	-	28.1006	16.8761	KAIGAS FM
WSB101	D_5 QUARTZ VEIN	-	28.0725	16.8957	BASEMENT GRANITE
WSB102	D_1/D_2 QUARTZ VEIN	-	28.0707	16.8914	KAIGAS FM
WSB105	D_1/D_2 QUARTZ VEIN	-	28.0721	16.8886	BASEMENT GRANITE
WSB106	D_5 QUARTZ VEIN	-	27.9829	16.8436	BASEMENT GRANITE
WSB109	D_1/D_2 QUARTZ VEIN	-	27.9316	16.7913	ROSH PINAH FM
WSB110	D_1/D_2 QUARTZ VEIN	-	27.9316	16.7913	ROSH PINAH FM
WSB113	D_1/D_2 CALCITE VEIN	-	27.9153	16.7076	PICKELHAUBE FM
WSB114	D_1/D_2 QUARTZ VEIN	-	27.9094	16.7069	PICKELHAUBE FM
WSB117	D_1/D_2 QUARTZ VEIN	-	27.9558	16.6975	PICKELHAUBE FM
WSB118	D_1/D_2 QUARTZ VEIN	-	28.0634	16.8539	NUMEES FM
WSB119	D_5 QUARTZ VEIN	-	28.0634	16.8539	NUMEES FM
WSB120	D_1/D_2 QUARTZ VEIN	-	28.0411	16.8498	NUMEES FM
WSB121	D_1/D_2 QUARTZ VEIN	-	27.8179	16.6714	ROSH PINAH FM
WSB123	D_1/D_2 CALCITE VEIN	-	27.8194	16.7067	BASEMENT GRANITE
WSB125	D_1/D_2 QUARTZ VEIN	-	27.8197	16.7071	BASEMENT GRANITE
WSB126	D_1/D_2 QUARTZ VEIN	-	27.8194	16.7067	BASEMENT GRANITE
WSB129	D_1/D_2 QUARTZ VEIN	-	27.8723	16.7614	ROSH PINAH FM
WSB135	D_4 QUARTZ VEIN	-	-28.4130	16.9155	HOLGAT FM

APPENDIX 2 (Continued)

SAMPLE DETAILS

SAMPLE NO.	SAMPLE TYPE	MINE LOCALITIES	LATITUDE	LONGITUDE	HOST ROCK
WSB136	D_4 QUARTZ VEIN	-	-28.4095	16.9125	NUMEES FM
WSB137	D_5 CALCITE VEIN	-	-28.2325	16.9200	NUMEES FM
WSB138	D_5 QUARTZ VEIN	-	-28.2310	16.9182	NUMEES FM
WSB139	D_3 QUARTZ VEIN	-	-28.2275	16.9140	NUMEES FM
WSB140	D_3 QUARTZ VEIN	-	-28.2356	16.9185	NUMEES FM
WSB141	D_1/D_2 QUARTZ VEIN	-	-28.2525	16.9195	NUMEES FM
WSB142	D_5 QUARTZ VEIN	-	-28.2320	16.9240	NUMEES FM
WSB144	D_3 QUARTZ VEIN	-	-28.2380	16.9240	NUMEES FM
WSB145	D_3 QUARTZ VEIN	-	-28.2400	16.9225	NUMEES FM
WSB146	D_5 QUARTZ VEIN	-	-28.3195	16.9305	NUMEES FM
WSB147	D_1/D_2 QUARTZ VEIN	-	-28.3872	16.8109	HOLGAT FM
WSB148	D_1/D_2 QUARTZ VEIN	-	-28.7961	17.0051	HOLGAT FM?
WSB149	D_1/D_2 QUARTZ VEIN	-	-29.0157	17.0841	LEKKERSING FM
WSB150	D_1/D_2 QUARTZ VEIN	-	-27.8558	16.7483	BASEMENT GRANITE
PN44b	D_1/D_2 QUARTZ VEIN	-	-28.2922	16.9698	KAIGAS FM
HFG146	D_1/D_2 QUARTZ VEIN	-			PICKELHAUBE FM

APPENDIX 3
STRUCTURAL DATA

SAMPLE NO.	VEIN GENERATION	VEIN ORIENTATION (DIP DIR./DIP)	FOLIATION S_1/S_2 (DIP DIR./DIP)	SAMPLE NO.	VEIN GENERATION	VEIN ORIENTATION (DIP DIR./DIP)	FOLIATION S_1/S_2 (DIP DIR./DIP)
MINE	-	-	186/60	WSB56	D_1/D_2	060/80	064/80
MINE	-	-	024/80	WSB57	D_1/D_2	223/85	227/80
MINE	-	-	040/48	WSB58	D_5	162/38	252/81
MINE	-	-	055/65	WSB59	D_1/D_2	253/77	253/77
MINE	-	-	050/60	WSB60	D_1/D_2	225/39	240/39
MINE	-	-	243/66	WSB61	D_1/D_2	250/70	259/70
MINE	-	-	218/50	WSB62	D_1/D_2	040/89	040/89
MINE	-	-	236/60	WSB63	D_1/D_2	230/73	220/73
MINE	-	-	050/52	WSB65	D_3	054/78	250/67
WSB35	D_1/D_2	250/56	250/56	WSB66	D_5	359/89	080/05
WSB36	D_1/D_2	242/47	242/47	WSB67	D_1/D_2	070/70	066/88
WSB37	D_1/D_2	242/62	242/62	WSB67	D_1/D_2	-	074/70
WSB39	D_1/D_2	245/72	249/68	WSB68	D_5	166/70	090/90
WSB40	D_1/D_2	232/67	230/49	WSB69	D_1/D_2	247/90	250/90
WSB40	D_1/D_2	-	230/62	WSB70	D_1/D_2	243/90	243/90
WSB40	D_1/D_2	-	230/54	WSB71	D_5	180/68	267/71
WSB41	D_1/D_2	233/69	236/69	WSB72	D_5	181/73	070/83
REGIONAL	-	-	048/88	WSB73	D_1/D_2	070/40	074/60
REGIONAL	-	-	240/84	WSB73	D_1/D_2	-	080/60
REGIONAL	-	-	231/72	WSB74	D_1/D_2	274/16	280/16
REGIONAL	-	-	070/76	WSB75	D_1/D_2	275/16	259/16
WSB43	D_5	170/60	-	WSB76	D_1/D_2	270/37	259/37
WSB43	D_5	169/52	-	WSB77	D_4	108/88	106/12
WSB44	D_1/D_2	252/68	249/68	WSB78	D_1/D_2	251/89	255/89
WSB44	D_1/D_2	242/90	060/89	WSB79	D_1/D_2	046/76	048/76
WSB45	D_1/D_2	050/80	063/83	WSB80	D_1/D_2	067/82	062/78
WSB46	D_1/D_2	231/88	231/88	WSB81	D_1/D_2	073/76	072/77
WSB47	D_3	065/54	063/58	WSB82	D_1/D_2	056/82	058/70
WSB48	D_5	200/20	271/59	WSB83	D_1/D_2	035/84	030/84
WSB49	D_5	194/32	253/79	WSB84	D_5	143/41	257/90
WSB50	D_1/D_2	230/40	230/40	WSB85	D_5	172/45	072/84
WSB51	D_1/D_2	067/86	068/81	WSB86	D_3	041/65	072/84
WSB51	D_1/D_2	066/82	216/88	WSB87	D_1/D_2	100/27	086/20
WSB52	D_5	160/40	070/84	WSB88	D_1/D_2	068/75	068/75
WSB53	D_1/D_2	048/77	060/77	WSB89	D_5	326/89	237/81
WSB54	D_5	183/38	030/78	WSB90	D_1/D_2	061/85	057/85
WSB55	D_1/D_2	240/88	230/88	WSB91	D_1/D_2	250/75	251/75

APPENDIX 3 (Continued)
STRUCTURAL DATA

SAMPLE NO.	VEIN GENERATION	VEIN ORIENTATION (DIP DIR./DIP)	FOLIATION S_1/S_2 (DIP DIR./DIP)
WSB92	D_1/D_2	251/75	251/75
WSB93	D_1/D_2	062/83	060/83
WSB95	D_1/D_2	087/90	092/90
WSB96	D_1/D_2	077/78	080/75
WSB97	D_1/D_2	074/90	074/90
WSB98	D_1/D_2	247/78	333/78
WSB99	D_1/D_2	-	083/71
WSB100	D_3	076/90	092/90
WSB102	D_1/D_2	072/90	072/60
WSB105	D_1/D_2	256/78	268/78
WSB106	D_5	175/68	035/90
WSB109	D_1/D_2	039/32	039/32
WSB109	D_1/D_2	052/52	052/52
WSB110	D_1/D_2	036/90	036/90
WSB113	D_1/D_2	047/82	047/82
WSB114	D_1/D_2	060/90	060/90
WSB117	D_1/D_2	062/90	062/90
WSB118	D_1/D_2	079/80	078/86
WSB119	D_5	147/58	072/90
WSB120	D_1/D_2	071/90	072/90
WSB125	D_1/D_2	047/90	047/90
WSB126	D_1/D_2	047/90	047/90
WSB129	D_1/D_2	234/68	231/68
WSB134	D_3	262/67	242/77
WSB138	D_5	118/64	250/78
WSB139	D_3	268/84	238/82
WSB140	D_3	270/88	253/84
WSB142	D_5	160/60	-
WSB144	D_3	077/88	261/86
WSB145	D_3	079/85	232/72
WSB146	D_5	180/45	-
WSB150	D_1/D_2	070/64	058/60
WSB150	D_1/D_2	-	042/86

APPENDIX 4

FLUID INCLUSION DATABASE

Note that the fluid inclusion database has been submitted in electronic form on the diskette that accompanies this work. The data has been saved in Microsoft Excel v. 5.0 and Lotus 1-2-3 formats. The following files are on the disk:

FILENAME	DESCRIPTION	TYPE
APPENDIX4.xls	All inclusion data in separate worksheets	MS EXCEL v 5.0
PRE.wk1	Pre-orogenic inclusion data	LOTUS 1-2-3
D1D2.wk1	D_1/D_2 inclusion data	LOTUS 1-2-3
D3.wk1	D_3 inclusion data	LOTUS 1-2-3
D4.wk1	D_4 inclusion data	LOTUS 1-2-3
D5.wk1	D_5 inclusion data	LOTUS 1-2-3

Note that the salinity estimates presented in Appendix 7 are the averages of different trails, highlighted in the Excel file by thicker lines, and in the *.wk1 files by trail numbers.

APPENDIX 5

STABLE ISOTOPE DATA

SAMPLE	$\delta^{18}O_{QTZ}$ (‰) (V-S.M.O.W.)	$\delta^{18}O_{HOST}$ (‰) (V-S.M.O.W.)	$\delta^{18}O_{CALCITE}$ (‰) (V-P.D.B)	δD (‰)$_{QTZ\ INCLUSION\ FLUIDS}$ (V-S.M.O.W.)
WSB2	13.04	-	-	-35.01
WSB11	12.77	8.01	-	-
WSB14	13.23	10.56	-	-
WSB15	13.14	-	-	-
WSB33	12.43	-	-	-
WSB40	11.34	-	-	-53.89
WSB43	9.67	-	-	-
WSB44a	12.10	-	-	-
WSB44b	12.23	-	-	-
WSB46	12.40	-	-	-75.63
WSB47	7.66	6.34	-	-
WSB48	11.31	-	-	-
WSB49	11.96	11.04	-	-
WSB51	12.05	11.22	-	-
WSB52	22.96	21.55	-	-
WSB53	10.18	9.34	-	-
WSB54	9.85	9.93	-	-
WSB55	10.89	9.97	-	-
WSB56	9.97	-	-	-
WSB57	6.81	-	-	-
WSB58	9.03	-	-	-
WSB59	9.81	-	-	-
WSB61	9.59	-	-	-
WSB66	11.90	12.25	-	-
WSB67	9.96	9.45	-	-
WSB68	9.08	8.10	-	-
WSB71	11.00	10.22	-	-
WSB74	16.35	11.68	-	-
WSB75	16.09	11.53	-	-
WSB76	16.23	12.56	-	-
WSB77	13.91	11.31	-	-
WSB78	22.75	-	-	-

APPENDIX 5 (Continued)

STABLE ISOTOPE DATA

SAMPLE	$\delta^{18}O_{QTZ}$ (‰) (V-S.M.O.W.)	$\delta^{18}O_{HOST}$ (‰) (V-S.M.O.W.)	$\delta^{18}O_{CALCITE}$ (‰) (V-P.D.B)	δD (‰)$_{QTZ\ INCLUSION\ FLUIDS}$ (V-S.M.O.W.)
WSB80	24.43	24.53	-	-
WSB81	25.17	24.53	-	-
WSB82	12.24	-	-	-
WSB83	15.24	14.23	-	-
WSB85	14.55	-	-	-
WSB86	14.06	-	-	-
WSB87	13.29	-	-	-
WSB88	9.04	7.25	-	-
WSB89	9.51	10.45	-	-
WSB90	11.30	8.24	-	-
WSB91	-	-	14.28	-
WSB92	11.66	10.82	-	-
WSB93	13.22	10.10	-	-
WSB94	16.64	-	-	-
WSB101	10.19	8.99	-	-46.26
WSB105	11.37	-	-	-
WSB106	10.69	8.53	-	-
WSB109	14.37	13.84	-	-
WSB113	-	-	23.34	-
WSB114	17.45	-	-	-
WSB117	18.24	17.05	-	-
WSB118	13.71	8.96	-	-
WSB119	12.80	-	-	-
WSB120	13.10	-	-	-
WSB121	12.13	-	-	-
WSB123	-	-	11.72	-
WSB125	8.72	6.44	-	-
WSB136	11.86	-	-	-
WSB137	-	-	14.18	-
WSB139	13.92	-	-	-
WSB140	12.97	-	-	-
WSB141	17.30	14.89	-	-

APPENDIX 5 (Continued)

STABLE ISOTOPE DATA

SAMPLE	$\delta^{18}O_{QTZ}$ (‰) (V-S.M.O.W.)	$\delta^{18}O_{HOST}$ (‰) (V-S.M.O.W.)	$\delta^{18}O_{CALCITE}$ (‰) (V-P.D.B)	δD (‰)$_{QTZ\ INCLUSION\ FLUIDS}$ (V-S.M.O.W.)
WSB145	13.59	-	-	-
WSB147	14.31	-	-	-
WSB148	16.13	-	-	-
WSB149	11.72	11.64	-	-
WSB150	10.14	-	-	-

APPENDIX 6

RESULTS OF CRUSH-LEACH ANALYSIS

Sample Number	Li^+ (ppm)	Na^+ (ppm)	NH_4^+ (ppm)	K^+ (ppm)	Mg^{2+} (ppm)	Mn^{2+} (ppm)	Ca^{2+} (ppm)	Cl^- (ppm)	Br^- (ppm)	SO_4^{2-} (ppm)
WSB15(i)	0.033	2.309	0.216	0.163	0.232	0.030	0.043	2.897	0.000	0.372
WSB15(ii)	0.020	1.591	0.156	0.089	0.051	0.037	0.048	1.851	0.055	0.110
WSB15(iii)	0.021	1.437	0.160	0.093	0.133	0.037	0.007	1.488	0.000	0.438
WSB43(i)	0.000	2.669	0.106	0.083	0.040	0.023	2.100	5.871	0.055	0.000
WSB43(ii)	0.000	2.402	0.090	0.134	0.043	0.008	1.683	3.240	0.165	0.051
WSB43(iii)	0.000	2.592	0.095	0.077	0.029	0.015	0.976	4.947	0.097	0.083
WSB106(i)	0.007	0.716	0.107	0.025	0.039	0.007	0.040	1.198	0.000	0.008
WSB106(ii)	0.007	0.515	0.090	0.015	0.029	0.002	0.011	0.751	0.000	0.169
WSB106(iii)	0.006	0.437	0.099	0.006	0.025	0.004	0.036	1.618	0.000	0.110
WSB05(i)	0.000	0.920	0.210	0.554	0.108	0.047	0.104	0.931	0.000	2.522
WSB05(ii)	0.000	0.307	0.212	0.050	0.025	0.052	0.022	5.607	0.000	5.410
WSB05(iii)	0.000	0.312	0.195	0.035	0.010	0.070	0.239	0.510	0.000	4.277
WSB31(i)	0.001	0.266	0.361	0.534	8.748	0.000	9.941	0.261	0.000	3.708
WSB31(ii)	0.001	0.886	0.075	0.195	4.194	0.000	6.529	0.161	0.000	1.727
WSB31(iii)	0.001	0.230	0.144	0.315	5.898	0.000	7.771	0.173	0.000	4.607
WSB24(i)	0.003	2.071	0.247	3.420	4.936	0.000	6.572	3.333	0.000	9.681
WSB24(ii)	0.001	0.305	0.039	1.178	2.246	0.000	2.278	0.853	0.000	2.544
WSB24(iii)	0.002	1.850	0.203	2.603	3.778	0.000	5.921	2.628	0.000	8.284
WSB24(iv)	0.002	0.699	0.232	2.318	2.836	0.000	4.999	0.945	0.000	3.744
PN44B(i)	0.007	1.803	0.231	0.209	0.000	0.019	0.629	1.362	0.000	0.024
PN44B(ii)	0.003	1.395	0.240	0.176	0.000	0.004	0.080	0.982	0.000	0.014
PN44B(iii)	0.006	1.455	0.288	0.219	0.014	0.006	0.591	1.086	0.000	0.014
WSB40(i)	0.010	4.287	0.376	0.339	0.048	0.041	2.532	6.455	0.178	0.069
WSB40(ii)	0.007	3.397	0.272	0.295	0.000	0.015	1.086	4.758	0.127	0.028
WSB96(i)	0.006	0.849	0.278	0.115	0.021	0.000	1.961	0.634	0.000	0.039
WSB96(ii)	0.005	0.661	0.271	0.074	0.032	0.010	2.093	0.438	0.000	0.056
WSB96C(i)	0.016	2.603	0.319	0.381	0.797	0.000	12.567	3.099	0.055	1.606
WSB96C(ii)	0.017	2.869	0.257	0.392	0.813	0.000	12.549	3.914	0.000	1.088
WSB86(i)	0.001	1.086	0.305	0.130	0.053	0.001	5.419	1.042	0.000	1.326
WSB86(ii)	0.001	0.944	0.247	0.147	0.036	0.007	1.836	0.926	0.000	0.672

APPENDIX 7

AVERAGE SALINITY ESTIMATES FOR DIFFERENT INCLUSION TRAILS

SAMPLE	GENERATION	FPD	SALINITY (wt% $NaCl_{eq}$)	T_hH_2O (°C)	SAMPLE	GENERATION	FPD	SALINITY (wt% $NaCl_{eq}$)	T_hH_2O (°C)
HFG146	D_1/D_2	2.3	3.87	227.2	WSB15	D_1/D_2	5.7	8.81	242.0
HFG146	D_1/D_2	2.4	4.03	214.7	WSB15	D_1/D_2	6.0	9.21	239.7
HFG146	D_1/D_2	8.2	11.93	248.7	WSB15	D_1/D_2	6.5	9.86	217.3
HFG146	D_1/D_2	1.7	2.90	216.3	WSB15	D_1/D_2	6.0	9.21	192.1
HFG146	D_1/D_2	2.6	4.34	231.8	WSB24	D_1/D_2	2.7	4.49	212.2
HFG146	D_1/D_2	2.5	4.18	253.0	WSB40	D_1/D_2	5.9	9.08	137.7
HFG146	D_1/D_2	0.8	1.40	235.3	WSB40	D_1/D_2	0.9	1.57	106.9
HFG146	D_1/D_2	1.1	1.91	242.4	WSB40	D_1/D_2	11.8	15.76	193.7
HFG146	D_1/D_2	1.3	2.24	224.7	WSB40	D_1/D_2	5.0	7.86	134.8
HFG146	D_1/D_2	1.3	2.24	238.1	WSB40	D_1/D_2	5.1	8.00	169.9
HFG146	D_1/D_2	1.2	2.07	219.0	WSB40	D_1/D_2	10.9	14.87	274.3
HFG146	D_1/D_2	2.3	3.87	232.4	WSB40	D_1/D_2	7.4	10.98	139.4
HFG146	D_1/D_2	2.3	3.87	227.1	WSB40	D_1/D_2	7.9	11.58	141.0
HFG146	D_1/D_2	2.4	4.03	227.0	WSB40	D_1/D_2	10.1	14.04	184.2
HFG146	D_1/D_2	1.2	2.07	243.4	WSB40	D_1/D_2	10.5	14.46	155.3
HFG146	D_1/D_2	3.6	5.86	238.4	WSB43	D_5	6.7	10.11	153.2
HFG146	D_1/D_2	2.8	4.65	226.3	WSB43	D_5	10.2	14.15	176.4
HFG146	D_1/D_2	2.5	4.18	225.3	WSB43	D_5	10.4	14.36	165.3
HFG146	D_1/D_2	2.5	4.18	224.2	WSB43	D_5	8.7	12.51	140.2
HFG146	D_1/D_2	2.6	4.34	236.3	WSB43	D_5	11.2	15.17	180.9
PN44B	D_1/D_2	4.5	7.17	203.4	WSB43	D_5	6.0	9.21	156.9
PN44B	D_1/D_2	8.9	12.73	187.5	WSB43	D_5	4.1	6.59	140.9
PN44B	D_1/D_2	1.7	2.90	181.7	WSB43	D_5	5.1	8.00	161.8
PN44B	D_1/D_2	1.5	2.57	198.1	WSB43	D_5	5.4	8.41	153.3
PN44B	D_1/D_2	0.6	1.05	200.9	WSB43	D_5	7.0	10.49	159.0
PN44B	D_1/D_2	3.4	5.56	189.2	WSB43	D_5	3.8	6.16	146.0
WSB1	D_1/D_2	3.7	6.01	229.9	WSB43	D_5	5.4	8.41	143.2
WSB15	D_1/D_2	5.5	8.55	169.5	WSB43	D_5	5.3	8.28	168.5
WSB15	D_1/D_2	1.3	2.24	212.5	WSB43	D_5	5.4	8.41	150.5
WSB15	D_1/D_2	1.3	2.24	186.7	WSB46	D_1/D_2	0.6	1.05	208.7
WSB15	D_1/D_2	5.5	8.55	251.6	WSB46	D_1/D_2	0.7	1.22	203.1
WSB15	D_1/D_2	1.4	2.41	243.8	WSB46	D_1/D_2	1.2	2.07	214.0

FPD = FREEZING POINT DEPRESSION

APPENDIX 7 (Continued)

AVERAGE SALINITY ESTIMATES FOR DIFFERENT INCLUSION TRAILS

SAMPLE	GENERATION	FPD	SALINITY (wt% $NaCl_{eq}$)	T_hH_2O (°C)	SAMPLE	GENERATION	FPD	SALINITY (wt% $NaCl_{eq}$)	T_hH_2O (°C)
WSB46	D_1/D_2	1.0	1.74	205.4	WSB67	D_1/D_2	4.7	7.45	256.8
WSB46	D_1/D_2	1.1	1.91	202.7	WSB67	D_1/D_2	5.0	7.86	222.0
WSB46	D_1/D_2	0.8	1.40	209.7	WSB67	D_1/D_2	3.7	6.01	151.0
WSB46	D_1/D_2	0.9	1.57	208.9	WSB67	D_1/D_2	8.0	11.70	164.1
WSB46	D_1/D_2	1.2	2.07	205.5	WSB67	D_1/D_2	6.1	9.34	163.9
WSB46	D_1/D_2	1.1	1.91	205.4	WSB67	D_1/D_2	6.7	10.11	159.7
WSB46	D_1/D_2	1.1	1.91	204.7	WSB67	D_1/D_2	2.4	4.03	165.4
WSB46	D_1/D_2	1.3	2.24	199.4	WSB67	D_1/D_2	4.8	7.59	196.8
WSB46	D_1/D_2	0.7	1.22	195.0	WSB67	D_1/D_2	4.9	7.73	210.4
WSB46	D_1/D_2	1.0	1.74	200.0	WSB67	D_1/D_2	5.7	8.81	196.4
WSB46	D_1/D_2	0.7	1.22	206.3	WSB67	D_1/D_2	4.6	7.31	187.4
WSB46	D_1/D_2	0.3	0.53	202.7	WSB67	D_1/D_2	4.7	7.45	195.9
WSB46	D_1/D_2	1.3	2.24	211.7	WSB67	D_1/D_2	4.1	6.59	185.7
WSB46	D_1/D_2	1.4	2.41	204.5	WSB67	D_1/D_2	5.7	8.81	176.5
WSB46	D_1/D_2	0.8	1.40	213.2	WSB77	D_4	1.7	2.90	244.7
WSB49	D_5	9.3	13.18	169.8	WSB77	D_4	1.7	2.90	237.3
WSB49	D_5	2.9	4.80	164.3	WSB77	D_4	9.0	12.85	221.8
WSB49	D_5	0.4	0.70	162.1	WSB77	D_4	9.3	13.18	224.1
WSB49	D_5	2.9	4.80	152.0	WSB77	D_4	1.5	2.57	244.8
WSB49	D_5	3.8	6.16	163.4	WSB80	D_1/D_2	1.2	2.07	181.5
WSB49	D_5	0.8	1.40	165.1	WSB80	D_1/D_2	1.5	2.57	180.0
WSB49	D_5	0.1	0.18	174.5	WSB80	D_1/D_2	1.6	2.74	183.0
WSB49	D_5	0.4	0.70	155.9	WSB80	D_1/D_2	2.9	4.80	173.2
WSB49	D_5	4.0	6.45	168.3	WSB80	D_1/D_2	2.5	4.18	185.8
WSB49	D_5	3.7	6.01	163.5	WSB80	D_1/D_2	1.9	3.23	203.0
WSB67	D_1/D_2	4.7	7.45	182.3	WSB80	D_1/D_2	1.5	2.57	187.2
WSB67	D_1/D_2	4.3	6.88	165.8	WSB80	D_1/D_2	1.6	2.74	191.8
WSB67	D_1/D_2	4.7	7.45	192.3	WSB80	D_1/D_2	1.4	2.41	216.4
WSB67	D_1/D_2	5.8	8.95	176.1	WSB80	D_1/D_2	1.6	2.74	196.0
WSB67	D_1/D_2	5.0	7.86	186.3	WSB80	D_1/D_2	4.3	6.88	166.5
WSB67	D_1/D_2	4.7	7.45	169.5	WSB80	D_1/D_2	4.4	7.02	171.7
WSB67	D_1/D_2	4.2	6.74	158.4	WSB80	D_1/D_2	1.7	2.90	207.0

FPD = FREEZING POINT DEPRESSION

APPENDIX 7 (Continued)

AVERAGE SALINITY ESTIMATES FOR DIFFERENT INCLUSION TRAILS

SAMPLE	GENERATION	FPD	SALINITY (wt% $NaCl_{eq}$)	T_hH_2O (°C)	SAMPLE	GENERATION	FPD	SALINITY (wt% $NaCl_{eq}$)	T_hH_2O (°C)
WSB80	D_1/D_2	1.4	2.41	201.6	WSB86	D_3	4.0	6.45	193.9
WSB80	D_1/D_2	1.4	2.41	203.6	WSB96	D_1/D_2	0.4	0.70	225.0
WSB80	D_1/D_2	1.4	2.41	198.0	WSB96	D_1/D_2	6.1	9.34	208.8
WSB80	D_1/D_2	1.6	2.74	183.5	WSB96	D_1/D_2	6.9	10.36	197.9
WSB80	D_1/D_2	1.5	2.57	184.8	WSB96	D_1/D_2	6.8	10.24	173.9
WSB80	D_1/D_2	1.8	3.06	187.9	WSB96	D_1/D_2	5.8	8.95	229.5
WSB80	D_1/D_2	1.5	2.57	161.3	WSB96	D_1/D_2	4.1	6.59	201.4
WSB80	D_1/D_2	1.3	2.24	203.4	WSB96	D_1/D_2	10.3	14.25	166.4
WSB80	D_1/D_2	1.3	2.24	147.3	WSB96	D_1/D_2	4.3	6.88	216.2
WSB80	D_1/D_2	1.3	2.24	182.2	WSB96	D_1/D_2	3.7	6.01	206.6
WSB85	D_5	1.9	3.23	144.8	WSB96	D_1/D_2	3.9	6.30	161.9
WSB85	D_5	1.3	2.24	156.5	WSB96	D_1/D_2	3.6	5.86	180.2
WSB85	D_5	3.2	5.26	158.0	WSB96	D_1/D_2	3.9	6.30	216.9
WSB85	D_5	3.1	5.11	161.9	WSB96	D_1/D_2	8.1	11.81	152.1
WSB85	D_5	3.0	4.96	154.6	WSB96	D_1/D_2	2.7	4.49	181.9
WSB85	D_5	4.0	6.45	164.4	WSB96	D_1/D_2	4.6	7.31	238.1
WSB85	D_5	4.5	7.17	149.7	WSB96	D_1/D_2	3.7	6.01	169.4
WSB85	D_5	4.1	6.59	171.4	WSB100	D_3	2.9	4.80	187.5
WSB85	D_5	3.9	6.30	164.1	WSB100	D_3	5.5	8.55	175.1
WSB85	D_5	3.3	5.41	179.8	WSB100	D_3	7.1	10.61	178.2
WSB86	D_3	6.7	10.11	189.4	WSB100	D_3	6.4	9.73	181.4
WSB86	D_3	1.7	2.90	194.7	WSB100	D_3	5.4	8.41	172.7
WSB86	D_3	0.1	0.18	193.2	WSB100	D_3	5.1	8.00	156.8
WSB86	D_3	6.5	9.86	190.1	WSB100	D_3	4.0	6.45	196.6
WSB86	D_3	7.2	10.73	183.4	WSB100	D_3	6.0	9.21	164.8
WSB86	D_3	5.7	8.81	177.5	WSB100	D_3	8.6	12.39	167.5
WSB86	D_3	6.0	9.21	184.3	WSB100	D_3	5.7	8.81	195.3
WSB86	D_3	0.3	0.53	197.5	WSB100	D_3	4.9	7.73	193.6
WSB86	D_3	0.1	0.18	191.1	WSB100	D_3	8.6	12.39	164.3
WSB86	D_3	6.3	9.60	176.6	WSB101	D_5	3.2	5.26	150.1
WSB86	D_3	6.1	9.34	176.6	WSB101	D_5	3.1	5.11	150.9
WSB86	D_3	4.4	7.02	203.1	WSB101	D_5	3.8	6.16	147.0

FPD = FREEZING POINT DEPRESSION

APPENDIX 7 (Continued)

AVERAGE SALINITY ESTIMATES FOR DIFFERENT INCLUSION TRAILS

SAMPLE	GENERATION	FPD	SALINITY (wt% $NaCl_{eq}$)	T_hH_2O (°C)	SAMPLE	GENERATION	FPD	SALINITY (wt% $NaCl_{eq}$)	T_hH_2O (°C)
WSB101	D_5	3.7	6.01	143.5	WSB139	D_3	1.5	2.57	185.1
WSB101	D_5	4.9	7.73	153.3	WSB139	D_3	1.5	2.57	185.4
WSB101	D_5	3.0	4.96	148.2	WSB139	D_3	1.7	2.90	192.3
WSB101	D_5	3.0	4.96	148.7	WSB139	D_3	2.0	3.39	189.0
WSB101	D_5	3.0	4.96	144.9	WSB139	D_3	5.8	8.95	198.4
WSB101	D_5	2.6	4.34	152.0	WSB139	D_3	1.8	3.06	200.7
WSB101	D_5	2.9	4.80	153.7	WSB139	D_3	5.9	9.08	198.2
WSB101	D_5	3.4	5.56	158.2	WSB139	D_3	1.5	2.57	209.8
WSB101	D_5	2.9	4.80	162.7	WSB139	D_3	1.8	3.06	201.0
WSB106	D_5	1.9	3.23	136.9	WSB139	D_3	1.6	2.74	207.8
WSB106	D_5	6.4	9.73	154.4	WSB139	D_3	1.7	2.90	205.0
WSB106	D_5	1.8	3.06	139.3	WSB144	D_3	5.2	8.14	188.7
WSB106	D_5	1.7	2.90	142.0	WSB144	D_3	4.7	7.45	184.6
WSB106	D_5	4.1	6.59	153.3	WSB144	D_3	5.0	7.86	196.1
WSB106	D_5	3.2	5.26	149.7	WSB144	D_3	5.2	8.14	173.8
WSB106	D_5	0.2	0.35	140.4	WSB144	D_3	5.9	9.08	190.0
WSB106	D_5	4.4	7.02	167.0	WSB144	D_3	9.3	13.18	169.4
WSB106	D_5	3.6	5.86	148.1	WSB144	D_3	3.8	6.16	202.8
WSB106	D_5	1.4	2.41	143.4	WSB144	D_3	6.0	9.21	202.5
WSB106	D_5	4.4	7.02	154.7	WSB144	D_3	6.0	9.21	202.2
WSB106	D_5	1.5	2.57	143.1	WSB149	D_1/D_2	4.6	7.31	146.2
WSB106	D_5	3.0	4.96	141.6	WSB149	D_1/D_2	2.3	3.87	165.7
WSB106	D_5	3.4	5.56	159.4	WSB149	D_1/D_2	3.0	4.96	173.7
WSB135	D_4	12.3	16.24	221.0					
WSB135	D_4	3.6	5.86	266.9					
WSB135	D_4	4.6	7.31	273.0					
WSB135	D_4	7.5	11.10	287.0					
WSB135	D_4	4.8	7.59	247.7					
WSB135	D_4	3.5	5.71	257.4					
WSB135	D_4	4.2	6.74	235.1					
WSB135	D_4	6.1	9.34	234.3					
WSB139	D_3	4.7	7.45	195.0					

FPD = FREEZING POINT DEPRESSION